Silicate melt inclusions in the new millennium: A review of recommended practices for preparation, analysis, and data presentation

E.F. Rose-Koga, A.-S. Bouvier, G.A. A Gaetani, P.J. J Wallace, C.M. M
Allison, J.A. A Andrys, C.A. A Angeles de La Torre, A. Barth, R.J. J
Bodnar, A.J.J. Bracco Gartner, et al.

Journal Pre-proof

Silicate melt inclusions in the new millennium: A review of recommended practices for preparation, analysis, and data presentation

E.F. Rose-Koga, A.-S. Bouvier, G.A. Gaetani, P.J. Wallace, C.M. Allison, J.A. Andrys, Angeles de la Torre CA, A. Barth, R.J. Bodnar, Bracco Gartner AJJ, Butters, A. Castillejo, B. Chilson-Parks, B.R. Choudhary, N. Cluzel, M. Cole, E. Cottrell, A. Daly, L.V. Danyushevsky, DeVitre CL, M.J. Drignon, L. France, M. Gaborieau, M.O. Garcia, E. Gatti, F.S. Genske, Hartley, E.C. Hughes, A.A. Iveson, E.R. Johnson, M. Jones, T. Kagoshima, Y. Katzir, M. Kawaguchi, T. Kawamoto, K.A. Kelley, J.M. Koornneef, Kurz, M. Laubier, G.D. Layne, A. Lerner, K.-Y. Lin, P.-P. Liu, A. Lorenzo-Merino, N. Luciani, N. Magalhães, H.R. Marschall, P.J. Michael, B.D. Monteleone, L.R. Moore, Y. Moussallam, M. Muth, M.L. Myers, D.F. Narváez, O. Navon, Newcombe, Nichols ARL, R.L. Nielsen, A. Pamukcu, T. Plank, D.J. Rasmussen, J. Roberge, F. Schiavi, Schwartz, Shimizu Kei, K. Shimizu, N. Shimizu, J.B. Thomas, G.T. Thompson, J.M. Tucker, G. Ustunisik, C. Waelkens, Y. Zhang, T. Zhou

This is a PDF file of an article that has undergone enhancements after acceptance, such as the addition of a cover page and metadata, and formatting for readability, but it is not yet the definitive version of record. This version will undergo additional copyediting, typesetting and review before it is published in its final form, but we are providing this version to give early visibility of the article. Please note that, during the production process, errors may be discovered which could affect the content, and all legal disclaimers that apply to the journal pertain.

Silicate melt inclusions in the new millennium: A review of recommended practices for preparation, analysis, and data presentation

Rose-Koga EF[1], Bouvier A-S[2], Gaetani GA[3], Wallace PJ[4], Allison CM[5], Andrys JA[6], Angeles de la Torre CA[7], Barth A[8], Bodnar RJ[9], Bracco Gartner AJJ[10], Butters DA[11], Castillejo A[3], Chilson-Parks B[12], Choudhary BR[13], Cluzel N[1], Cole M[14], Cottrell E[15], Daly A[3], Danyushevsky LV[16], DeVitre CL[5], Drignon MJ[17], France L[18], Gaborieau M[1], Garcia MO[19], Gatti E[20], Genske FS[21], Hartley ME[22], Hughes EC[20], Iveson AA[23], Johnson ER[14], Jones M[3], Kagoshima T[24], Katzir Y[25], Kawaguchi M[1,44], Kawamoto T[26], Kelley KA[6], Koornneef JM[10], Kurz MD[3], Laubier M[1], Layne GD[27], Lerner A[4], Lin K-Y[28], Liu P.-P.[29], Lorenzo-Merino A[30], Luciani N[10], Magalhães N[31,32], Marschall HR[33], Michael PJ[34], Monteleone BD[3], Moore LR[9], Moussallam Y[1,8], Muth M[4], Myers ML[1], Narváez DF[1,46], Navon O[35], Newcombe ME[31], Nichols ARL[36], Nielsen RL[17,41], Pamukcu A[3], Plank T[8], Rasmussen DJ[8], Roberge J[7], Schiavi F[1], Schwartz DM[37], Shimizu Kei[38], Shimizu K[39], Shimizu N[3], Thomas JB[40], Thompson GT[40], Tucker JM[38], Ustunisik G[41], Waelkens C[42], Zhang Y[43], Zhou T[45].

Affiliations:

1: CNRS, Université Clermont Auvergne, IRD, OPGC, Laboratoire Magmas et Volcans, F-63000 Aubière, France

2: Institut des Sciences de la Terre, Université de Lausanne, Switzerland

3: Department of Geology and Geophysics, Woods Hole Oceanographic Institution, Woods Hole, Massachusetts 02543, USA

4: Department of Earth Sciences, University of Oregon, Eugene, OR 97403-1272, United States

5: Department of Earth and Atmospheric Sciences, Cornell University, Ithaca, NY 14853, USA

6: Graduate School of Oceanography, University of Rhode Island, Narragansett, RI 02882, USA.

7: ESIA-Ticoman, Instituto Politecnico Nacional (IPN), D.F. 07340, Mexico

8: Lamont-Doherty Earth Observatory of Columbia University, Palisades, NY 10960, USA

9: Department of Geosciences, Virginia Tech, Blacksburg, Virginia 24061, U.S.A.

10: Faculty of Science, Vrije Universiteit Amsterdam, De Boelelaan 1085, 1081 HV Amsterdam, The Netherlands

11: Department of Earth Sciences, Wills Memorial Building, Queen's Road, University of Bristol, Bristol BS8 1RJ, UK.

12: Department of Geological Sciences, Brown University, Providence, RI 02912, USA.

13: Guangzhou Institute of Geochemistry, Chinese Academy of Sciences, Guangzhou 510640, China

14: Dept. Geological Sciences, New Mexico State University, Las Cruces, NM 88003, USA

15: Department of Mineral Sciences, National Museum of Natural History, Smithsonian Institution, 10th & Constitution Ave., Washington DC, 20560, USA

16: Earth Sciences and CODES, University of Tasmania, PB79, Hobart TAS 7001, Australia

17: College of Earth, Ocean, and Atmospheric Sciences, Oregon State University, Corvallis, OR 97331-5503, USA

18: Centre de Recherches Pétrographiques et Géochimiques, Université de Lorraine, CNRS UMR 7358, Nancy, France.

19: Hawaii Center for Volcanology, Department of Geology and Geophysics, University of Hawaii, Honolulu, HI 96822, USA

20: Division of Geological and Planetary Sciences, California Institute of Technology, Pasadena, California 91125, USA

21: Institut fur Mineralogie, Westfälische Wilhelms-Universität Münster, Corrensstrasse 24, 48149 Münster, Germany

22: Department of Earth and Environmental Sciences, University of Manchester, Oxford Road, Manchester, M13 9PL, UK

23: Department of Earth Sciences, Durham University, Durham DH13LE, UK

24: Geological lnstitute, University of Tokyo, Tokyo 113, Japan

25: Department of Geological and Environmental Sciences, The Faculty of Natural Sciences, Ben-Gurion University of the Negev, P.O. Box 653, Beer Sheva 84105, Israel

26: Faculty of Science, Department of Geosciences, Shizuoka University, 422-8529, Japan.

27: Department of Earth Sciences, NC 1047, Memorial University, St. John's, Newfoundland A1B 3X5, Canada

28: Department of Earth Sciences, University of Delaware, Newark, DE 19711, USA

29: Key Laboratory of Orogenic Belts and Crustal Evolution, School of Earth and Space Sciences, Peking University, Beijing 100871, China.

30: Instituto de Geofisica, UNAM, Ciudad de Mexico, 04510, Mexico

31: Department of Geology, University of Maryland, College Park, MD 20742, USA

32: Department of Earth Sciences, University of Toronto, Toronto, ON M5S 3B1, Canada

33: Goethe Universität Frankfurt, Altenhöferallee 1, 60438 Frankfurt am Main, Germany

34: College of Engineering & Natural Sciences, University of Tulsa, 800 S. Tucker Drive Tulsa, OK 74104, USA

35: Institute of Earth Sciences, The Hebrew University of Jerusalem, 91904 Jerusalem, Israel

36: School of Earth and Environment, University of Canterbury, Private Bag 4800, Christchurch 8140, New Zealand

37: Department of Geosciences, Boise State University, 83725, Boise, ID, USA

38: Department of Terrestrial Magnetism, Carnegie Institution for Science, Washington, DC 20015, USA.

39: Kochi Institute for Core Sample Research, Japan Agency for Marine-Earth Science and Technology, Nankoku 783-8502, Japan.

40: Department of Earth Sciences, Syracuse University, Syracuse, NY 13244, USA

41: Geology and Geological Engineering, South Dakota School of Mines and Technology, Rapid City, SD 57701, USA

42: Department of Earth and Planetary Sciences, McGill University, Montreal, Quebec, Canada H3A 0E8

43: Institute of Oceanology, Chinese Academy of Sciences, Beijing, China

44: Kumamoto University, Graduate School of Science and Technology, Kurokami 2-36-1, Kumamoto 860-8555, Japan

45: China University of Petroleum (East China), Qingdao, China, 266580

46: Departamento de Geología, Escuela Politécnica Nacional, Ladrón de Guevara E11-253, Quito, Ecuador

Abstract

Mineral-hosted melt inclusions have become an important source of information on magmatic processes. As the number of melt inclusion studies increases, so does the need to establish recommended practice guidelines for collecting and reporting melt inclusion data. These guidelines are intended to ensure certain quality criteria are met and to achieve consistency among published melt inclusion data in order to maximize their utility in the future. Indeed, with the improvement of analytical techniques, new processes affecting melt inclusions are identified. It is thus critical to be able to reprocess any previously published data, such that reporting the raw data is one of the first "recommended practices" for authors and a publication-criteria that reviewers should be sensitive to. Our guidelines start with melt inclusion selection, which is a critical first step, and then continue on to melt inclusion preparation and analysis, covering the entire field of methods applicable to melt inclusions.

Dedication

In March of 2000, a melt inclusion workshop was held at the Chateau de Sassenage in Grenoble and a companion issue of Chemical Geology entitled "Melt Inclusions at the Millennium" was published. Erik Hauri was heavily involved with the meeting and contributed two landmark papers to the topical issue of Chemical Geology on the use of secondary ion mass spectrometry to analyze volatiles in melt inclusions. When the melt inclusion community re-convened at Woods Hole Oceanographic Institution in August of 2018, we were saddened that Erik was unable to join us due to his failing health. Less than a month later came the devastating news of his passing at only 52 years of age. In recognition of his incredible contributions to science in general and to the *in situ* analysis of melt inclusions in particular, the participants and organizers of the WHOI melt inclusion workshop dedicate this collegial paper to Erik Hauri, our colleague, mentor and friend. Thank you Erik.

Introduction

Melt inclusions (MI) have long been recognized as unique petrologic indicators, starting with the classic descriptions of melt inclusions by Sorby in 1858. These small pockets of silicate, carbonate, sulfide and other types of melts entrapped within growing mineral grains have been used to study a wide range of topics, including mantle melting and sources (e.g. Saal et al., 1998; Hauri et al., 2006), pre-eruptive magmatic volatile budgets (e.g. Kovalenko et al., 2006; Hauri et al., 2011), volatile cycles in the mantle (e.g. Cabral et al, 2014), reconstruction of magma degassing (e,g. Dixon et al., 1995; Métrich and Wallace, 2008; Witham et al., 2012), the oxidation state of the upper mantle (e.g. Rowe et al., 2007; Moussallam et al., 2014; Hartley et al., 2017), the metal contents of ore-forming magmas (e.g. Zajacz and Halter, 2009) and partitioning behavior of elements and chemical species between minerals, melts and fluids (e.g. Zajacz et al., 2008). The information recorded by melt inclusions is unique because entrapped melts are physically isolated from most interactions with the external environment and preserved for later examination. The study of melt inclusions involves careful sample selection and

preparation, application of state-of-the-art analytical methods, and meticulous attention to potential artifacts related to post-entrapment processes. As the melt inclusion community has grown and access to *in situ* analytical techniques expanded, the number of publications using melt inclusion data has dramatically increased. The numbers speak for themselves: in 1990 there were about 10 publications on melt inclusions, which grew to 60–100 research papers in 2000, to more than 300 publications in 2017–2018 (source: Science Direct, using keywords search for "melt inclusion" in the abstract or title. We note that ISI referencing might not have accounted properly for the abundant untranslated foreign literature on the subject, but our point on the increase of publication remains). It is therefore important to periodically assess the state of the field. In August of 2018, a melt inclusion workshop – attended by 74 researchers from 14 countries – was convened at Woods Hole Oceanographic Institution (WHOI) with this goal in mind.

Much of the collective knowledge amassed by the melt inclusion community is passed along from one lab to another *viva voce*, making it difficult for a motivated novice to know where to start. One outcome of the WHOI melt inclusion workshop was a set of recommended practice guidelines for collecting and reporting melt inclusion data. They are appropriate for silicate melt inclusion compositions and mainly applicable to olivine host-mineral phases, but *in situ* analytical methods can be adapted to other host minerals. These guidelines are presented here as a resource for the broader melt inclusion community.

Several reviews dedicated to melt inclusions have been published and deal with sample preparation, composition corrections, and in situ analytical techniques (e.g. Lowenstern 1995, 2003; Frezzotti, 2001; Schiano, 2003; Webster and Thomas, 2006 for felsic plutons; Kent, 2008; Cannatelli et al., 2016). Here we often refer to these reviews and also build on them by extending the discussion to the use of analytical techniques of recent application to the study of glass inclusions (e.g. 3D XRT, XANES). We provide a detailed treatment of the problems encountered in data analysis and interpretation, accompanied by a summary of the recommended practices for the study of inclusions. The paper is divided into three complementary sections. The first section discusses protocols for choosing appropriate melt inclusions for study, documenting their textural characteristics. The second section describes recommended practices for commonly used

analytical techniques. The last section discusses the compositional corrections that can be made to account for post-entrapment modifications and to the presence of a bubble. We summarize the corrections that can be made to analytical data to account for those modifications, as needed.

One objective of this paper is to provide the scientific melt inclusion community with a resource documenting how to collect and process high-quality melt inclusion data and to suggest guidelines for the type of data that should be reported and included in publications. Adherence to these guidelines will bring some uniformity to characterizing melt inclusions and reporting those characteristics, making the data much more useful for application to future studies. As you read through the text, it is instructive to remember the words used by Henry Clifton Sorby to close his 1857 address before the Geological Society of London: *"I argue that there is no necessary connexion between the size of an object and the value of a fact, and that, though the objects I have described are minute, the conclusions to be derived from the facts are great."*

1. Melt inclusion selection and correcting for post-entrapment processes

1.1. Choice of melt inclusions

What is the pre-eruptive magmatic volatile budget of a volcano? What is the nature of the mantle source region for mafic magmas from different tectonic and geodynamic environments? How much water can be lost or gained by melt inclusions through post-entrapment diffusive processes? What is the cooling history of a crystal? What was the metal content of the ore-forming melt? How are elements partitioned between melts, minerals and fluids? These are examples of questions that can be addressed using data from melt inclusions.

The first step in any melt inclusion study is to identify the problem or question that is being addressed. This information is required to select the appropriate melt inclusions for study, and to identify the various steps one should follow to obtain the highest quality and most detailed information from the melt inclusions. Filtering out the cracked melt

inclusions (which can occur during eruption or during laboratory re-heating) or not fully enclosed melt inclusions is the second step to melt inclusion selection. If, *a priori,* this is difficult to do, then an *a posteriori* criterion for distinguishing such inclusions is that they typically have very low volatile contents (e.g. Nielsen et al., 1998) and, in the case of cracked (decrepitated) melt inclusions, a relatively large vapor bubble. In many cases, especially with slowly cooled lava flow samples, some or all of the melt inclusions may be crystallized to various extents, and this, in turn, determines the steps required to prepare the inclusions for analysis. Thus, rapidly quenched, glassy melt inclusions such as those that can be found in tephra samples, can be exposed and analyzed directly, whereas crystallized melt inclusions may require heating and homogenization before exposure. If the goal is to determine the pre-eruptive volatile content of the melt, a homogeneous (glassy) melt inclusion is required, and naturally quenched inclusions are preferred, because they will reduce the extent to which rapid diffusion of hydrogen through the host mineral may have reduced the melt inclusion H_2O concentration. Conversely, if the goal is determining the metal (Cu, Au, Zn, etc.) content of the melt associated with ore formation, crystallized MI can be analyzed as is, using LA-ICP-MS to determine the metal content.

 The nature of the melt inclusions in any given sample is a function of the history of trapping and later evolution of the host rock, and can produce MI that range from being totally homogenous and glassy to those that are completely crystalline. Student and Bodnar (1999), for example, discuss the various processes that determine the phase state of MI "as found". Both types of melt inclusions (glassy and crystalline; photos. Fig. 1A and C, respectively) are potentially useful, depending on the question or problem being addressed, and glassy melt inclusions are not always "better" than crystalline melt inclusions.
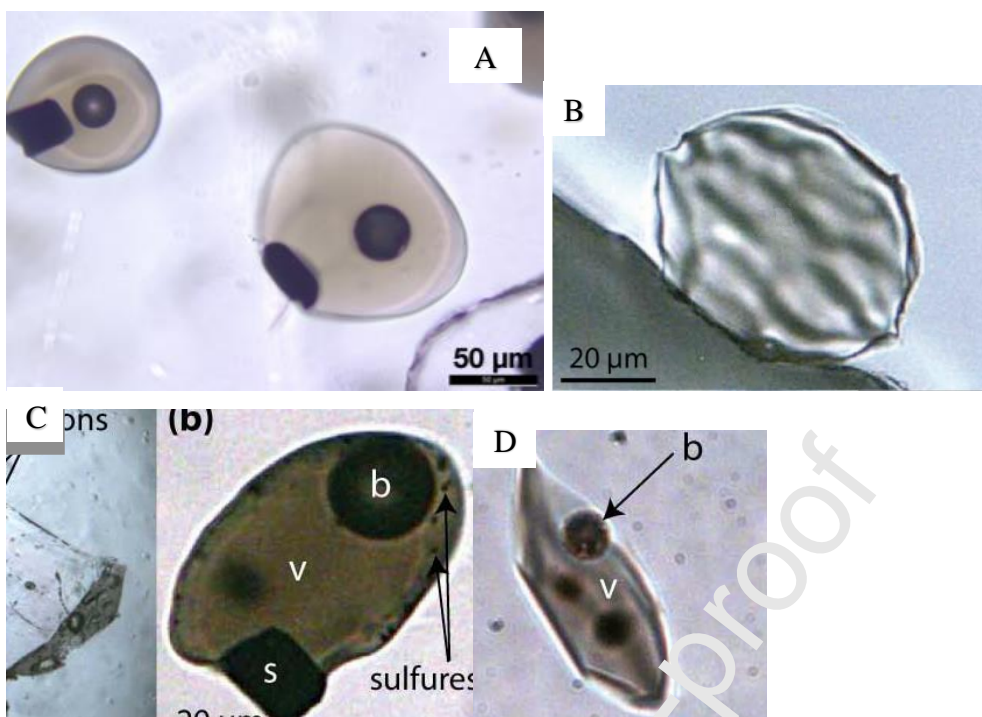
Fig. 1: (A) photomicrograph of two glassy olivine-hosted melt inclusions from the Ambae volcano. Inside both inclusions, we can see the very circular bubble and the angular spinel grains. (B) Sometimes the melt adopts the faceted crystal shape of the host mineral giving this Sommata melt inclusion this "raisin" aspect. (C) Backscattered electron image of a crystallized inclusions from Mount Shasta, with microcrystals (m), several small bubbles (b) and matrix glass. (D) picture in transmitted light of a devitrified melt inclusion from Pan de Azucar volcano (pictures B, C and D from Le Voyer, PhD 2009).

Glassy melt inclusions with no bubble are not necessarily less affected by post-entrapment crystallization compared to crystallized melt inclusions. It may just be less obvious, and one may still need to correct for the compositional effects of post-entrapment modifications (see section 3). There is not one single procedure that is applicable to all melt inclusions, or to all questions being addressed. Rather a variety of approaches can and should be applied, depending on the nature of the melt inclusions and the question you want to address.

Because melt inclusions often experience post-entrapment modifications, it is critical to assess whether the MI to be studied have recorded and preserved the original conditions at trapping, and this can be addressed through the study of melt inclusion assemblages (MIA). The concept of MIA is based solely on petrographic observations and echoes the definition for fluid inclusion assemblages that is, groups of melt inclusions that were all

trapped at the same time (e.g. Sobolev and Kostyuk, 1975; Roedder, 1979; Bodnar and Student, 2006; Cannatelli et al. 2016). A MIA is often identified as a group of melt inclusions that occur within a three-dimensional grouping within a phenocryst, or are distributed along either growth surfaces or healed fractures. Excellent examples of MIAs are shown in Bodnar and Student, 2006, (Figs. 1-5 and 1-15) and Esposito et al., 2014, (Figs. 3 and 4). Tools such as cathodoluminescence (CL) zoning in quartz (Peppard et al., 2001) or phosphorous (P) zoning in olivine obtain by electron probe or nanoSIMS (e.g. Milman-Barris et al., 2008; Welsch et al., 2014; Shea et al., 2019; Manzini et al., 2017b) can be combined with petrographic observations to help identify MIAs. Melt inclusions are usually best investigated in polished thin or thick sections. Similar chemical composition of all of the melt inclusions in an assemblage indicates that the melt inclusions all trapped a single homogeneous phase (melt) that has not been modified after trapping or that all of the melt inclusions in the MIA experienced the same extent of modification.

1.2. Textural features, imaging of melt inclusions and orientation of the crystal

Melt inclusion textures (shapes, sizes, and distributions within crystals) are often overlooked in favor of compositional data, yet they can hold information on magmatic processes, conditions, and timescales. For example, several studies have noted that melt inclusion morphologies vary from irregularly-shaped to ellipsoidal to faceted (negative crystal shape giving the inclusion a "raisin-like" aspect; Fig. 1B; e.g., Chaigneau et al. 1980, Beddoe-Stephens et al. 1988, Manley 1996, Anderson et al. 2000, Gualda et al. 2012) and a geospeedometer based on faceting of quartz-hosted melt inclusions was recently proposed, which can be used to assess quartz crystallization timescales and growth rates (Gualda et al. 2012; Pamukcu et al. 2013, 2015, 2020). Combining such information from melt inclusion textures with melt inclusion and/or host crystal compositions can be an especially powerful approach to understanding magmatic systems.

Given the small size and three-dimensional (3D) nature of melt inclusions, high-resolution 3D methods are necessary for accurate quantification of their sizes and shapes

(Richard et al., 2018). The spatial distribution and context of melt inclusions within crystals also has implications for interpreting 2D images and compositional data (Créon et al., 2018). In particular, an unexposed melt inclusion hidden below the crystal surface may affect CL intensities and backscattered electron signals, as well as compositional analyses from electron and scanning electron microprobes, depending on the excitation volume for a given set of beam conditions.

Traditionally, optical microscopy has been the primary method for describing and documenting melt inclusion textures, yielding 2D information. For example, melt inclusion size and position inside the grain should be reported (see Supplementary Table S1 for templates). As an example of why this is important, larger inclusions located in the interiors of large olivine host-crystals are less susceptible to H diffusive loss (e.g. Qin et al., 1992; Chen et al., 2011; Gaetani et al., 2012), therefore their H_2O contents are more likely to represent the pre-eruptive H_2O content. Another important consideration is that the lack of correlation between bubble size and melt inclusion size in MIAs may indicate heterogeneous entrapment of vapor in some of the melt inclusions (e.g. Sobolev and Kostyuk, 1975; Roedder, 1979; Steele-MacInnis et al., 2017).

Increased accessibility of 3D X-ray tomography (XRT) and the development of new methods for imaging materials with XRT allows for rapid (minutes to hours), non-destructive, high-resolution (≤ 1 μm/voxel) 3D imaging of crystals and their melt inclusions (e.g. Richard et al., 2018). This has significantly increased the accuracy and precision of quantitative measurements of melt inclusion textures; however, the approach is not without its shortcomings, and the following points should be considered when deciding to use 3D XRT for studies of melt inclusion in crystals:

(i) Low density contrast between melt inclusion and most mineral host phases (e.g., rhyolitic melt inclusions in quartz) precludes the use of standard XRT approaches and grayscale filtering for image processing. Under these circumstances, propagation phase-contrast XRT can instead be used to enhance object edges, and edge-detection algorithms can be used for image processing (see Pamukcu et al., 2013). However, this approach is most effective on synchrotron-based XRT systems, where the sample-to-detector distance can be changed significantly.

(ii) Imaging with synchrotron-based XRT has the advantage that analyses are relatively quick (~15–30 minutes) and the systems typically do not charge user fees (except in cases of proprietary research). However, users generally have to submit research proposals, and obtaining time on these systems can be competitive. Consequently, access and data collection are limited by proposal acceptance, time allotted, and – in some cases – cost. In addition, for these setups, crystals are typically imaged individually (depending on their size). In comparison, access and costs for desktop XRT systems are lab-specific, and analyses can take much longer (up to 12+ hours), although multiple crystals can often be scanned at once. In both cases, substantial time may be required for image processing (up to hours for individual melt inclusions). Large datasets (up to tens of GB) may require significant computing resources (i.e., large number of CPU cores and memory). Future developments in image processing methods may substantially reduce the time and computing power required for this step.

Precise imaging of crystals is also valuable for assessing potential H diffusive loss from melt inclusions, in order to make the best estimates of actual magmatic H_2O values at the time of trapping. Any elemental diffusion work requires careful crystal orientation and good practices are reviewed in detail in Shea et al. (2015). With H diffusion being so anisotropic in most mineral hosts, it is important that melt inclusions should be sectioned with attention to crystallographic orientation, ideally in oriented crystals. The H diffusivity parallel to a particular crystallographic direction is faster than you find in bulk studies (Ferriss et al., 2018; Barth et al., 2019) from the dehydration-hydration experiments on unoriented olivines that contain melt inclusions (e.g. Portnyagin et al., 2008; Gaetani et al., 2012, 2014; Chen et al., 2011, 2013). Recently published experimental results provide new volume diffusivities for the highly anisotopic diffusion that can lead to large errors in interpretation, specifically for olivine-hosted melt inclusions close to a crystal edge (Barth et al., 2019; Barth and Plank, 2021).

Recommended practices:

The first step in a melt inclusion study is to conduct a detailed petrographic examination to determine the range in sizes, shapes, textures and distribution of MI within host phenocrysts. An example of presentation is given in a template table (Table S1) with the

11

size of the inclusion, the size of a vapor bubble, indication of the presence of daughter minerals or quench crystallization, and the shortest distance to the rim of the crystal, (when available the shortest distance to the edge of the crystal along the a axis), should be documented and reported in the supplementary material (see template Table S1). This information is critical to selecting MI that are related to the geologic question or problem being addressed, and to identify MI that may have been modified following trapping. Conventional petrographic examination of the MI may be sufficient in many cases, or may be supplemented by cathodoluminescence (CL) imaging of MI in quartz (e.g., Peppard et al., 2001), major and minor element mapping by electron microprobe, phosphorous zoning in olivine (e.g., Welsch et al., 2014; Manzini et al., 2017b), or 3D propagation phase-contrast XRT, to better constrain the physical characteristics of the MI and their relationship to host-crystal growth. Subsequent analyses of these crystals and melt inclusions, and interpretation of results, should take melt inclusion textures into account. While precise textural analysis requires considerable effort, the extent of detailed imaging is also dependent on the question being addressed, so microscope imaging might be sufficient. We recommend reporting imaging conditions, image resolution, and any image processing approaches used on 3D datasets. During image processing, be careful not to overwrite the original data.

1.3. Rehomogenization

Determination of the chemical compositions of melt inclusions (major, trace, and volatile elements) is essential for using melt inclusions to interpret magmatic processes. For partially or fully crystalline melt inclusions, rehomogenization experiments requires heating to re-melt crystals in the inclusion, followed by rapid cooling to quench the melt to glass (fundamentals of the method are described in Sobolev and Kostyuk 1975; Roedder, 1979, 1984; Danyushevsky et al., 2002; Schiano, 2003). Rehomogenization experiments can be performed in three ways: in a microscope heating stage (e.g. Sobolev et al., 1980), in a 1-atm furnace (e.g. Sinton et al.,1993), and heating the melt inclusions in an internally heated pressure vessel (e.g. Mironov et al., 2015). The first two procedures were compared using quartz-hosted inclusions and have been extensively discussed elsewhere (Student and Bodnar, 1999). They concluded that the temperature of rehomogenization is independent of inclusion size when the procedure is performed in a 1-atm furnace with a small heating rate (10 ºC per minute), and the temperature of rehomogenization corresponded to the known temperature of formation. In contrast, in a

microscope heating stage, the temperature of rehomogenization is higher than the formation temperature and a positive correlation exists between the size of the quartz-hosted melt inclusions and the heating rates. Student and Bodnar's (1999) advice for quartz-hosted melt inclusions was to use the data of the smallest melt inclusions that were rehomogenized with slow heating rates (<1 ºC/min). The 1-atm furnace procedure can be wasteful of material since rehomogenization temperature estimates are done after the experiments, requiring several initial test-runs, but larger crystals (>2mm) with potentially larger inclusions (up to 500µm) can be studied (e.g. Nielsen et al., 1998). As for the microscope heating stage the method is more time consuming because crystals are individually heated in the stage, but the visual inspection during heating allows the disappearance of the last daughter crystal to be observed, thus yielding an accurate rehomogenization temperature (also called homogenization temperature; T_h). In the case of olivine-hosted melt inclusions, the positive correlation between temperature of homogenization and the forsterite content of the host olivine observed in basaltic rocks (e.g. Sobolev and Nikogosian, 1994), can be a method to check the reliability of homogenization temperatures.

While the goal of heating experiments is not usually to determine the entrapment temperature, the entrapment temperature can be determined if the melt inclusions are re-heated under a confining pressure that is equivalent to the trapping pressure (see discussion in Student and Bodnar, 2004; Cannatelli et al., 2016). In a 1-atm furnace or in a microscope heating-stage, temperature of homogenization (T_h) of melt inclusions systematically increase with time during successive heating experiments, regardless of their major element composition and their H_2O content, likely due to deformation of the inclusion in response to the pressure gradient between the inclusion and the exterior of the host olivine (e.g. Sobolev and Danyushevsky, 1994; Massare et al., 2002; Tison, 2006; Schiavi et al, 2016).

Rehomogenization of melt inclusions affect the original trapped composition of the fast diffusing elements: care must be taken to assess the extent to which the heating procedure may have affected volatile concentrations, especially H_2O, in the melt inclusions. For example, diffusive exchange is strongly temperature-dependent, with experimental

studies showing that complete diffusive exchange of H_2O between a melt inclusion and the external melt surrounding a 1-mm-diameter host olivine occurs within 2 days at 1250°C (Gaetani et al., 2012), whereas even after 2 days complete equilibrium will not be attained at 1140 °C (Portnyagin et al., 2008) and no reequilibration occurs over 2 days at 1100 °C (Bucholz et al., 2013). Careful homogenization procedures are required to minimize H_2O loss (e.g. Chen et al., 2011; <10 min above 1200 °C for a 20-µm-radius melt inclusion in a 300-µm-diameter olivine will not produce significant H_2O loss). Due to the strong anisotropy of H+ diffusion in olivine, water loss from melt inclusions is dominated by diffusion along the crystallographic "a" axis of the olivine (the fast diffusion direction; Barth et al., 2019; Barth and Plank, 2021, H_2O loss during homogenization is much slower in quartz because of the lower temperatures of rhyolitic magmas; Severs et al. (2007) documented insignificant H_2O loss after 12 hours of heating at the inferred trapping temperature of 800 °C at a confining pressure of 1 kbar, but significant loss did occur over days to a week.

It is now established that one conclusive test for proton diffusion during homogenization is to confirm that there is no negative correlation between H_2O content and the D/H isotope ratio. Gaetani et al. (2012) and Bucholz et al. (2013) assess the consequence of diffusive re-equilibration using the MATLAB script given in Bucholz Appendix B. Other volatile elements like Cl and F are not affected by diffusive re-equilibration during homogenization (Bucholz et al. 2013), but it is not clear yet if S is sensitive to diffusion through the olivine host.

Another post-entrapment effect that can be investigated using homogenization experiments is the transfer of low-solubility CO_2 to a bubble. Homogenization experiments in a heating stage (Wallace et al., 2015), a 1-atm furnace (Tuohy et al., 2016), an internally heated pressure vessel (Mironov et al., 2015), and a piston-cylinder apparatus (Rasmussen et al., 2020) have all been successful in redissolving CO_2 in bubbles back into the melt (see also Moore et al., 2018). Transfer of CO_2 from the melt into vapor bubbles is discussed in more detail in the last section of this article.

Recommended practice:

Fundamental historical references for experimental homogenization exist describing in detail the method and the pitfalls of the procedure (Roedder, 1979, 1984; Student and Bodnar, 1999; and review by Lowenstern 1995) and for the different heating method that can be used (e.g. Schiano, 2003; Chen et al., 2011). If possible, visual inspection during homogenization of inclusions is recommended, requiring the use of a heating stage. Ideally one should do initial tests of heating procedures on a few melt inclusions to determine the homogenization temperatures of the MI before adopting a specific protocol for a given sample. If sample material is abundant, and a bit can be sacrificed, the 1-atm furnace heating method is equally effective, and is often more readily available in laboratories. One of the rare studies comparing the two methods reports similar results with both (on Koolau, Hawaii, melt inclusions; Norman et al., 2002).

Diffusive H_2O loss can occur during magma ascent in nature and during heating in the laboratory. The best evidence that melt inclusions have experienced loss of H_2O (or other volatiles) is if the melt inclusions within a melt inclusion assemblage (assuming that all inclusions were trapped under the same conditions) show variable concentrations, as any type of modification, including H_2O loss, depends on inclusion size, shape, location within a crystal, and other factors. Diffusive H_2O loss may be identified through a negative correlation between H_2O and D/H. If you do not have access to a SIMS for D/H measurements, then a positive correlation between melt inclusion diameter and H_2O concentration is a sign that diffusive loss of hydrogen has occurred. If diffusive loss occurred during ascent, the largest, most H_2O-rich inclusions provide the closest estimate for pre-eruptive H_2O concentration in the melt, though even the highest value may be lower than the original magmatic values.

2. Melt inclusion analysis

We hereafter summarize the different analytical techniques that can be used to characterize melt inclusion (Fig. 2). They are reported as a function of their destructive impact on the integrity of the melt inclusion and should they all be needed, they should be performed in the order described. The durations of sample preparation and measurements times associated with each analytical technique are highly variable, reflecting the complexity, pitfalls, and/or availability of certain instruments.

Some recommended practices are independent of analytical methods and common to all of them. An obvious example is to include a photomicrograph of each MI in supplementary data. The photomicrograph should show the location of each analysis within the MI and the surrounding host phase, or provide a labeled post-analysis

photomicrograph showing the spots, such as laser ablation pits. Also, using the same identifier on the photo and in the data tables allows easy comparisons.
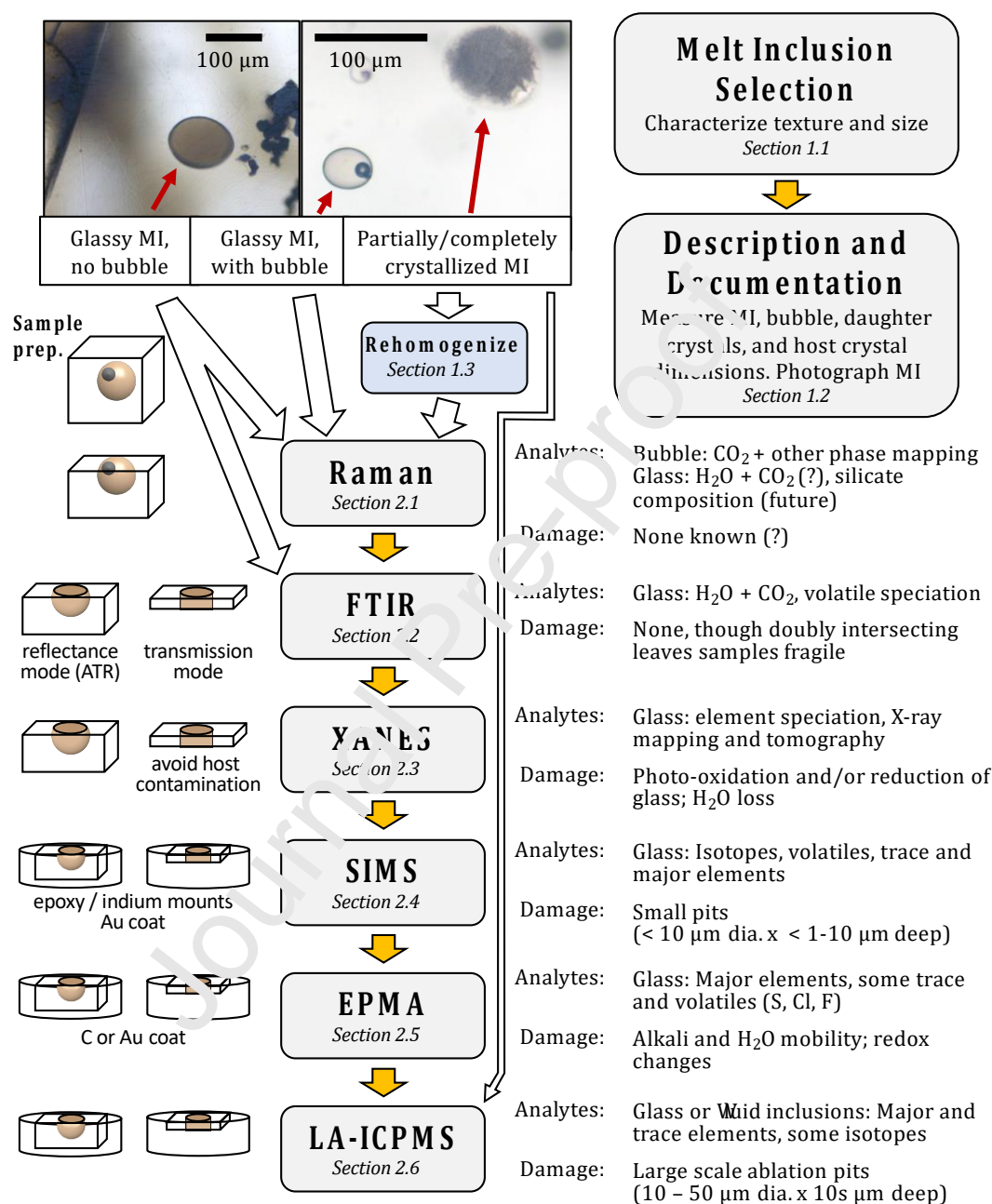
Fig. 2: Idealized flow-chart for melt inclusion (MI) sample analyses given sample preparation and analysis-induced damage considerations (Lerner, 2020). Depending on the intended research, particular steps may be skipped. Samples can be re-polished to remove upper surfaces that were damaged by various techniques (EPMA, SIMS, LA-ICPMS). See text for references and for more details on preparation and recommended practices for MI sample selection, MI homogenization, each for analytical technique.

16

Melt inclusions in inset photos are from Kīlauea Volcano's 2018 Lower East Rift Zone eruption.

2.1. Raman spectrometry

Raman spectrometry is a non-destructive analytical technique that has been applied to both fluid and melt inclusions for well over 50 years. Indeed, motivation for development of the Raman spectrometric technique was driven in part by the need for an analytical method that could be applied to the tiny fluid and melt inclusions contained in natural samples (Delhaye and Dhamelincourt, 1975; Rosasco and Roedder, 1979; Dhamelincourt et al., 1979; Rosasco et al., 1975). Modern Raman systems allow for the rapid analysis of any form of matter (solid, liquid or vapor) that contains covalent bonds and is Raman active, with approximately 1μm spatial resolution. The time required to complete a single analysis varies greatly as a function of the scattering efficiency of the species being analyzed, the concentration of the species in the analytical volume, background noise from the sample, including fluorescence, and interference from other species that show Raman bands that overlap with those of the species of interest. For more details on the Raman technique in general, and its application to fluid and melt inclusions, the reader is referred to Burke (2001), Frezzotti et al. (2012), Thomas and Davidson (2012) and Bodnar and Frezzotti (2020). Raman spectrometry has been applied to melt inclusions in three general areas: (1) to determine the volatile contents of silicate (and other) glass phases contained in melt inclusions (e.g. Chabiron et al., 1999; Zajacz et al., 2005; Thomas et al., 2006; Mercier et al., 2010; Morizet et al., 2013, 2017); (2) to identify and quantitatively analyze the volatile species contained in vapor bubbles in melt inclusions (e.g. Moore et al., 2015; Aster et al., 2016; Hanyu et al., 2020); (3) to identify solid phases contained in bubble (e.g. Liptai et al., 2020; Schiavi et al., 2020) or in melt inclusions that have undergone partial to total crystallization following trapping (e.g. Mernagh et al., 2011).

The Raman technique can be applied to melt inclusions that are exposed at the sample surface as well as to those that are beneath the surface and totally enclosed by the host crystal – this allows the mutual spatial relationships between the different phases to be preserved for multi-phase melt inclusions. The glass phase in melt inclusions is analyzed

17

by focusing the laser beam at the surface or slightly below the surface. Spectra are generally obtained in two ranges, the 150–2000 cm^{-1} range (to cover aluminosilicate framework vibration) and 3000–4000 cm^{-1} range (to cover OH-stretching) relative to the exciting laser light (Fig. 3).
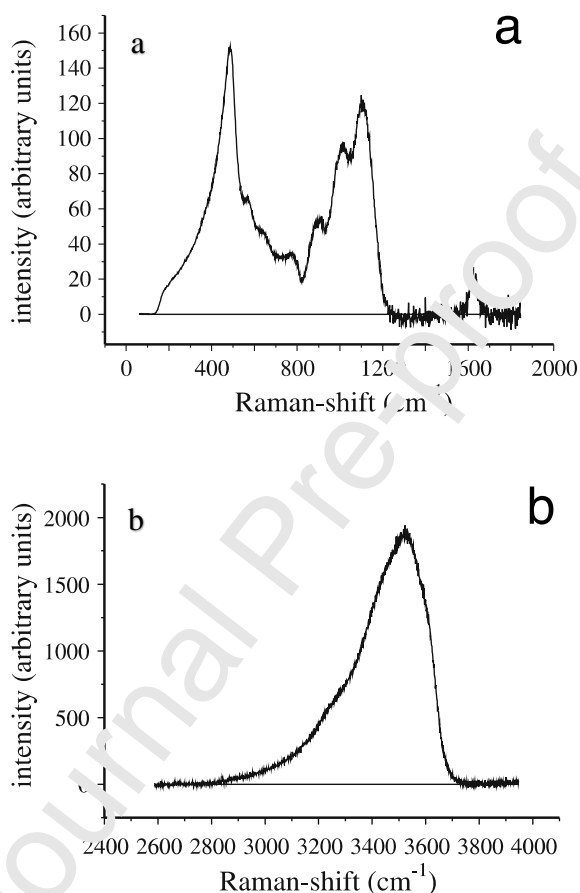
Fig. 3: Raman spectra after frequency-temperature correction (a) of the aluminosilicate framework vibration range and (b) of the OH-stretching range ("water band").

Determining the H_2O and CO_2 concentrations of melt inclusion glass by Raman spectroscopy (McMillan, 1984) has become common in melt inclusion studies (e.g. Thomas, 2000; Thomas et al., 2006; Chabiron et al., 2004; Zajacz et al., 2005; Mercier et al., 2010; Morizet et al.; 2013; Créon et al., 2018). Thomas (2000) proposed a simple technique to determine the H_2O content of melt inclusion glass by comparing the intensity of the Raman H_2O band with that obtained from a glass standard with known H_2O content collected at identical analytical conditions. Zajacz et al. (2005) described a

18

method that corrected the intensities of the Raman band for H_2O to account for differences in the glass composition that affect intensity, thus eliminating the effect of glass composition on the estimated water content. Severs et al. (2007) applied Raman analysis to determine the H_2O content of rhyolitic-composition melt inclusion, and used a UV (244 nm) laser to eliminate fluorescence background that is commonly associated with analyses using a green (514 or 532 nm) laser. In some cases, Raman is the only method (other than, perhaps, nano-SIMS) to analyze the very small (~5 μm) "nano-granite" melt inclusions that occur in anatectic samples formed in the deep crust (Bartoli et al., 2013). Compared to H_2O, researchers have had less success in determining the CO_2 concentration in glass by Raman analysis, mostly because the CO_2 bands overlap with many of the bands produced by the silicate species in the glass, and because carbon occurs in more than one structural state in the melt (glass) (Mysen and Virgo, 1980; Morizet et al., 2013). In spite of these complications, Morizet et al. (2013) developed a method to quantify the CO_2 content of the glass using area under the carbonate v_1 peak(s) and the area ratio for the aluminosilicate peaks in the range 700–1200 cm^{-1}. The authors report that the calibration is valid from 0.2 to 16 wt.% CO_2 with an analytical precision of ±0.4 wt.% CO_2. The ideal melt inclusion to study is one that contains only a homogeneous glass (melt) phase at ambient surface conditions.

In some cases, especially for melt inclusions contained in lavas or in plutonic rocks, the melt inclusions may have undergone complete crystallization during cooling. Such melt inclusions are often difficult to identify and analyze, and are often overlooked during normal petrography (Yang & Bodnar, 1994; Thomas et al. 2002; 2003; Bodnar & Student, 2006). In most cases, the crystals in the melt inclusions are fine-grained and intergrown with other crystals, making their identification using petrography or SEM difficult if not impossible. Occasionally, however, such phases are large enough to be analyzed by Raman in order to identify the minerals. Thus, Student and Bodnar (2004) were able to identify the presence of feldspar in crystallized melt inclusions from the Red Mountain, Arizona, porphyry copper deposit using Raman spectroscopy. Similarly, Mernagh et al. (2011) were able to identify alkali-Ca carbonates, with varying proportions of cations, and Na-Ca-Ba sulphates (without any evidence of H_2O) in melt inclusions from "dry" kimberlites, whereas melt inclusions from "wet" kimberlites were

19

found to contain bassanite, pirssonite, and hydromagnesite, consistent with higher amounts of water in the residual magmas. In melt inclusions in eclogitic diamonds Shatsky et al. (2019) identified clinopyroxene using *in situ* Raman analysis. Raman can also be used to detect the presence of nanolites in the glass (magnetite nano-crystals 30–1000 nm in diameter) by a peak at ~670 cm^{-1} (Mujin et al., 2017; Di Genova et al., 2017; 2018).

Among the more significant developments in melt inclusion research in recent years has been the growing recognition that the vapor bubbles in melt inclusions are important reservoirs for volatiles contained in the originally trapped melt. Perhaps the first researcher to recognize the importance of vapor bubbles and attempt to include the contents of the vapor bubble in estimates of formation pressures of melt inclusions was Fred Anderson (Anderson and Brown, 1993), who recognized that the CO_2 content of the glass phase in bubble-free and bubble-bearing melt inclusions from the 1959 eruption of Kilauea Iki was different. These workers further summarized that the "missing" CO_2 in the bubble-bearing melt inclusions was contained in the vapor bubbles and then reconstructed the CO_2 content of the trapped melt based on the bubble size and assumptions concerning the amount of CO_2 in the bubbles using an equation of state. More recently, various researchers have shown that the Raman spectrum of CO_2 varies as a function of CO_2 density (or pressure) and densimeters describing the relationship between splitting of the Fermi diad and CO_2 density (pressure) have been developed (see a summary and comparison of the various densimeters in Lamadrid et al., 2017). Esposito et al. (2008; 2011) combined the earlier methodology described by Anderson and Brown (1993) with the Raman densimeters that had recently been developed to describe a method to reconstruct the volatile contents of melt inclusions by accounting for CO_2 in the vapor bubble. The results showed that a large proportion of the CO_2 in a melt inclusion is hosted in the bubble. Therefore, the CO_2 content of the glass alone, and therefore calculated saturation pressures are significantly under-estimated if the CO_2 content of the bubble is ignored. This has led to a series of studies that applied the Raman densimeter to determine the density of CO_2 in the bubble, followed by a reconstruction of the CO_2 content of the melt that was originally trapped in the melt inclusions (Hartley et al., 2014; Moore et al., 2015; Wallace et al., 2015; Aster et al., 2016; Drignon et al,

20

2019a, b; Hanyu et al., 2020). The amount of CO_2 in a melt inclusion vapor bubble that can be detected and quantified depends on the density of the CO_2 in the bubble and the depth of the bubble beneath the surface. In general, the CO_2 content of a vapor bubble that is a few μm or less beneath the polished surface and has a density of greater than approximately 0.05 g/cm^3 can be quantified. An important result of the several recent studies that have been conducted to analyze the proportion of the total CO_2 in the melt inclusions that is contained in the vapor bubble demonstrates that between 30 to 90% of the CO_2 is present in the vapor bubble. This has important implications concerning the estimated entrapment pressures and degassing paths. Analysis of the vapor bubble in melt inclusions at room temperature is challenging because at these conditions the H_2O that was in the original single fluid phase that exsolved from the melt has condensed to form a thin (nanometer scale) film of liquid H_2O at the bubble-glass interface (Esposito et al., 2016) . However, if the melt inclusion is heated slightly, the liquid H_2O evaporates into the CO_2-rich vapor to produce a homogeneous fluid containing both H_2O and CO_2. Analysis of the bubble at elevated temperature then shows peaks for both H_2O and CO_2, and their relative concentrations can be determined from the peak areas (Berkesi et al., 2009; Lamadrid et al., 2014). As researchers have begun to focus on the analysis of the vapor bubbles in melt inclusions, they have started to recognize other features associated with the volatile components in or adjacent to the vapor bubbles. For example, using Raman spectroscopy, Kamenetsky et al. (2002) identified carbonates, sulfates, sulfides and hydrous silicates at the interface between the vapor bubble and the glass in melt inclusions from various tectonic settings, including mid-ocean ridges, ocean islands, and various modern and ancient backarc–island arc settings. They suggested that the various phases precipitated after the melt inclusions were trapped and a vapor bubble formed. The volatile components in the vapor bubble (CO_2, H_2O, S) likely interacted with (1) the glass in the melt inclusion, (2) the film of liquid H_2O, and/or (3) with other species in the vapor phase (Ca, Na, Fe, Mg, etc.) to form the carbonates, sulfates, sulfides and hydrous silicates identified by Raman analysis. Similarly, Esposito et al. (2016) identified liquid H_2O, native sulfur and calcite at the interface between the vapor bubble and glass in melt inclusions from the Mount Somma-Vesuvius volcano, Italy, and Moore et al. (2018) identified magnesite, native sulfur and arsenopyrite in vapor bubbles from Klyuchevskoy

21

volcano, Kamchatka. Li and Chou (2015) identified hydrogen (H_2), as well as CH_4, N_2, H_2O, disordered graphite, and possibly higher hydrocarbons, in silicate melt inclusions in quartz from the Jiajika granite in China. These and other studies show that in order to obtain an accurate assessment of the volatile budget of melts using melt inclusions, both the fluid and solid phases in the vapor bubbles must be quantified and used to reconstruct the original melt composition. An important recent development in Raman spectroscopy that has been applied to melt (and fluid) inclusions is the Raman mapping technique, whereby a 2- or 3-D map showing Raman spectral properties is used to identify and determine the spatial distribution of phases within melt inclusions. Thus, Guzmics et al. (2019) constructed a 3-D Raman map of the vapor bubble within a silicate melt inclusion in nepheline phenocrysts from the Kerimasi volcano in the East African Rift and identified, in addition to a CO_2 fluid, crystals of natrite (Na_2CO_3) and nacholite ($NaHCO_3$) within the bubble. The nacholite is thought to have formed as a result of subsolidus interaction of the CO_2-rich fluid with the surrounding glass.

Recommended practice:

Type of data produced:
Concentrations of H_2O and CO_2 in the melt and H_2O and CO_2 concentrations in the bubble. Identification of the minerals (Raman spectra) present inside crystallized melt inclusion and on the wall of the bubble.

Sample requirements:
Solid (glass or minerals) or fluid inside a solid with a flat polished surface.

Analytical conditions:
For analysis of CO_2 in bubbles, it is important to analyze samples of known CO_2 density to confirm the accuracy of the densimeter for the individual Raman instrument (e.g., Lamadrid et al. 2017). A densimeter calibration made on one Raman instrument should not be used on other instruments. Raman can be used to determine the H_2O, and to a lesser extent, CO_2 in the glass phase of melt inclusions, and can identify H_2O, CO_2 and other volatiles in the vapor bubble.
For mineral identification, a conventional approach is to compare the sprectrum to that in database or published articles to identify the solids.

Analytical details:

22

For doing CO_2 in bubble by Raman, the inclusion doesn't need to be exposed, but the sample does need to be sectioned so the bubble is not too far beneath the surface.

Reporting requirements:
-Report the types of Raman instruments used since there are several commercially available.
-Report the different protocols that have been used to analyze melt inclusions with Raman, and describe in detail the analytical equipment and conditions so that results from different labs may be compared.
-Report how the Raman peak positions were calibrated when using peak position to determine compositions or densities.
-Describe any calculation methods to quantify the volatile contents of melt inclusions.
-Report calibration standards used, detection limits, precisions and accuracy.

2.2. *Fourier transform infrared spectroscopy*

Fourier-transform infrared spectroscopy (FTIR) is widely used to analyze H_2O and CO_2 species dissolved in silicate glass and minerals (e.g., see von Aulock et al., 2014). It has the advantage of being relatively inexpensive, easy to use, non-destructive during analysis, and capable of measuring the speciation and concentrations of H_2O and CO_2. The conventional method involves an infrared beam transmitted through a sample. In the ideal case, where melt inclusions are large enough, sample wafers are prepared so that the inclusion is exposed and polished on both sides and spectra are uncontaminated by the host crystal. This is a drawback of FTIR as preparing very small inclusions can be challenging or impossible. Vibrations of different bonds in H-O and C-O species absorb energy at specific wavenumbers. These absorbances are used with the Beer-Lambert law (Stolper, 1982) for calculating species concentrations. The Beer-Lambert law requires knowledge of the molecular weight of the absorbing species of interest, the sample density and thickness, and a composition-dependent molar absorption coefficient (also known as an extinction coefficient). Molar absorption coefficient values have been published for specific melt compositions (e.g., Table 1 in von Aulock et al., 2014), and there are also equations allowing them to be calculated as a function of melt composition (e.g., Mandeville et al., 2002) that can be used. Direct measurements of melt inclusion densities are impractical. As a result, density values are usually calculated on the basis of the chemical composition (e.g., Lange 1997; Ochs & Lange 1999). Thickness can be

measured directly (1) using a digital micrometer, (2) by viewing a sample wafer edgewise under the microscope and using the eye-piece reticle (Wallace et al., 1999), or (3) using a stage where the focus depth has been calibrated (e.g., Befus et al, 2012). Alternatively, the thickness of a sample wafer can be determined using the frequency of interference fringes over an interval of wavenumbers on a FTIR spectrum collected in reflectance mode (e.g., Tamic et al., 2001; Wysoczanski & Tani, 2006). In practice this method requires the knowledge of the refractive index (RI) of the material you are analyzing. You can obtain a more accurate measurement of the thickness of the host mineral immediately adjacent to the inclusion where you can use a larger aperture to get better reflectance spectra and because the host mineral's refractive index is easier to constrain than that of the glass phase (e.g., using Deer et al., 1997). There are errors associated with each of the parameters used in the Beer-Lambert law (Agrinier & Jendrzejewski, 2000), giving an overall error of about 10% relative on the species concentration. Examples of FTIR spectra you obtain are shown in Figure 4.
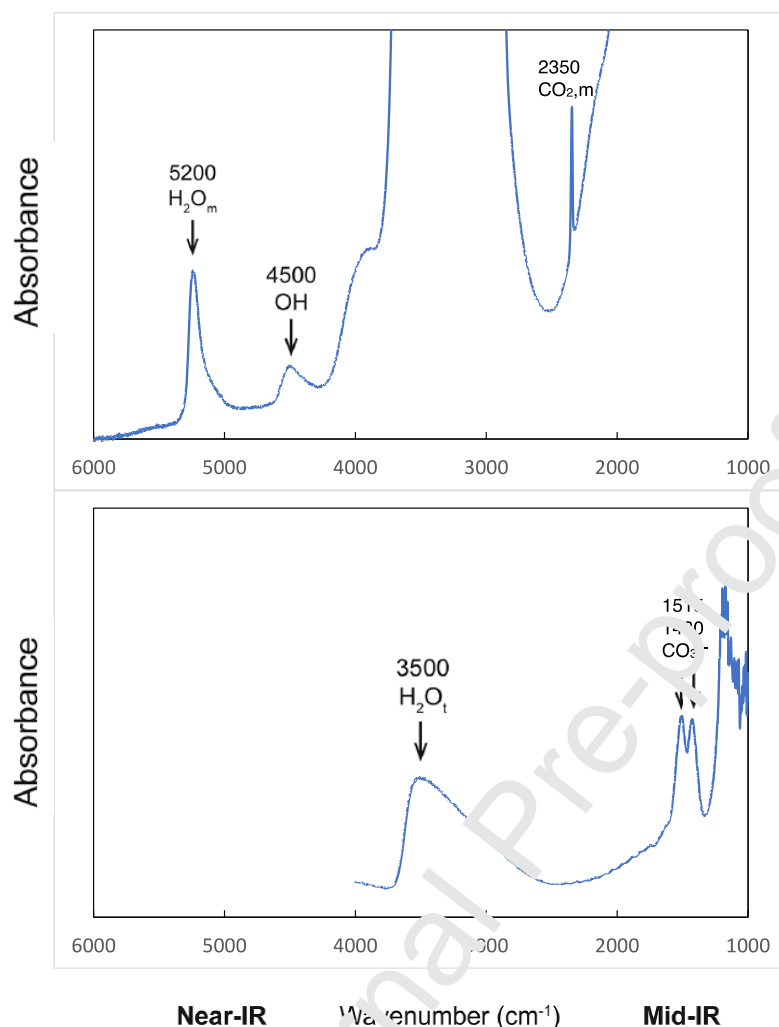
Fig. 4: H_2O and CO_2 absorption bands in FTIR spectra of hydrous rhyolitic (top) and basanitic (bottom) melt inclusions. In the rhyolite spectrum, the 5200 cm^{-1} (molecular H_2O) and 4500 cm^{-1} (OH) bands can be seen, but the mid-IR fundamental OH stretching band (3550 cm^{-1}), which gives total H_2O, is oversaturated. The 2350 cm^{-1} band (molecular CO_2) can also be seen. In the basanite spectrum, total H_2O is much lower and therefore can been seen at 3550 cm^{-1}. The doublet at 1515 and 1430 cm^{-1} is for dissolved carbonate, which is the primary solution mechanism for CO_2 in mafic compositions. Data are from Roberge et al. (2013) and Rasmussen et al. (2017).

Detection limits depend on sample thickness. Very low volatile contents can only be detected in thicker samples, whereas high volatile contents require thinner samples to avoid saturation of the detector. For example, the detection limits for a basaltic glass inclusion with a 50 μm thickness are ~0.02 wt.% H_2O (at ~3500 cm-1) and ~50 ppm CO_2

as carbonate (both depending on composition, which affects the molar absorption coefficient), but these limits are halved by doubling the wafer thickness to 100 μm. If inclusions are too small to be exposed on both sides, there are other methods that can be applied. Volatile contents of unexposed inclusions can be determined by the Beer-Lambert law as long as spectral contamination from the host crystal does not overlap with the absorbance bands of interest and the thickness of the unexposed inclusion within the host crystal can be measured (Befus et al., 2012). Unexposed inclusion thickness can be determined under the microscope as above, as the average of the dimensions of the inclusion in x and y orientations (Befus et al., 2012; this assumes the inclusion has a regular shape), or using spectral features (Tollan et al., 2019). For inclusions hosted in olivine, the thickness of the olivine in the beam path can be determined using peaks in the spectrum of the olivine host and then subtracting this from the overall thickness of the sample wafer (i.e., host crystal + inclusion) to obtain the inclusion thickness (Nichols & Wysoczanski, 2007). In an attempt to further simplify sample preparation, efforts have been made to calibrate reflectance FTIR spectra to calculate concentrations of H_2O and CO_2 species (Hervig et al., 2003). However, reflectance FTIR spectra are much less intense than those in transmitted light resulting in much higher detection limits (~0.5 wt.% water). To improve the signal to noise ratio and reduce detection limits, Yasuda (2014) has conducted FTIR measurements under vacuum using a narrow band detector, reducing detection limits to <0.3 wt.% H_2O. King & Larsen (2013) manipulate reflectance FTIR spectra using a Kramers-Kronig transform, which causes H_2O and CO_2 spectral bands to increase in intensity, enabling H_2O and CO_2 species concentrations to be calculated with errors of ~20% relative. More sensitive still is micro-attenuated total reflectance (ATR) FTIR (Lowenstern & Pitcher, 2013), where an ATR crystal is placed in contact with the sample surface. This has a detection limit of <0.2 wt.% H_2O and gives errors of about 20% relative. Unfortunately, none of these reflectance methods yields sufficiently low detection limits for either molecular CO_2 or carbonate to enable their analysis in melt inclusions. Use of a synchrotron source, instead of the conventional globar or tungsten-halogen white light bench source, will greatly improve the signal to noise ratio, and thus detection limits, on FTIR spectra in both transmitted and reflected light.

Recommended practice:

Type of data produced:
Concentrations and speciation of H_2O and CO_2.

Sample requirements:
Solid (glass or minerals) with a flat polished surface. Melt inclusions should be intersected and polished on both sides to avoid host contamination in the FTIR spectra whenever possible.

Analytical conditions:
The adjustable aperture in an FTIR microscope should be set as large as possible without overlapping into the adjacent mineral host. A background spectrum should be taken after each melt inclusion spectrum to ensure use of the same aperture setting. Most instruments are set up with both white light and IR (globar) light sources. The white light source provides better intensity for collection of near IR spectra, whereas an IR source is required for analysis of the carbonate doublet peak in basaltic glasses.

Analytical details:
Replicate spectra on a given melt inclusion should be taken with slightly different aperture sizes to check for consistency of results. Reflectance spectra taken to determine sample thickness should be measured on two or three spots on the mineral host adjacent to the inclusion.

Reporting requirements:
-Publish measured peak heights in a supplemental table.
-Report sample thicknesses, the absorption coefficients that were used to calculate concentrations, the background subtraction method used (e.g., straight line or flexicurve), and the reference used for density calculations.
-Inclusions that were not doubly intersected to avoid host contamination in the spectra should be noted and details given as to the correction scheme used to calculate H_2O and CO_2 concentrations.
-Report detection limits (if analyzed concentrations are very low), precision estimated from replicate spectra, and accuracy.
-Include sample spectra in supplemental material.

2.3. X-ray absorption near edge structure spectroscopy

X-ray Absorption Near Edge Structure (XANES) spectroscopy is sensitive to the electronic and structural properties of condensed matter. When combined with synchrotron radiation sources, XANES offers a relatively non-destructive *in situ* method for the determination of elemental valence state and coordination. Spatial resolution is instrument- and material-specific, but can reach 2×2 μm, making it particularly attractive for small specimens, like melt inclusions. The technique has broad applications and we refer our readers to excellent reviews, such as Henderson et al., 2014 and Sutton et al., 2020. Here, we limit ourselves to a discussion of Fe K-edge XANES in silicate glasses for the determination of of the relative proportions of ferric (Fe^{3+}) and ferrous (Fe^{2+}) iron – frequently quantified as $Fe^{3+}/[Fe^{3+}+Fe^{2+}]$, or the $Fe^{3+}/\sum Fe$ ratio. Iron's oxidation state can, in turn, inform investigators about the extent to which silicate melt inclusions are in equilibrium with their mineral hosts and allows investigators to calculate the oxygen fugacity (fO_2) recorded by melt inclusions.

The $Fe^{3+}/\sum Fe$ ratio in a glass can be quantified through empirical calibration of the spectra against the spectra of matrix-matched standards with known $Fe^{3+}/\sum Fe$ ratios. Therefore, accurate inter-facility/laboratory comparisons rely on acquisition of common, widely distributed, standards. Standards should be selected to match the composition of the unknowns as closely as possible. The Smithsonian Institution's National Museum of Natural History (NMNH) holds three sets of reference glasses of basaltic, andesitic and pantelleritic compositions (Cottrell et al., 2009; Zhang et al., 2016; Zhang et al., 2018) that can be requested by any researcher through their loan program. These standard sets have been widely used and are particularly useful for inter-laboratory/facility comparisons. The absolute value of the $Fe^{3+}/\sum Fe$ ratios of the NMNH basaltic glass standards (Cottrell et al., 2009, revised by Zhang et al., 2018), and, in fact, all glasses, has been the subject of contention. Two independent revisions of the Cottrell *et al.*, 2009 calibration have been proposed (Zhang *et al.*, 2018; Berry *et al.*, 2018), diverging because of different interpretations of Mössbauer spectra. The Mössbauer-based calibration of Zhang et al., 2018 is consistent with wet-chemical determinations of $Fe^{3+}/\sum Fe$ ratios as a function of fO_2 (Zhang et al., 2018; Cottrell et al., 2020; Borisov et al., 2018), while the Mössbauer-based calibration of Berry et al., 2018 is consistent with the theoretical change in $Fe^{3+}/\sum Fe$ ratio as a function of fO_2, and suggests that wet-chemical

determinations overestimate $Fe^{3+}/\sum Fe$ ratios (Berry et al., 2018, O'Neill et al., 2018). This unresolved controversy concerns the accuracy of Mössbauer- and wet-chemical-based calibrations and does not affect the utility of calibration standards for the precise determination of relative differences in $Fe^{3+}/\sum Fe$ ratio, nor does it impact the relationship between XANES spectra and fO_2 for a given composition. In other words, it may be debated whether a given XANES (or Mössbauer) spectrum of a typical mid-ocean ridge basalt corresponds to $Fe^{3+}/\sum Fe$ =0.09 or 0.15, but both interpretations of the calibration may still imply that the spectrum is most consistent with a basalt equilibrated at or near the quartz-fayalite-magnetite (QFM) buffer.

Other authors have created sets of standards for basalt (e.g. Berry et al., 2003; Wilke et al., 2004; Botcharnikov et al., 2005; Dauphas et al., 2014), andesite, dacite, rhyolite (e.g., Dauphas et al., 2014), alkali-silicate glasses (e.g., Knipping et al., 2015), basanites (e.g., Moussallam et al., 2014), haplotonalites, haplogranites (e.g., Wilke et al., 2006) and felsic glasses (Fiege et al., 2017). While international standards offer useful opportunities for inter-study comparisons, they may not cover the compositional or fO_2 range of interest to your study. In this case, it is best to create your own standards by synthesizing glasses of the desired compositions over a range of fO_2 conditions. The $Fe^{3+}/\sum Fe$ of the synthesized materials must be determined by one or several independent methods before using them as XANES standards.

Many attributes of Fe-XANES spectra contain information about iron's formal valence state and coordination, including the pre-edge, edge, and the extended, or post-edge, regions. We provide an example of how Fe-XANES spectra of basalts evolve with changing $Fe^{3+}/\sum Fe$ ratios in Fig. 5.
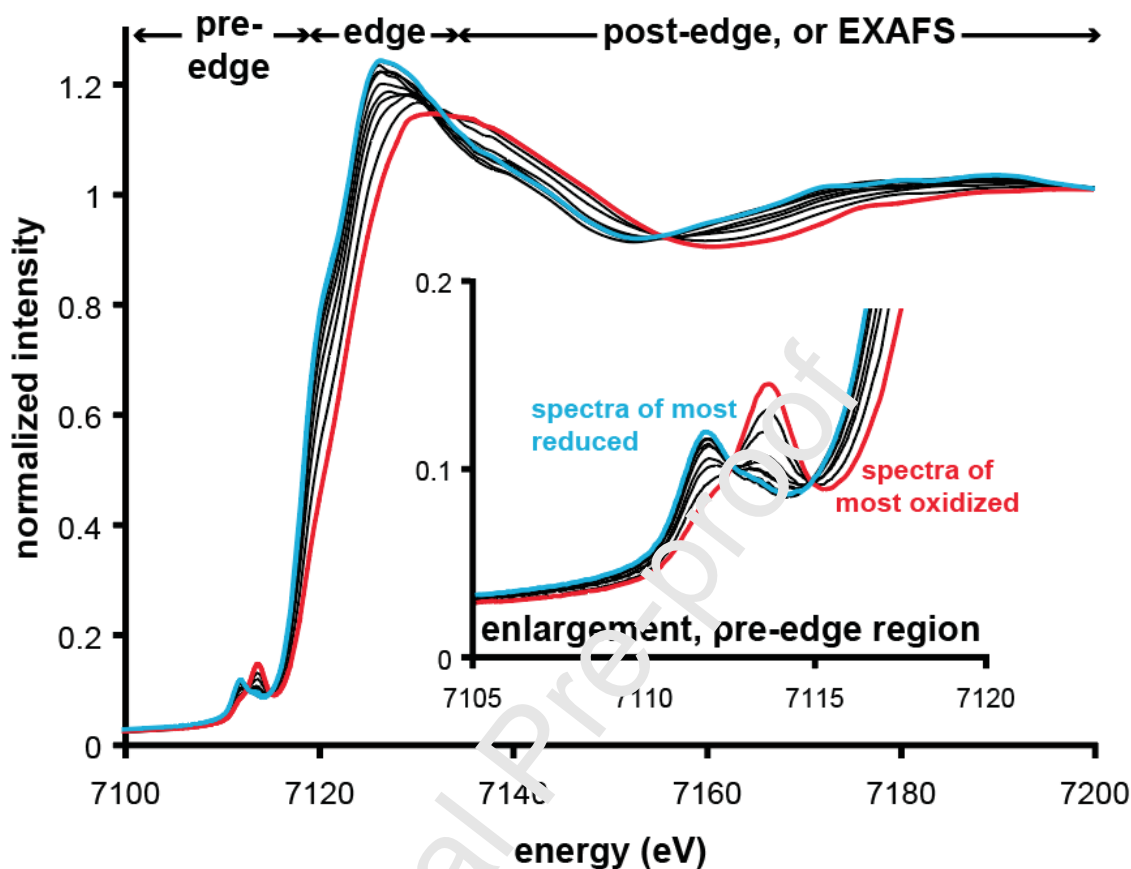
Fig. 5: Edge-step normalized XANES spectra of basaltic standard glasses (Smithsonian catalog number NMNH 117393) equilibrated from 2.5 log units below, to 4.5 log units above, the QFM buffer. Spectra of most oxidized and most reduced glasses are highlighted in red and blue, respectively (modified from Cottrell et al., 2009, with permission).

The precision with which $Fe^{3+}/\sum Fe$ ratios or coordination can be inferred will depend on the quality of the standard calibration and the quality of the spectra acquired. The latter depends on the X-ray flux, the optics and focusing achievable at the beamline, energy step resolution and dwell times, and many sample-specific factors, such as the concentration of Fe, the susceptibility of the sample to radiation damage, and the size of the analyzable area/volume. Precision must be established at each analytical session through standard means, such as replicate analyses, and propagated through the uncertainty inherent in the calibration.

The preparation of naturally glassy melt inclusions hosted in iron-bearing minerals such as olivine or pyroxene will need to be doubly intersected polished wafers with both sides of the melt inclusion exposed (Fig. 2 and Fig. 6), leaving a clear path through the glass. It is essential that the X-rays only interact with the target glass to avoid contributions from Fe in the mineral host or mounting media. To avoid contamination, practitioners must keep in mind that the X-ray beam is at a 45-degree angle to the sample (if spectra are acquired in fluorescence mode) and that the X-ray beam penetrates the sample and interacts with Fe at depth. The diameter of the melt inclusion must always be significantly greater than the X-ray spot size and proportional to the wafer/glass thickness (Fig. 6). Measured spectra should also be screened for features that indicate the presence of Fe-bearing microlite or nanolite crystals, which may invalidate the application of calibrations that are established for pure glasses (Lerner et al, submitted). Fe-free glass slides are useful for mounting wafered samples to avoid potential spectral contamination.
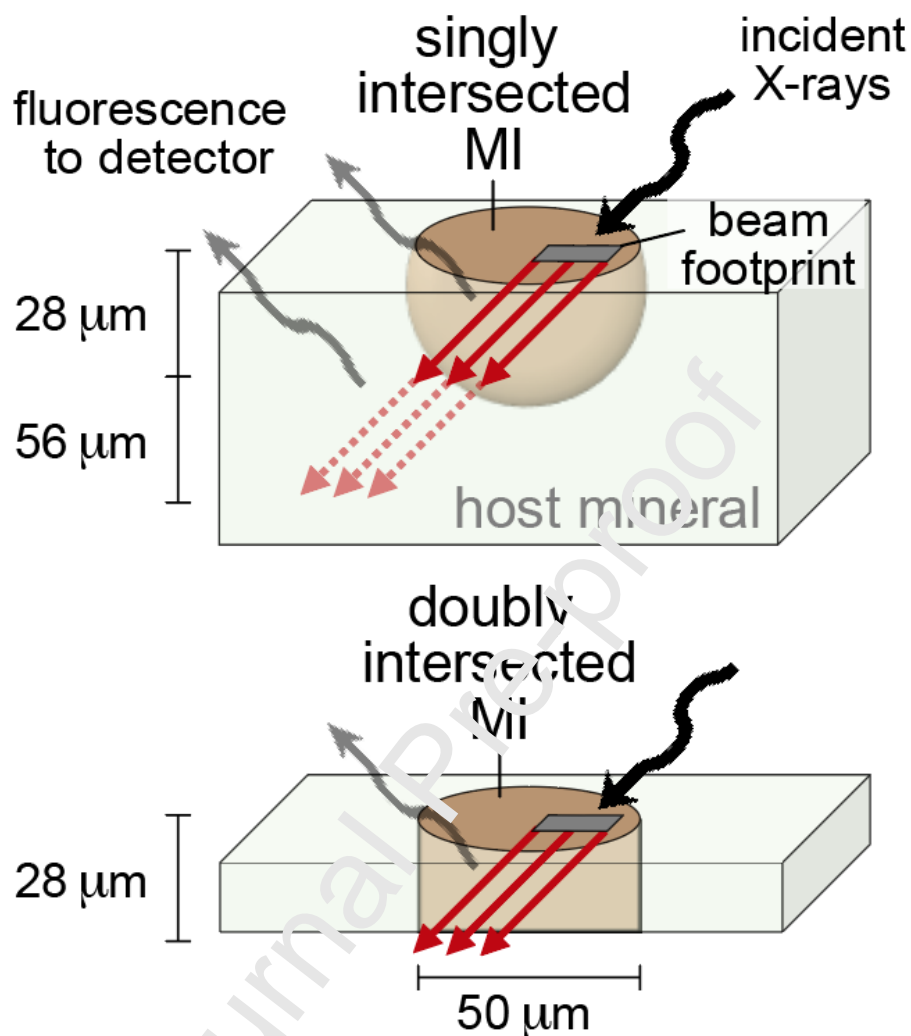
Fig. 6: Schematic illustration of Fe K-edge XANES analysis of an olivine-hosted melt inclusion, highlighting the geometrical considerations and X-ray penetration depths for a typical basalt. Solid and dashed red lines indicate the depth at which 37% and 86%, respectively, of the X-rays at 7118eV are absorbed ($1/e$ and $1/e^2$, respectively). Figure modified from Lerner et al., submitted, and provided courtesy of Allan Lerner and Michelle Muth.

Spectral contamination from Fe in other phases must be rigorously monitored and avoided. 2D mapping and line transects across the inclusion-host interfaces above the Fe-edge provide one mechanism to X-ray image the glass, enabling selection of a contamination-free area. Following acquisition, each spectrum must be carefully assessed for evidence of contamination, which often manifests as increased structure near

the main absorption edge, due to increased short-range ordering in minerals, relative to glass (e.g. Fig. S2 in Kelley and Cottrell, 2009). Principal component regression over the edge and post-edge energy range (7125–7300 eV) can also be used to identify contaminated spectra, since one of the principal components will be correlated with the extent of host contamination (Hartley et al., 2017).

To extract the formal valance of Fe from XANES spectra, several processing methods have been proposed. All techniques benefit from the collection of high-quality spectra on standards and unknowns. Because XANES is an empirical "fingerprinting" technique, the essential requirement is that standards and unknowns be treated identically, and the calibration technique must either be insensitive to composition, or the calibration glasses must have well-matched matrices to the unknowns. Beyond that requirement, many options for spectral fitting and analysis are available. The three most common are detailed here:

i. Ratio of intensities, or peak height ratio method
The relative intensity of the two pre-edge peaks is used to calibrate for $Fe^{3+}/\sum Fe$ ratio (e.g. Berry et al., 2003; Cottrell et al., 2009; Wilke et al., 2001; Wilke et al., 2005; Zhang et al., 2016). Advantages of this method include that the peak height ratio remains sensitive to changes in $Fe^{3+}/\sum Fe$ ratio even as $Fe^{3+}/\sum Fe$ ratios exceeds 0.5, and that the ratio is less sensitive to glass composition (Zhang et al., 2016).
ii. The centroid method
The pre-edge regions of edge-step normalized spectra are fit with combinations of mathematical functions, which are then used to calculate the centroid, or area-weighted average energy, of the background-subtracted pre-edge peaks. The centroid varies non-linearly with $Fe^{3+}/\sum Fe$ ratio and the centroid loses sensitivity as $Fe^{3+}/\sum Fe$ ratios increase beyond ~ 0.6. This method has the advantages of being highly precise for the determination of formal valence (e.g., Cottrell et al., 2009; Cottrell and Kelley, 2011, 2013; Moussallam et al., 2014, 2016, 2019a; Fig. 7) and being less sensitive to coordination changes (e.g. Berry et al., 2003; Cottrell et al., 2009; Wilke et al., 2001; Wilke et al., 2005; Zhang et al., 2016). This method has been shown to be composition

dependent (Cottrell et al., 2009; Dauphas et al., 2014; Zhang et al, 2016) and so care with the calibration must be taken.
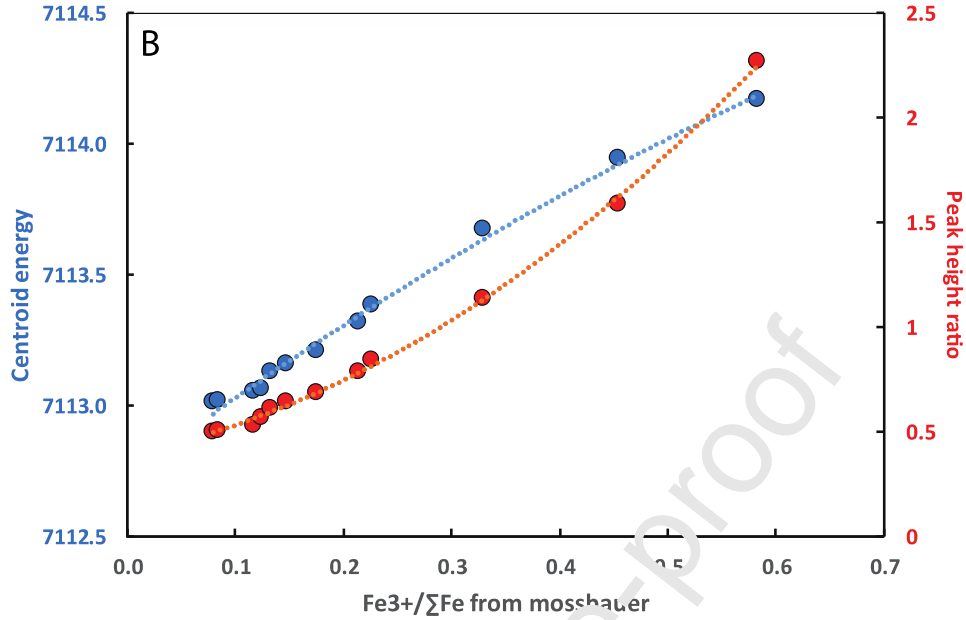

Fig. 7: Calibration curve for the centroid position (blue) and peak height ratio (red) determined by XANES compared with the $Fe^{3+}/\sum Fe$ ratios of the Smithsonian basaltic standard glasses determined by Mössbauer spectroscopy (data from Moussallam et al., 2019a).

iii. The principal component regression method

Principal component regression (PCR) identifies spectral features corresponding to the maximum variance in the dataset through conventional principal component analysis (PCA). The principal components are linearly correlated with $Fe^{3+}/\sum Fe$, meaning that reference spectra can be used to generate a linear mixing model to determine $Fe3+/\sum Fe$ in unknowns (e.g., Farges *et al.*, 2004; Shorttle *et al.*, 2015; Dyar et al., 2016; Hartley *et al.*, 2017). An advantage of the PCR method over the critical pre-edge region of 7105–7119 eV is that it uses all redox-sensitive features of the spectra, including the absolute position of the main absorption edge, and hence is theoretically most sensitive to small differences in $Fe^{3+}/\sum Fe$ between spectra. The disadvantage of PCA is that it may ascribe spectral changes to formal valence that might instead be due to coordination changes (for example, due to composition).

34

Calibrations for andesites, basalts, and hydrous basaltic glasses have proven to be statistically indistinguishable (Dauphas et al., 2014, Zhang et al., 2016, 2018; Cottrell et al 2018) provided there is no beam damage (Cottrell et al., 2018). Beam damage refers to radiation-induced changes in the sample by interaction with a monochromatic X-ray beam, such as oxidation/reduction of a cation and/or element migration. The extent of X-ray-induced photo-oxidation or reduction of Fe in silicate glasses is dependent on the glass composition, water content, and the photon flux density (Goncalves Ferreira et al., 2013; Cottrell *et al.*, 2018). Flux density can be diminished via attenuation of the beam, but is also efficiently achieved via defocusing the beam to larger spot size. The former has the advantage of maintaining high spatial resolution, while the latter has the advantage of maintaining, or increasing, the signal/noise ratio. While it is ideal to minimize beam damage, it may also be possible to account for beam damage using time-dependent corrections (Lerner et al., submitted). Fig. 8 shows the effect of using different beam attenuation conditions on the extent of induced beam damage during XANES analyzes of a water-rich basaltic glass. Inappropriate analytical conditions may result in extensive beam damage of unknowns, and hence unreliable results.
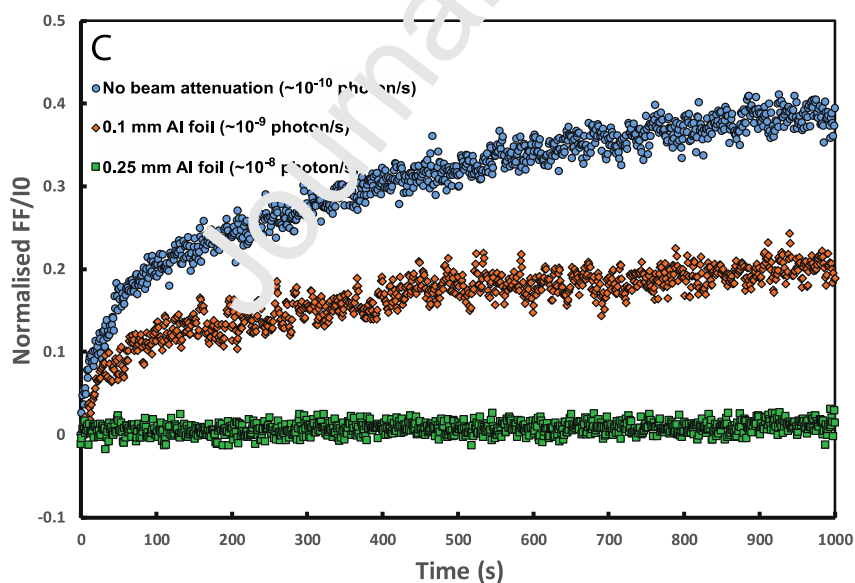

Fig. 8: Three independent time-series analyses of a hydrated (5.2 wt.% H_2O) basalt under three different beam attenuation conditions. Plotted is normalized fluoresced intensity (FF) over the incident flux (I0), with the monochromator set to the position of the higher energy pre-edge multiplet, integrated over 1 s intervals at a spot size of 2.5×1.2 μm

35

(modified from Moussallam et al., 2019a). At high photon flux density (blue circles), the intensity of the high energy pre-edge peak increases with time, whereas this is not the case at low flux density, once the beam has been attenuated, here down to 1% of its original flux (using a 0.25 mm Al foil).

Recommended practice (XANES):

Type of data produced:

Valence state of element of interest (examples detailed here are for Fe K-edge studies for the determination of $Fe^{3+}/\sum Fe$)

Sample requirements:

Solid (examples detailed here are for glasses). For melt inclusions hosted in iron-bearing minerals, prepare a double polished wafer, leaving a clear path through the glass (Fig. 2 and 6). It is best not to subject your inclusions to any other analytical technique using an X-ray, electron, ion beam or laser prior to XANES analysis. The valence of Fe in the glass can be modified by such techniques especially if the inclusion is water rich. XANES analysis should therefore be one of the first techniques you subject your inclusion to.

Analytical conditions:

Fe K-edge spectra are generally acquired from 7000 to 7350 eV, or higher, with the pre-edge region (7110-7118 eV) acquired at higher energy resolution than the pre- or post-edge regions. Every XANES study should begin with a series of tests to define the analytical conditions under which the samples can be analyzed with acceptable signal/noise and minimum beam damage. Tests should be performed on natural or synthetic glasses that have the same composition and the same (or higher) water content as the unknowns, such as monitoring for time-dependent or flux-density-dependent (i.e. spot size) changes. As a result, specific analytical conditions will vary based on individual studies/samples.

Analytical details:

Standards or reference materials of similar composition should be analyzed during the same analytical session as your unknown to obtain a valid calibration. The accuracy of the XANES measurement is only as good as that of independent method used to determine the $Fe^{3+}/\sum Fe$ of the standards. The precision with which $Fe^{3+}/\sum Fe$ ratios or coordination can be inferred will depend on the quality of the standard calibration and the quality of the spectra acquired and must be determined at each analytical session. Contamination from Fe-bearing materials during XANES analysis of the melt inclusion must be avoided through the judicious choice of analysis points (via mapping or line profiles) and all scans should be screened for evidence of contamination.

Reporting requirements:

-Report the synchrotron, beamline, beam dimensions, monochromator, mode, detector, energy step sizes, dwell time, incident photon flux, photon density at the sample surface and geometry of the setup.
-Report results of your beam damage tests.
-Report calibration standards used and an energy reference position for a widely-available standard, such as Fe-foil or other freely available reference material.
-Report the precision with which the spectral parameters used to quantify Fe oxidation state can be fit/extracted and propagate this precision through the calibration curve to obtain overall precision. Check precision via replicate analysis of a standard throughout the analytical session.
-We encourage publication of raw and edge step-normalized spectra from all unknowns and standards as supplementary information.
-Report the full composition, including volatile contents, of your unknowns and standards.

2.4. Secondary ion mass spectrometry

Secondary Ion Mass Spectrometry (SIMS) is a microanalytical technique that utilizes a finely focussed beam of primary ions (O^- or Cs^+ are most common for geochemical applications) to sputter secondary ions from the surface of a solid substance. These secondary ions are subsequently analyzed using a specially adapted mass spectrometer. As such, SIMS provides an extremely versatile tool for analysis of glassy melt inclusions that have experienced little or no PEC.

In addition to quantitative trace element (e.g., REE and other incompatible elements; e.g. Sobolev and Shimizu, 1993; Sobolev, 1996) and volatile (e.g., H_2O, CO_2, S, Cl, F, Br; Sisson and Layne, 1993; Hauri et al 2002a, Hauri 2002b ; Bracco Gartner 2019; Cadoux et al., 2017) analysis, a specific strength of SIMS is sub-per mil precision and reproducibility for a wide variety of stable isotope ratio determinations (δD, $\delta^7 Li$, $\delta^{11} B$, $\delta^{34} S$, $\delta^{37} Cl$; Hauri, 2002b; Layne 2006; Manzini et al., 2017a) and radiogenic isotopes ($^{204} Pb/^{206} Pb/^{207} Pb/^{208} Pb$, Layne and Shimizu 1998a, 1998b; Kobayashi et al 2004).

In general, a lateral spatial resolution of 10 μm (with sputtered pit depths of less than a few μm) may be achieved for individual analyses (total sample size < ~10 ng). *In situ* SIMS microanalysis is thus compatible with the size range of many melt inclusion populations. Samples commonly require only simple preparation of a flat polished surface that exposes the melt inclusions, thus preserving information on both host minerals and textural context - although samples and mounting media must be compatible with the ultra-high vacuum of the SIMS sample chamber. Therefore, many SIMS

37

facilities now encourage sample preparation in indium mounts for certain applications. A thin conductive layer, usually ultra-pure Au, is applied to the sample surface to mitigate charging during analysis. Balanced electron flooding may also be required during analysis if using Cs^+ primary ion beams.

For determination of volatiles (F, Cl, S and especially H_2O and CO_2; Hauri et al., 2002a,b; Koga et al., 2003), or for light stable isotopes of trace element analytes (e.g., $\delta^{11}B$, Chaussidon et al., 1997; Straub and Layne 2002), an intrinsic advantage of SIMS is the ability to combine pre-sputtering of the sample surface with an appropriately restricted effective field of view (Field Aperture) for ions entering the mass spectrometer. This approach can be used to reduce extraneous signal from surface contamination to an insubstantial level – in fact, often well below the comparable "blank" levels that limit some other mass spectrometric approaches. For CO_2 measurements, the melt inclusion will need to be exposed avoiding diamond paste solutions or any carbon-bearing polishing disks. Corundum polishing mats will be preferred and care will be taken to analyze a glassy area far from any cracks, hole or partially-open bubble since all these surface defects are source of contamination.

SIMS instruments are designed to resolve the complex mass spectra of secondary ions produced by the ion beam sputtering of solid materials, using energy filtering and/or mass resolution approaches (Layne, 2006). Degree of ionization to simple (generally monoatomic) secondary ions during sputtering varies by element, primary beam and major element matrix. As a consequence, quantification requires comparison to reference materials of similar bulk composition to the sample, and the use of appropriate and well characterized reference materials is an important consideration in all forms of SIMS microanalysis. Matrix matching reference materials are required to calibrate for the combined instrumental mass fractionation (IMF) effects related to mass dependence in production of analyte secondary ions by sample sputtering, and to mass dependent effects in the ion detectors.

Many analyses are readily accomplished using smaller format (e.g., Cameca f-series) SIMS instruments (for example, $\delta^{11}B$; Chaussidon et al 1997). However, larger format (e.g., Cameca 1270/1280/1300HR) instruments have significant advantages for some

analyses, especially those where a trace element analyte is used for isotope ratio analysis; for example, δ^7Li (Bouvier et al., 2008), δ^{11}B (Rose et al., 2001; Straub and Layne 2002) or δ^{37}Cl (Layne et al, 2009; Bouvier et al., 2019). The multi-collection arrays of larger format instruments can also become invaluable for the determination of δ^{37}Cl (Manzini et al 2017a), δ^{18}O (e.g., Hartley et al., 2012; Manzini et al., 2019) or δ^{34}S (Chaussidon et al., 1989; Cabral et al., 2013) and both precision and accuracy for Pb isotope analysis can be improved (e.g supplementary material in Rose-Koga et al., 2012).

Due to the gradual removal of material by sputtering, SIMS also inherently accumulates a time-resolved depth profile of the sample, allowing the selective elimination of signals from defects or micro inclusions. Image acquisition of elements via large geometry SIMS is also possible by rastering a large area (up to 500 μm squared), and accumulation of image layers allows 3D imaging of melt inclusions (Florentin et al., 2018).

Imaging and diffusion profiles between melt inclusions and their host are more precise when using a Cameca NanoSIMS instrument. Indeed, due to a different geometry and ion optical design, NanoSIMS can achieve superior lateral spatial resolution, typically 100–200 nm, compared to typically 10 μm, possibly down to 3 microns (Decraene et al 2021), for other SIMS instruments. NanoSIMS has been used, for example, to map the volatile distribution in and around melt inclusions (Hauri et al., 2011; Le Voyer et al., 2014). Similarly, to estimate residence time or ascent rate, exceptionally fine scale diffusion profiles can be obtained for volatile elements (e.g. Lloyd et al., 2014; Newcombe et al., 2014; Moussallam et al., 2019b) or trace elements (e.g. Manzini et al., 2017b).

Trace elements analysis could be done by SIMS and laser ablation mass spectrometer (LA-ICP-MS). Kent (2008) detailed the advantages and disadvantages of both techniques for such measurements. To summarize, both techniques could achieve similar precision. Detection limit is usually better with the SIMS, however the new generation of LA-ICP-MS (e.g., coupled with sector field spectrometer Element XR MS) can achieve low detection limit for trace elements, allowing measurements of trace elements in olivine for example (e.g., Bussweiler et al., 2019). Acquisition time is faster for LA-ICP-MS measurements than for SIMS. Cost-wise, LA-ICP-MS is more often less expensive and

easier to access than SIMS. The main disadvantage of LA-ICP-MS is a deeper spot, also sometime larger than for the SIMS (5-20 microns diameter for SIMS vs. 10-50 microns diameter for LA-ICP-MS). If LA-ICP-MS is the method chosen for trace element analysis, then all other analysis required for the project must be done before.

There are a number of recent or on-going improvements in SIMS analysis that may contribute to the expansion of frontiers of melt inclusion research. Progressive improvement in SIMS capability for lateral imaging of trace elements has been left generally unexplored for applications such as assessing diffusion profiles between melt inclusions and host minerals. New finer spatial resolution and denser primary sources (e.g., Hyperion II™ RF O⁻ source) have the potential for applications to ultra-small inclusions, improved measurements of diffusion profiles by step traverse or imaging, and the informative assessment of microlites and other inhomogeneities within individual melt inclusions, as well as better precision on stable isotopes of trace elements (δ^7Li, δ^{11}B). Also, development of more sensitive detectors (for example, Faraday cup associated with 10^{12} Ω resistor) will allow a better precision on some stable isotopic systems (e.g., δ^{37}Cl, δ^{34}S) over a large range of composition of the targeted analyte.

Recommended practice:

Type of data produced:
Mostly concentrations of volatile elements and isotope compositions. Possibly trace elements compositions.

Sample requirements:
Solid (glass or minerals) with a flat polished surface. Samples should be pushed in indium mount. High vacuum pre-preparation is especially important for the analysis of CO_2 or δD (Hauri et al 2002a), and preparation in an indium (instead of epoxy) mount is encouraged (mandatory in certain SIMS hosting institutions). Samples should be kept at least overnight in the airlock of the SIMS or several days in an oven at 70ºC prior to measurements.

Analytical conditions:
1) Provision of well characterized matrix-specific reference materials for the calibration of elemental concentrations and instrumental mass fractionation (IMF). A piece of the

appropriate standard material(s) (acting as secondary standard) should be placed in each sample mount, in order to monitor possible instrumental drift or possible mount conductivity trouble. 2) Elimination of sample surface contamination and other exotic contributions through pre-sputtering and other means, including pre-preparation in high vacuum where necessary. 3) Calibration of accuracy and sensitivity (or relative sensitivity) of ion detectors (whether single or multiple array) over an adequate dynamic range. This last consideration is especially important for stable isotope determinations.

Reporting requirements:
-Report the instrument manufacturer, model used for analyses.
-Report the primary beam used (O^-, O^{2-}, Cs^+…), the use of electron gun or not and the intensity of the primary beam. The values of the contrast aperture and field aperture and the mass resolving power (MRP) should also be given and varies between concentration measurements and isotope measurements.
-Report the counting time on each mass of elements, the pre-sputtering time and the deadtime applied. For comparison with other studies, the useful yield for the element of interest could be reported.
-Report calibration standards used, detection limits, precisions and accuracy.

2.5. Electron Microprobe

Electron probe microanalysis (EPMA) is used to measure major and some volatile elements (S, Cl, F) *in situ* in melt inclusions and their hosts. Since this analytical technique requires carbon coating the sample to make the surface conductive, it is best when possible to carbon coat the sample and conduct EPMA analyses after CO_2 has been analyzed by SIMS. Beam damage can be significant during EPMA of both mafic and rhyolitic compositions, especially for hydrous glasses, resulting in mobile element migration (Na, K, and H; e.g. Morgan and London 1996; Humphreys et al., 2006), elevated concentrations of immobile elements (Si, Al; e.g. Morgan and London 1996), and redox changes to Fe and S (e.g. Fialin et al., 2001; 2004; Fialin and Wagner, 2012). Therefore, the analytical conditions and routine must be carefully chosen. For instance, time-dependent intensity corrections can be used to correct for changes in element concentrations during analysis by extrapolation back to time zero (Nielsen & Sigurdsson, 1981). Also, using mean atomic number (MAN) background (uses the measured relationship between background counts and MAN, rather than measured off-peak

41

backgrounds, to calculate the background; Donovan & Tingle 1996) reduces analysis time and beam damage.

Using lower intensities, 2 to 4 nA, avoids migration but then count rates are low (e.g. Morgan and London, 1996). An alternative is to use two different beam conditions at a single location by analyzing Na, K, Si and Al at a first condition of 8–10 nA, and then the rest of the major elements and volatiles at a higher current of 50 nA (e.g., Ruscitto et al., 2011). If limited in time and/or only allowed one beam condition, an 8 nA beam current, an accelerating voltage of 15 kV and a 20 μm defocused beam is recommended for glass analysis as repeated analysis (more than 1500 measurements) of the anhydrous basaltic standard VG-A99 show no significant sodium loss (Oladottir *et al.* 2011). Other studies have shown that for hydrous basaltic MI from arc samples, a substantial Na migration happens even at 10 nA (e.g. Vigouroux et al., 2008; Ruscitto et al., 2011). In this case, either time-dependent intensity corrections must be used, or a lower current of 4 nA is required to avoid sodium migration, and the latter results in a signal that is twice as low and longer counting times are required (on the order of 4 times longer). A beam size beyond ~20 μm will result in the wavelength dispersive spectrometers, which measure the X-ray intensities, going out of focus. Typical analytical uncertainties (1σ) in these conditions, obtained from replicate measurements of the basaltic glass standard VG-A99 (Jarosewich et al. 1979) are typically less than 3% for FeO and K_2O, 5% for Na_2O and P_2O_5, 30% for MnO and 2% for the other oxides. A test for the effect of beam defocusing on the analytical reproducibility consists of comparing analyses done with a 10 and 20 μm beam size in a single melt inclusion.

Chlorine, sulfur and fluorine analyses are best performed at higher currents, 40–80 nA, to ensure higher count rates, and with a 10–20 μm defocused beam and given the low concentrations of these volatiles, they need to be treated as trace elements, with longer counting times and/or higher sample current. Details information about analytical procedure of the volatile element measurements are given elsewhere (e.g., Rose-Koga et al., 2017 and 2020). Depending on the counting times of Cl, S and F, detection limits can reach ~50, 50, and 150 ppm, respectively. Longer counting time with high sample current can lead to lower than 10ppm detection limits for Cl for example (Sobolev et al., 2011). The total analytical error for S, Cl, and F including precision and accuracy of

measurements, is typically of 20% (relative uncertainty) for S, and 30% for Cl and F over the range of concentrations found in inclusions. There is excellent agreement between EPMA and SIMS measurements for F concentrations above 150 ppm and on 10 widely available referenced standards (Rose-Koga et al., 2020; Fig. 9).
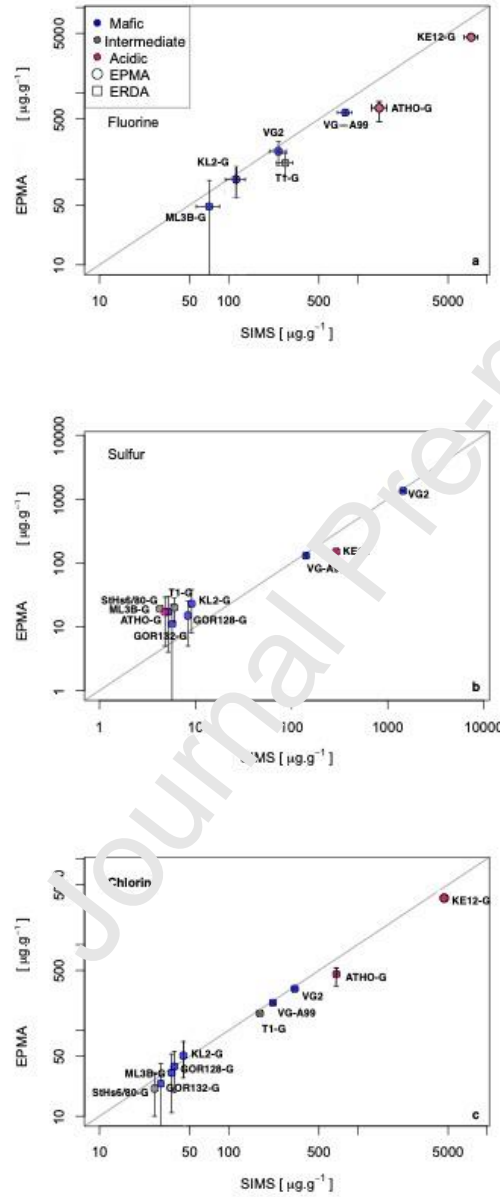

Fig. 9: log-log plot of concentrations of F (**a**), S (**b**), and Cl (**c**) measured by SIMS vs. that measured by EPMA (circles). Standards are categorized according to their SiO_2 contents into mafic, intermediate, and acidic. The solid line is a one-to-one slope indicating the coherence of the fit, and the dashed lines are 20% slope variation to help

reading the figure. The square symbols are ERDA measurements (modified from Rose-Koga et al., 2020). The high SiO_2 standards do not fall on the same slope as standards with mafic and intermediate compositions (Rose-Koga et al., 2020).

 Precision and accuracy can be improved for EPMA at low concentrations (e.g., in MORB or ultra-depleted inclusions) by using two or more spectrometers simultaneously for the same element. Large area analyzing crystals on some microprobes also provide lower detection limits and better precision. While analyzing elements with low concentrations (<100 ppm), it is also useful to run a "blank" by analyzing a material that has ≈0 ppm of the element(s) of interest to ensure that sample surfaces are not contaminated and that backgrounds are chosen correctly. A clear spot in the host crystal is readily available and is a good choice for many incompatible elements. SIMS analytical precision as well as detection limits on Cl, S, F are usually smaller (< 5% relative) and lower (< 10 ppm typically), but using EPMA has the advantage of being more accessible and less expensive. Sulfur can occur in multiple oxidation states in a melt (Carroll and Rutherford, 1988; Jugo et al., 2010), and therefore the choice of standards and S K_α peak position measurement need to be considered for each sample suite because the peak position of S K_α shifts with changes in oxidation state (e.g., Wallace & Carmichael, 1994). This wavelength shift makes it possible to use EPMA to measure the S oxidation state of melt inclusions. For such measurements, the spatial resolution is ~50 μm^2 with an error of ±0.05 on S^{6+}/S_{total} (e.g., Rowe et al., 2007). It has been shown that changes in the oxidation state of multivalent elements such as Fe and S may occur under the electron beam. Moving the beam position incrementally at a rate of 1μm/min seems to avoid the apparent increase in $\lambda(SK\alpha)$ (Wallace & Carmichael, 1994; Rowe et al., 2007).

Although not a direct measurement "volatiles by difference" (VBD), an estimate of the H_2O+CO_2 content of the glass, can be calculated from the difference between 100 wt% and the analytical total (e.g., Devine et al., 1995, Humphreys et al., 2006, Hughes et al., 2019). For very high CO_2, the CO_2 could be as much as 30% of the VBD value (e.g. Ross Island basanites, Rasmussen et al. 2017), in other cases authors have often assumed that the CO_2 content was almost always so low in comparison to H_2O content, that VBD was an effective estimate of H_2O content

Recommended practice:

Type of data produced:

Concentrations of major and minor elements (including volatile elements S, Cl, F)

Sample requirements:

Solid (glass or minerals) with a flat polished surface. The area to be analyzed must be exposed on the sample surface. Mount samples in indium (rather than epoxy) if you plan to measure more volatile element by SIMS, otherwise epoxy is fine. Perform SIMS analysis before EPMA to avoid carbon contamination. Best results obtained if MI is greater than about 10 microns in diameter to avoid including host phase in the analysis. MI should not contain multiple solid phases (but may contain a vapor bubble).

Analytical conditions:

Analytical conditions will vary depending on what is being analyzed (glass versus mineral), mineral type and element. Use analytical conditions that are appropriate and analyze elements in an order that minimizes modifications, such as diffusion of Na, during exposure to the electron beam. Calibrate using a standard that closely matches the unknown to be analyzed is not mandatory because modern matrix correction methods are so good that this is less of a concern than it used to be. Instead we recommend that one analyze a standard like VG-2 glass as an unknown periodically during a run to confirm accuracy and detect and correct for drift.

Analytical details:

Analyze multiple spots if the MI is large enough (great than about 25 microns).

Measure the host composition in 2-3 different locations close (< 20 microns) to the melt inclusion. This may not be required for MI in quartz, depending on the question/problem being addressed

If doing transects to determine zoning of the host phase, collect two transects radial to the melt inclusion (90° from one another).

Reporting requirements:

Recently thorough guidelines for reporting EPMA results were recently published (Llovet et al., 2021). The recommendations are for applications in material science and engineering and most of them apply to Earth science as well. In the following we suggest a more streamlined version of the requirements.

 -Report the instrument manufacturer and model of the electron microprobe used for analyses.

-Report calibration standards used and analytical conditions for each element analyzed (beam current, accelerating voltage, beam diameter, counting time, analytical uncertainties).

-Report the size and shape of each MI analyzed and include a photomicrograph of each MI in supplementary data. On the photomicrograph place a mark to indicate the location of each analysis within the MI and the surrounding host phase. Use the same identifier on the photo and in the data tables to allow easy comparison (i.e., a given analysis might have an identifier such as: 08102019-A-IV-1 where:

08102019 is the sample number (here it is identified based on the date it was collected – August 10, 2019.

A is the phenocryst or crystal in sample "08102019"

IV is the label for the MI in phenocryst "A" in sample "08102019"

1 is the first analysis of MI "IV" in phenocryst "A" in sample "08102019"

2.6. LA-ICP-MS

Laser Ablation-Inductively Coupled Plasma-Mass Spectrometry (LA-ICP-MS) is perhaps the most easily accessible and frequently used method for micro-analysis of minor and trace elements in melt inclusions and their mineral hosts. This method involves pulsing a UV wavelength laser (213 Nd-YAG or 193 nm ArF are most common) at a set frequency to ablate a small spot (tens to hundreds of μm) in a sample. The ablated material is swept away in a carrier gas (commonly He, Ar, or a mixture of the two) and transported to an inductively coupled plasma for ionization, and analysis by mass spectrometry. We note that if SIMS analysis were performed on the MI using the cesium (Cs) source, then Cs will be implanted in the sample (Mourey et al., 2017) and laser data on Cs trace element measurements should be discarded. Advantages of this method over others (e.g., SIMS) include relatively low cost, rapid sample throughput, less matrix sensitivity, and a large suite of analyzable elements. Another major advantage is that LA-ICP-MS allows simultaneous analysis of elements over a 9-10 order of magnitude concentration range, thus permitting analysis of major (wt. %), minor and trace (ppb to ppm) elements at the same time. Yet, this method of analysis is particularly destructive to the sample, and so should be the final analytical method used in any planned sequence of analyses on a melt inclusion.

A background of the ICP-MS signals with the laser off is usually collected at the beginning of each analysis (~30-40 s), and an average of this background is then subtracted from the average count intensity on the sample for each element. Background-subtracted intensities are then typically normalized to the signal of an internal standard

element whose concentration may either be inferred from stoichiometry or independently determined using another analytical method (e.g., for glasses, ^{47}Ti, ^{43}Ca, and ^{29}Si are commonly used; Kelley et al., 2003; Lytle et al., 2012; Jenner & O'Neill, 2012). The technique is calibrated by analysis of a suite of standard glasses of known composition within the same analytical session as the unknowns. The effect of variable concentrations of the internal standard element from one sample or standard to the next is factored out of the normalized signal intensity through multiplying by its concentration. These modified intensities may then be referenced against known element concentrations in a suite of standards to build a working calibration curve that allows quantification of element concentrations in unknowns. For glasses many useful reference standards are now available (e.g., NIST, USGS, MPI-DING). Calibration methods vary among laboratories (e.g., a single-point calibration [Jenner & O'Neill, 2012] vs. a curve built from multiple reference glasses [Lloyd et al., 2013; Kelley et al., 2003]), but for inter-laboratory bias assessment, a recommended practice should be to report the analysis of at least one reference standard run as an unknown. Some commercial software packages (e.g., GLITTER, IOLITE, Lametrace) and free software (AMS; Mutchler et al., 2008) are available to assist with data management and calculations. Most commercial laser systems allow users to adjust the spot size, either using a set of fixed-diameter round apertures or a rectangular spot whose dimensions may be controlled dynamically. In general, the larger the ablated area, the higher the signal intensity, so for melt inclusions, one larger spot will generate data with lower standard deviation for low-abundance elements than two smaller spots (e.g. Kent and Ungerer, 2005; Kent, 2008).

Because of the aggressive rate of sample consumption via laser ablation, sample thickness limits the duration of useable data. For thin samples, such as wafers prepared for FTIR or XANES, ablation time may be extended by slowing the repetition rate of the laser (e.g., from 10 Hz to 5 Hz; Kelley & Cottrell, 2012) to avoid growing through the wafer. Awareness of heterogeneities with depth in the sample is also important for LA-ICP-MS analysis, and spots should be placed to avoid vapor bubbles, co-included phases, and the host crystal if at all possible.

The limit in size for the smallest melt inclusions analyzed by LA-ICP-MS for trace elements, are typically in the 30-50 μm range (possibly down to 10 μm; e.g., Rottier et

al., 2019; Chang and Audétat, 2019, Zhang et al., 2018) and reported precisions and accuracy in this case are better than 10-15% (at the 2σ limit), with detection limits sufficient for measurements of most depleted basaltic compositions similar for example to the composition of BIR-1G standard (i.e. in the ng/g levels; e.g., Kent and Ungerer 2005; Bussweiler et al., 2019).

In some cases, especially with partially to completely crystallized melt inclusions, it is necessary to analyze melt inclusions that are unexposed to avoid preferentially removing some portion of the heterogeneous melt inclusion contents during polishing to expose the melt inclusion at the mineral surface (Severs et al., 2007). In this case, the melt inclusion plus some amount of host phase that is above, peripheral to, and below the melt inclusion will be sampled. Then, the host contribution can be mathematically subtracted if the concentration of one element in the MI is known, and the composition of the host is known (see for example Halter et al., 2002 for the different data treatment methods). For this reason, at least one clean LA-ICP-MS analysis of the host mineral should accompany any melt inclusion analysis, in the event that it is necessary to reconstruct the melt composition by subtracting the contribution from the host.

Recommended practice:

Type of data produced:
Concentrations of major, minor and trace elements.

Sample requirements:
Solid (glass or minerals) with a flat polished surface; specific mounting media are not proscribed because these don't affect the performance of the laser, and most laser systems will accept a variety of common mounts including 1" round mounts typical for EPMA or SIMS analysis, and standard petrographic thin sections. Best results obtained if melt inclusion is greater than about 50 microns in diameter to ensure sufficient signal intensity and to avoid including host phase in the analysis. In the best case, melt inclusion should not contain multiple solid phases (but may contain a vapor bubble), although crystallized inclusions can be analyzed with meaningful results if the entire volume of the inclusion is ablated in bulk during analysis. The area to be analyzed may either be exposed on the sample surface or be unexposed below it, within a volume that the laser will ablate through time.

Analytical conditions:

Analytical conditions will vary depending on what is being analyzed (glass versus mineral), mineral type and element. Spot size is one of the most commonly adjusted instrument settings during LA-ICP-MS analysis, and we recommend for smaller melt inclusions (for example <50μm) to analyze a single, large spot instead of 2-3 smaller spots because the larger spot will produce greater signal intensity and enable better determination of the lowest-abundance elements. For thin samples (e.g., those that have been wafered for FTIR or XANES analysis), it can be advantageous to decrease the laser repeat rate (e.g., from 10 Hz to 5 Hz). Although this decreases the signal intensity, it increases the duration of ablation within the sample and ensures a quantifiable plateau in the spectrum (~20 seconds is a fair rule of thumb). Calibrate using standards that are similar to the unknowns to avoid matrix effects.

Analytical details:
Analyze one biggest spot size or multiple spots if the MI is large enough (> ~100 μm). Measure the host composition close (< 20 microns) to the melt inclusion. This is particularly important if there is accidental contamination of the inclusion spectrum with the host mineral, and also for determining partitioning if desired.
For quantification of LA-ICP-MS data, you must either have previous analysis of an internal standard element by another method (e.g., Ca or Ti by EPMA), or you must be able to assume a stoichiometric concentration of an analyzed element in the host mineral If doing transects to determine zoning of the host phase, collect two transects radial to the melt inclusion (90° from one another). If it is possible to customize the dimensions of the laser (e.g., with a rectangular, rotatable aperture), align the long axis of the rectangle perpendicular to the transect to afford the highest spatial resolution.

Reporting requirements:
-Report the instrument manufacturer and model of the ICP-MS and the manufacturer, model, and wavelength of the laser ablation system.
-Report calibration standards used, reference or report the concentrations used for calibration, and tabulate analytical conditions for each element analyzed (isotope, dwell time, resolution).
-Report the energy output of the laser in units of fluence ($mJ/pulse/\mu m^2$).
-Report any methods used to correct for interferences.
-Report the reproducibility of multiple spots, if applicable, and the analysis of a reference glass analyzed as an unknown.

2.7. Radiogenic isotopes in melt inclusions

49

Analysis of radiogenic isotope ratios in melt inclusions is challenging because their size and elemental concentrations limit the available amount of the element of interest. In the late 90s, a pioneering study by Saal et al (1998) used *in situ* SIMS techniques to determine Pb isotope compositions (including $^{208}Pb/^{206}Pb$ and $^{207}Pb/^{206}Pb$) of melt inclusions from three Polynesian lavas, which were shown to span 50% of the variation in Pb composition in worldwide OIBs. Subsequent studies analyzed melt inclusions from ocean island and subduction-related settings, revealing increased isotope variability compared to the host lava compositions (e.g., Yurimoto et al., 2004; Maclennan, 2008; Rose-Koga et al., 2012; Schiavi et al., 2012; Nikogosian et al., 2016; Rose-Koga et al., 2017) In situ techniques were further developed for Sr isotopes in melt inclusions by LA-multicollector (MC)-ICP-MS (Jackson et al., 2006), and a subsequent paper by Sobolev et al. (2011) reported combined Sr-Pb isotope data obtained by laser ablation. These studies have highlighted the strength of using radiogenic isotopes in individual melt inclusions to study mantle heterogeneity and reveal processes unrecognized in bulk lavas.

In 2009, the first Sr isotope data obtained from combined wet chemistry and TIMS analysis were reported for olivine-hosted melt inclusions from Iceland (Harlou et al., 2009). This approach allows interference-free isotope measurements, and hence yields a significant improvement in precision compared to *in situ* measurements. The authors evaluated the use of micro-milling and showed that entrainment of a small amount of host olivine alongside the inclusion has a negligible effect on the measured isotope composition. It was, however, not until after 2015 that the analytical capabilities were optimized for combined measurement of $^{87}Sr/^{86}Sr$ and $^{143}Nd/^{144}Nd$ ratios in olivine-hosted melt inclusions by TIMS (Koornneef et al., 2015; Reinhard et al., 2018) and, ultimately, combined analyses of Sr, Nd and Pb isotopes including $^{208}Pb/^{204}Pb$ and $^{207}Pb/^{204}Pb$ ratios on individual inclusions (Koornneef et al., 2019). The optimizations included development of miniaturized, ultra-low blank chemical separation procedures combined with analytical techniques that use more sensitive amplifiers in the Faraday detection system of the TIMS (Koornneef et al., 2014). Use of these amplifiers, equipped with 10^{13} Ω resistors in their feedback loop, results in 10-fold increase in precision when analyzing sub-nanogram samples at low ion currents ($<2\times10^{-13}$ A). The techniques allow

50

precise and accurate analyses of Sr-Nd-Pb isotope ratios in individual melt inclusions, provided they contain >1 ng Sr, >30 pg Nd and >200 pg Pb. The capability of MC-ICP-MS for the determination of radiogenic isotopes in melt inclusions (>1 ng Sr, >0.5 ng Nd) has also been demonstrated recently (Genske et al., 2019, Stracke et al., 2019). Current developments include optimizations of the ion-exchange chromatography procedure in order to yield residual matrix fractions that can be analyzed for trace element ratios by conventional ICP-MS methods (Bracco Gartner et al., 2019).

The analytical developments open up new research directions that include intra-oceanic subduction zones, intraplate and mid-ocean ridge settings, and will likely lead to significant advances in our understanding of the processes that create isotopic variability in mantle-derived melts.

Recommended practice for analysis of radiogenic isotopes (TIMS / MC-ICP-MS):

Type of data produced:
Isotope ratios (i.e. radiogenic isotope over stable isotope of an element). Multiple isotope systems (e.g. Sr, Nd, Pb) can be analyzed in a single sample.

Sample requirements:
Melt inclusions should be selected so that the amount of the element of interest is sufficient with respect to potential blank contributions. The inclusion-bearing grain should be prepared so that the inclusion is effectively isolated (i.e. external contributions are negligible); this may necessitate micro-drilling or -milling to remove unwanted parts of the host grain, as well as leaching of the host grain to remove any adhering phases. Wet chemistry techniques (sample digestion) and ion-exchange chromatography are employed to isolate the element(s) of interest. These steps require ultra-pure reagents and minimal handling steps to minimize blank contributions. Representative aliquots of reference materials (closely matching the unknown samples) should be included throughout the procedure. Blanks should be actively monitored and cover the total procedure. If blank corrections are to be made, it is imperative to evaluate individual blank contributions, e.g. from sample preparation, reagents, ion-exchange chromatography, loading on TIMS filament, and their representativeness.

Analytical conditions:
Analyses are typically performed by TIMS or MC-ICP-MS equipped with 10^{11} Ω (for Sr and spiked-Pb fractions) and a mix of 10^{11} and 10^{13} Ω (for Nd and natural-Pb fractions) resistors in the feedback loop of Faraday cup amplifiers. Samples are generally run to exhaustion, ideally at the highest signal intensity for an acceptable number of

51

analytical cycles. Cup configurations should be set so that any potential interfering isotopes are monitored. Standard reference materials (e.g. NIST SRM 987 for Sr) are used to monitor the repeatability and intermediate precision of measurements. For Sr and Nd, isotopic measurements can be corrected internally for instrumental mass fractionation. Double spike inversion for Pb analyses is performed offline, using publicly-available data reduction programs.

Analytical details:

Multiple inclusions in a single grain (e.g. MIA) or compositionally similar inclusions/grains may be pooled to attain enough element of interest and/or the desired analytical precision.

Total procedural blanks can be corrected for using elemental abundances determined through isotope dilution by means of single (Sr and Nd) and double spike techniques (Pb).

Isotope ratios can be corrected for radioactive ingrowth of daughter isotopes over time by conventional age corrections.

Reporting requirements:

-Report the manufacturer and model of the analytical instrument used.

-Report reference materials used and analytical conditions for each isotope system analyzed (cup configuration, average signal intensity for each isotope, number of analytical cycles, propagated uncertainties).

-Report the repeatability and intermediate precision of measurements on standard reference materials. It is advised to avoid usage of terms not defined by ISO (e.g. "external precision").

-Report the elemental contributions for analyses that include inclusion and (part of the) host grain, ideally quantified using reported volume, density and elemental concentrations in both phases.

-If an age correction was applied, report analyzed isotope ratios, calculated initial ratios and employed decay constants.

3. Compositional corrections

A melt inclusion will record the composition of the trapped melt if the melt inclusion remains a chemically and physically isolated system following entrapment. Following entrapment, however, a melt inclusion may experience modifications in response to changing P-T-X-fO$_2$ conditions in the magma, post-entrapment crystallization (PEC) of the host mineral, thermoelastic deformation, plastic deformation and chemical exchange resulting from diffusive re-equilibration with host olivine (and other minerals; e.g.,

52

Watson, 1976; Qin et al., 1992; Tait, 1992; Zhang, 1998; Sobolev and Danyushevsky, 1994; Sobolev and Chaussidon, 1996; Danyushevsky et al., 2000; Gaetani and Watson, 2000; Danyushesky et al., 2002a; Portnyagin et al., 2008; Gaetani et al., 2012; Chen et al., 2013). These modifications must be identified to correct for their effects to reconstruct the original melt inclusion compositions. However, not all processes are reversible and therefore one may not always be able to correct for their effects (e.g. Schiavi et al., 2016). Plastic deformation (e.g. Zhang, 1998) is an example of an irreversible process. Hereafter we discuss the PEC corrections for olivine-hosted melt inclusions.

3.1. For major elements

In the case of olivine-hosted melt inclusions where olivine is the only crystallizing phase, the Fe-Mg contents of the trapped melt can be determined based on the equilibrium distribution coefficient Kd relating the partitioning of Fe and Mg between olivine and melt (Roeder and Emslie, 1970). This correction (first applied to melt inclusion by Anderson, 1974) is described in detail in the following paragraph and affects mainly MgO, FeO_T and SiO_2. All other elements (major, minor, volatile and incompatible elements) are affected to the same degree because they do not enter into the host phase and thus their concentrations are all diluted by the PEC-correction. Between formation at depth and eruption at the surface, an olivine-hosted melt inclusion may undergo crystallization in response to, for example, cooling or diffusive H_2O loss. A layer of olivine crystallizing along the melt inclusion wall will modify the major element composition of the residual melt, particularly affecting Fe and Mg contents. This PEC can be corrected for numerically (e.g., Sobolev and Chaussidon 1996; Sobolev 1996; Danyushevsky et al., 2002b; Danyushevsky and Plechov, 2011). This involves adding small increments of equilibrium olivine back into the measured melt inclusion composition until the Fe-Mg partition coefficient Kd reaches the equilibrium value. The equilibrium value for the Mg-Fe exchange coefficient between olivine and liquid, Kd, is known to depend on T, P, H_2O, and alkali content (e.g. Ford et al., 1983; Sack et al. 1987; Toplis, 2005). As an accurate knowledge of Kd is required for PEC correction, we recommend using a Kd model accounting for as many of these parameters as possible

(e.g. Toplis, 2005, where T and P are inputs to the model and you calculate an "expected Kd"). In addition, because the concentration of Fe^{2+} depends on the oxygen fugacity, the Fe^{3+}/Fe_{tot} ratio is needed for the PEC calculation and has to be assessed (e.g. Kress and Carmichael, 1991).

We acknowledge there are several ways of correcting for this PEC, but the general procedure is to calculate the $Kd=(Fe/Mg)_{olivine}/(Fe/Mg)_{melt}$ of a melt inclusion and recalculate this Kd after each increment of olivine addition. The value of $(Fe/Mg)_{olivine}$ should come from analysis of the olivine directly adjacent to the melt inclusion (but nonetheless, not in the rim of post-entrapment crystallization), so it is important to check for olivine zoning (e.g. Ruscitto et al., 2011) and when possible, to analyze along two orthogonal Fe-Mg profiles radially to the inclusion. The process of olivine addition stops when calculated Kd = "expected Kd". The mean mass of olivine added can therefore be calculated and PEC correction applied. PEC is highly variable, from a few percent to more than 20% (e.g. Rasmussen et al., 2017). The most commonly used software to perform this PEC correction is Petrolog3 (now on version 3; Danyushevsky and Plechov, 2011). It is important to recognize that Petrolog3 is a tool that incorporates many different model choices, meaning that simply stating a PEC correction was carried out using Petrolog3 is too vague. It is advisable to report which models were used for mineral-melt equilibrium, the $Fe^{3+}/\Sigma Fe$ of the melt, FeO_T etc. as implemented in Petrolog3.

A corollary to this recommendation is that the raw data, not normalized to 100 wt. % should be reported in the supplementary material of every melt inclusion study.

Some post-entrapment processes are more challenging to correct. For example, the chemical composition of an olivine-hosted melt inclusion is susceptible to Fe-Mg exchange reaction via Fe-Mg olivine/ melt equilibrium and interdiffusion in olivine (Gaetani and Watson, 2000; Danyushevsky et al. 2000). This process can be assessed by analyzing the host olivine to look for broad compositional gradients adjacent to the melt inclusion (e.g., Fig. 5 of Gaetani and Watson, 2000) or by comparing the FeO_T contents of associated lavas with the FeO_T of the melt inclusions as a function of MgO (e.g., Danyushevsky et al., 2000). Danyshevsky et al. (2000) proposed a correction scheme to deal with this diffusive exchange that can be implemented in Petrolog3.

One alternative to correcting for PEC and diffusive Fe-Mg exchange is to compare melt inclusion compositions using pseudo-ternary projection schemes (O'Hara, 1968; Walker et al., 1979). In this case, inclusion compositions are recalculated into mineral components (typically olivine, plagioclase, clinopyroxene, and quartz). Projecting the recalculated inclusions from the olivine apex eliminates the effects of PEC, and combining Fe and Mg on a molar basis eliminates the influence of Fe-Mg exchange. For melt inclusions hosted in quartz, PEC correction as defined above for olivine hosted melt inclusions, would imply adding SiO_2 but criteria for knowing when to stop is difficult to assess because the quartz host is a single-component system, therefore the composition of the instantaneous host will always match that of the host (e.g. Kress and Ghiorso, 2004). Theoretically, reverse crystallization calculations for plagioclase and clinopyroxene melt inclusions are available using Petrolog3 and PEC correction could be possible. Also, for orthopyroxene and feldspar hosted melt inclusions, both types of melt inclusion can be corrected for PEC (see details in Kress and Ghiorso, 2004).

3.2. For H_2O and CO_2: information from these volatile and bubble treatment
While melt inclusion CO_2-H_2O concentration data (with bubble and with no CO_2 bubble restoration) provide a "vapor saturation pressure", such pressures do not necessarily convert directly into entrapment depth. Vapor saturation pressures yield a minimum entrapment depth ($\approx$ minimum pressure of crystallization; e.g. Anderson et al., 1989) unless it can be shown that the melts were vapor saturated at the time of trapping. However, in the absence of independent evidence that the melts were volatile saturated at the time of trapping, such as the presence of melt and fluid inclusions that were trapped simultaneously, there is no basis for concluding that melt inclusions were vapor saturated during entrapment, and thus pressures determined from the MI will be minimum entrapment pressures. Additionally, because rapid H diffusion through olivine can re-equilibrate melt inclusions following entrapment, CO_2-H_2O vapor saturation pressures may have been further modified to reflect the external melt H_2O content during the final storage conditions prior to rapid ascent and eruption, so the pressure determined in that case is the last equilibration pressure (e.g. Mann et al., 2013) rather than initial entrapment conditions.

While the solubilities of all common volatile components in silicate melts vary with pressure, CO_2 solubility is especially sensitive to pressure (e.g., Liu et al., 2005; Behrens et al., 2004, 2009; Shishkina et al., 2014). When melts are trapped inside growing crystals, the melt could have already degassed/exsolved some fraction of its initial CO_2 and therefore not reflect the CO_2 concentration of the original magma at its source region. In this case, the CO_2 concentration reflects that of the melt at the pressure of trapping. Alternatively, the CO_2 content could be well below the saturation value so that, even though the solubility is pressure-dependent, the melt may not have reached volatile saturation before being trapped at some lower pressure.

Following trapping, some portion of the volatile components in the melt may exsolve to form a separate phase (e.g. Roedder, 1979; Anderson and Brown, 1993; Kamenetsky & Kamenetsky, 2010; Moore et al. 2015). It is very common for olivine-hosted melt inclusions to have a single, CO_2-rich vapor bubble. The post-entrapment decrease of pressure in inclusions that leads to bubble formation has two main causes: crystallization of olivine along the inclusion-host interface, and the greater thermal expansion of melt compared to olivine, which causes the melt to contract more than the host phase (cavity) during cooling (Roedder, 1979; Anderson and Brown, 1993). Other factors contributing to bubble formation include melt density changes during post-entrapment crystallization, diffusive loss of H from inclusions, and elastic deformation of the host mineral during pressure changes. The magnitude of the two main factors (crystallization and differential shrinkage of the included melt and host) are such that it is common for a bubble to occupy about 1 to 5 volume percent of the inclusion, and it is important to note that much of the total volume expansion takes place rapidly during eruption and quenching as the included melt cools to its glass transition temperature (Riker, 2005; Moore et al., 2015). The presence of MIAs that all contain the same proportions of melt and vapor provides strong evidence that bubbles formed after trapping (Roedder, 1984). In this case, it is reasonable to conclude that the composition of the melt that was trapped is represented by the bulk composition of the inclusion (glass + bubble).

In general, determining the bulk volatile concentration of melt inclusions in which some portion of the volatile components have fractionated into a separate vapor phase requires

the same approach that would be used to account for the presence of daughter crystals or post-entrapment crystallization: experimental reheating, *in situ* microanalysis and mass balance calculations, and/or numerical modeling (Moore et al., 2015; Aster et al., 2016; Tuohy et al., 2016; Esposito et al., 2016). The approach of experimental reheating involves re-dissolving the vapor bubble back into the melt and then quenching so that the glass can be directly analyzed for CO_2 (Mironov et al., 2015; Wallace et al., 2015). For the mass balance approach (e.g., Esposito et al., 2008; 2011; Hartley et al., 2014; Moore et al., 2015), it is necessary to determine the dissolved volatile concentrations in the glass, the room temperature density of CO_2 in the bubble, and the relative proportions of the glass and the bubble. The density of CO_2 in the bubble can be determined using Raman spectroscopy (e.g., Moore et al., 2015 and described in section 2.1.1.; Wieser et al., 2020), and the volume proportion occupied by the bubble can be determined petrographically or by using X-ray tomography (e.g. Richard et al., 2018). The numerical approach involves modeling of bubble formation and CO_2 exsolution as a function of PEC (Anderson & Brown, 1993; Steele-Macinnis et al., 2011; Wallace et al., 2015; Aster et al., 2016). Moore et al. (2018) discuss some of the relative strengths and weaknesses of different techniques applied to primitive olivine-hosted melt inclusions that contain CO_2-rich bubbles. Applying multiple methods whenever possible and looking for consistency between the different results provides confidence that the initial CO_2 concentrations of melt inclusions thus determined is correct.

In some cases, the accuracy of the mass balance calculation used to determine total CO_2 could be influenced by the presence of solid phases such as carbonate crystals or native S on the wall of the bubble (e.g. Esposito et al., 2016). However, the amount of CO_2 sequestered in carbonates may not be significant in most cases. When melt inclusions are heated long enough to destabilize most or all of the carbonate, the total CO_2 mass balance does not change significantly, but it does result in diffusive H_2O loss, as verified by D/H fractionation (Pamukcu and Gaetani, unpublished data).

A number of studies have employed the Ideal Gas Law or some other equation of state to calculate the density of the vapor within bubbles and then used their observed volume to calculate the mass of CO_2 (e.g. Shaw et al., 2008, 2010). This method, however, does not account for (disequilibrium) expansion of the bubble during quenching, and

systematically overestimates the CO_2 content of bubbles compared to *in situ* Raman analysis (Moore et al., 2015).

An alternative method to reconstruct entrapped CO_2 contents is to use a calculated bubble volume, rather than the observed volume, for the equation-of-state calculation (e.g., Riker, 2005; Maclennan, 2017; Rasmussen et al., 2020). The premise of this method is that the rapid cooling rates upon eruption, expected for most samples, leads to a phase of cooling where CO_2 addition to the vapor bubble has effectively ceased (i.e., CO_2 closed) while the vapor bubble may continue to expand (Anderson and Brown, 1993). Therefore, the equation-of-state calculation must use a modeled volume of the vapor bubble at the time CO_2 addition to the vapor bubble stopped. Several calculated-volume approaches assume bubble growth occurs in two stages: one pre-eruptive stage where vapor-melt equilibrium exists and a second stage of rapid cooling upon ascent and eruption where bubble growth occurs without significant CO_2 addition (e.g., Riker, 2005; Aster et al., 2016). However, in many cases, it is likely that CO_2 addition to vapor bubbles can occur during magma ascent and quench (Rasmussen et al., 2020). Other calculated-volume approaches model the vapor bubble at the time CO_2 closes (Maclennan, 2017; Rasmussen et al., 2020). An open-source Python code named MIMiC was presented by Rasmussen et al. (2020) that corrects melt inclusions for post-entrapment processes, including vapor-bubble growth. They showed that their calculated-volume approach yields CO_2 reconstructions similar to expected values based on data from rehomogenized melt inclusions from the same samples.

Finally, some host mineral grains may contain MIAs that include melt inclusions with a range of bubble sizes (Hartley et al., 2014; Moore et al., 2015) approaching 100 volume percent of the inclusion (Roedder et al., 1963; i.e., CO_2-rich fluid inclusions with a volumetrically minor glassy rim). While this occurrence provides strong evidence that the melts were volatile-saturated at the time of trapping, these larger melt inclusion bubbles, if not associated with decrepitation of the melt inclusion, likely represent heterogeneously entrapped inclusions (e.g., Steele-MacInnis et al. 2017). In this case, the bulk composition of the inclusions would overestimate the dissolved CO_2 concentration of the melt at the time of entrapment. However, as described by Steele-MacInnis et al. (2017),

the presence of this co-trapped fluid may better preserve the CO_2 concentration of the glass since the pressure drop due to PEC will be less.

3.3. For trace elements

Similar to major elements that are compatible in the host mineral, compatible trace element abundances will be affected by PEC of melt inclusions. Models for the evolution of trace element concentrations during PEC highlight that the type of process considered for PEC (i.e., equilibrium versus fractional) has a major influence on the post-entrapment (PE) contents of melt inclusions (Figure 10 a-f; Baudouin et al., 2020).
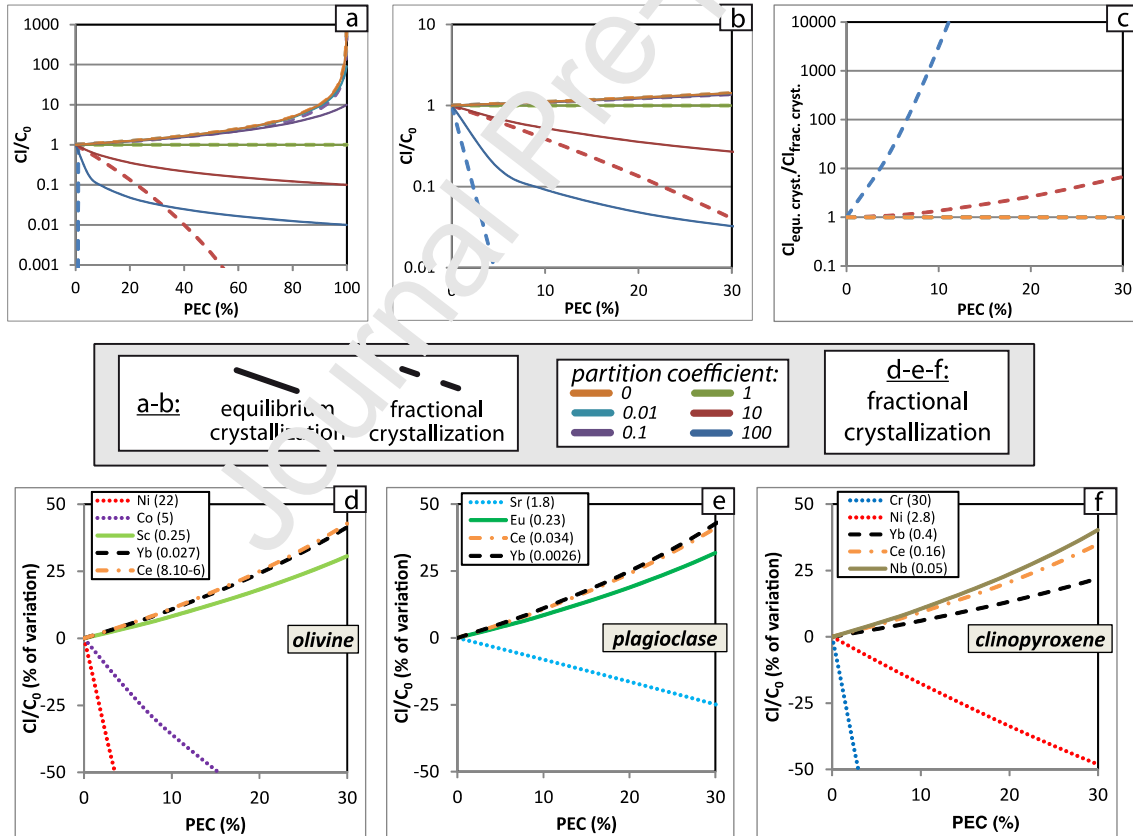

Fig. 10: Evolution of trace elements contents during PEC. a-b) present the evolution of the melt inclusion content (Cl) relative to initial content (C_0) for elements with various partition coefficients. In c-e) the variation is presented in percent of variation relative to

C_0. In a-b) both equilibration crystallization (solid lines), and fractional crystallization (dashed lines) models are presented for theoretical elements with various partition coefficients (from D= 0 to D=100). In c-e) an equilibrium crystallization model is used, and specific elements are considered for PEC of melt inclusions in olivine (c), plagioclase (d), and clinopyroxene (e). Considered partition coefficients are presented between brackets for each element, and are from Laubier et al. (2014) for all elements except Ce in olivine from Sun and Liang (2013), and Cr in clinopyroxene from Bacon and Druitt (1988). Eu partition coefficient value is for redox conditions buffered with NNO.

Compatible elements are depleted in the melt as soon as crystallization begins, this depletion being extreme when considering a fractional crystallization model (Figure 10a-b). Incompatible element contents are significantly affected only after extensive crystallization (e.g., the concentration of a perfectly incompatible element only increases by a factor of 1.4 - thus by 40% - after 30% of crystallization, Figure 10b), and only varies marginally depending on the considered crystallization model in the first ~50% of crystallization (Fig. 10a). The choice of the crystallization model to consider (equilibrium or fractional; Fig 10c) should therefore be described when quantifying post-entrapment variation of compatible elements. The compositional gradients adjacent to melt inclusions are proof that fractional crystallization occurs. These are not produced by equilibrium crystallization. During equilibrium crystallization, the melt would remain in equilibrium with the host and PEC would be impossible to identify. Therefore, for the correction of the compatible element composition (for example Ni in olivine Fig. 10d, Sr in plagioclase Fig. 10e), we advise that fractional crystallization equations should be used. Accordingly, the evolution of key compatible and incompatible elements during PE evolution of melt inclusions hosted in olivine, plagioclase, and clinopyroxene are presented in Fig. 10d-f, and highlight that PEC corrections should be applied when considering compatible element contents.

For incompatible and compatible trace elements, the reliability of the melt inclusion to represent the composition of the trapped mantle melt depends on the diffusion transport of these elements through their host crystal during magma ascent, eruption and cooling (e.g., Gaetani and Watson, 2000). The effect of PEC on both compatible and incompatible elements is a common process happening on potentially short timescales. For PEC of only a few percent, the effects on incompatible elements will be small.

60

Diffusive reequilibration with external melt will require much longer timescales and is only a factor for compatible elements (e.g. Cottrell et al., 2002). Experiments on REE diffusion in natural olivine (Cherniak et al., 2010) have shown that melt inclusions trapped in olivine (50 μm and 1 mm radii, respectively) will preserve their REE composition for a few decades to tens of thousands of years, which encompasses the duration of melt inclusion residence and transport through the crust. Faster REE diffusion are also described (Spandler et al., 2007), which are possibly due to "fast path" diffusion along dislocation cores. As a community we do not particularly see the kind of fast diffusion they advocate in natural systems, although we acknowledge that such a process might exist. Incompatible element variations are more restricted but, regardless of the extent of PEC, we recommend PEC corrections for incompatible elements (as well as for major and compatible elements).

Recommended practice:

-Report raw data (no PEC correction, not normalized to 100 wt. %; we provide a template of a table as an example; Table S1)
-Report the method used for PEC correction of major element compositions
-Report the value of Kd used (in case of olivine-hosted melt inclusions)
-Coupling of CO_2 and H_2O in order to identify at least H loss. Report the method use for initial volatile reconstruction if attempted
-We recommend PEC corrections for incompatible elements

Conclusions

The study of melt inclusions has evolved over the past 2-3 decades to become a mature and commonly used method to characterize a wide variety of igneous and volcanic processes. However, to date there has been little concerted effort to develop a set of guidelines to assist the beginning, and even experienced, researcher on the proper protocols to follow. As a community effort to constructively develop guidelines for the documentation, collection and reporting of data from melt inclusion studies, we provide recommendations to all scientists studying melt inclusions in an effort to systematize data collection and reporting to facilitate comparison and evaluation of reported melt inclusion data. We are aware that these guidelines increase the amount of information that must be reported and will lead to an increase in the amount of text and images required, and this

additional information can be provided mainly in the supplementary material of a publication. We encourage reviewers to request that images of melt inclusions be included, that raw data not be normalized to 100%, and that analytical details for each method be described in detail. We also encourage journal editors to accept the consequent size of supplementary material that will be submitted in support of the conclusions and results presented in manuscripts. Data should also be added to various online databases, such as EarthChem (http://www.earthchem.org/portal) or Georock (http://georoc.mpch-mainz.gwdg.de/georoc/) for chemistry data or Puli for IR spectra (http://www.puli.mfgi.hu/).

Declaration of interests
☒ The authors declare that they have no known competing financial interests or personal relationships that could have appeared to influence the work reported in this paper.

Fig. 1: (A) picture of two glassy olivine-hosted melt inclusions from the Ambae volcano. Inside both inclusions, we can see the very circular bubble and the squarish spinel. (B) Sometimes the melt adopts the faceted crystal shape of the host mineral giving this Sommata melt inclusion this "raisin" aspect. (C) BSE image of a crystallized inclusions from Mount Shasta, with microcrystals (m), several small bubbles (b) and matrix glass, (D) picture in transmitted light of a devitrified melt inclusion from Pan de Azucar volcano (pictures B, C and D from Le Voyer, PhD 2009).

Fig. 2: Idealized flow-chart for melt inclusion (MI) sample analyses given sample preparation and analysis-induced damage considerations. Depending on the intended research, particular steps may be skipped. Samples can be re-polished to remove upper surfaces that were damaged by various techniques (EPMA, SIMS, LA-ICPMS). See text

for references and for more details on preparation and best practices for MI sample selection, MI homogenization, each for analytical technique. Melt inclusions in inset photos are from Kīlauea Volcano's 2018 Lower East Rift Zone eruption.

Fig. 3: Raman spectra after frequency-temperature correction (a) of the aluminosilicate framework vibration range and (b) of the OH-stretching range ("water band").

Fig. 4: H_2O and CO_2 absorption bands in FTIR spectra of hydrous rhyolitic (top) and basanitic (bottom) melt inclusions. In the rhyolite spectrum, the 5200 cm^{-1} (molecular H_2O) and 4500 cm^{-1} (OH) bands can be seen, but the mid-IR fundamental OH stretching band (3550 cm^{-1}), which gives total H_2O, is oversaturated. The 2350 cm^{-1} band (molecular CO_2) can also be seen. In the basanite spectrum, total H_2O is much lower and therefore can been seen at 3550 cm^{-1}. The doublet at 1515 and 1430 cm^{-1} is for dissolved carbonate, which is the primary solution mechanism for CO_2 in mafic compositions. Data are from Roberge et al. (2013) and Rasmussen et al. (2017).

Fig. 5: Edge-step normalized XANES spectra of basaltic standard glasses (Smithsonian catalog number NMNH 117393) equilibrated from 3.5 log units below, to 4.5 log units above, the QFM buffer. Spectra of most oxidized and most reduced glasses are highlighted in red and blue, respectively (modified from Cottrell et al., 2009, with permission).

Fig. 6: Schematic illustration of Fe K-edge XANES analysis of an olivine-hosted melt inclusion, highlighting the geometrical considerations and X-ray penetration depths for a typical basalt. Solid and dashed red lines indicate the depth at which 37% and 86%, respectively, of the X-rays at 7118 eV are absorbed ($1/e$ and $1/e^2$, respectively). Figure modified from Lerner et al., submitted, and provided courtesy of Allan Lerner and Michelle Muth.

Fig. 7: Calibration curve for the centroid position (blue) and peak height ratio (red) determined by XANES compared with the $Fe^{3+}/\sum Fe$ ratios of the Smithsonian basaltic standard glasses determined by Mössbauer spectroscopy (data from Moussallam et al., 2019a).

Fig. 8: Three independent time-series analyses of a hydrated (5.2 wt.% H_2O) basalt under three different beam attenuation conditions. Plotted is normalized fluoresced intensity (FF) over the incident flux (I0), with the monochromator set to the position of the higher energy pre-edge multiplet, integrated over 1 s intervals at a spot size of 2.5×1.2 μm (modified from Moussallam et al., 2019a). At high photon flux density (blue circles), the intensity of the high energy pre-edge peak increases with time, whereas this is not the case at low flux density, once the beam has been attenuated, here down to 1% of its original flux (using a 0.25 mm Al foil).

Fig. 9: Log-Log plot of concentrations of F (**a**), S (**b**), and Cl (**c**) measured by SIMS vs. that measured by EPMA (circles). Standards are categorized according to their SiO_2 contents into mafic, intermediate, and acidic. The solid line is a one-to-one slope

indicating the coherence of the fit, and the dashed lines are 20% slope variation to help reading the figure. The square symbols are ERDA measurements (modified from Rose-Koga et al., 2020). The high SiO_2 standards do not fall on the same slope as standards with mafic and intermediate compositions (Rose-Koga et al., 2020).

Fig. 10: Evolution of trace elements contents during PEC. a-b) present the evolution of the melt inclusion content (Cl) relative to initial content (C_0) for elements with various partition coefficients. In c-e) the variation is presented in percent of variation relative to C_0. In a-b) both equilibration crystallization (solid lines), and fractional crystallization (dashed lines) models are presented for theoretical elements with various partition coefficients (from D= 0 to D=100). In c-e) an equilibrium crystallization model is used, and specific elements are considered for PEC of melt inclusions in olivine (c), plagioclase (d), and clinopyroxene (e). Considered partition coefficients are presented between brackets for each element, and are from Laubier et al. (2014) for all elements except Ce in olivine from Sun and Liang (2013), and Cr in clinopyroxene from Bacon and Druitt (1988). Eu partition coefficient value is for redox conditions buffered with NNO.

References

Agrinier P., Jendrzejewski N., 2000. Overcoming problems of density and thickness measurements in FTIR volatile determinations: a spectroscopic approach. Contributions to Mineralogy and Petrology, 139, 265-272, https://doi.org/10.1007/s004100000141

Anderson, A.T., 1974. Evidence for a Picritic, Volatile-rich Magma beneath Mt. Shasta, California, Journal of Petrology, 15, 243-267.

Anderson, A.T., Newman, S., Williams, S.N., Druitt, T.H., Skirius, C. and Stolper, E., 1989. H_2O, CO_2, Cl and gas in Plinian and ash flow Bishop rhyolite. Geology, 17, 221-225.

Anderson, A.T. and Brown, G.G., 1993. CO_2 contents and formation pressures of some Kilauean melt inclusions. American Mineralogist, 78, 794-803.

Anderson AT, Davis AM, Lu F, 2000. Evolution of Bishop Tuff rhyolitic magma based on melt and magnetite inclusions and zoned phenocrysts. Journal of Petrology, 41, 449-473.

Aster, E.M., Wallace, P.J., Moore, L.R., Watkins, J., Gazel, E., Bodnar, R.J., 2016. Reconstructing CO_2 concentrations in basaltic melt inclusions using Raman analysis of vapor bubbles. Journal of Volcanology and Geothermal Resources, 323, 148-162.

Bacon, C.R. and Druitt, T.H., 1988. Compositional Evolution of the Zoned Calcalkaline Magma Chamber of Mount-Mazama, Crater Lake, Oregon. Contributions to Mineralogy and Petrology 98: 224-256.

Barth, A., Newcombe, M., Plank, T., Gonnermann, H., Hajimirza, S., Soto, G.J., Saballos, A., and Hauri, E.H., 2019. Magma decompression rate correlates with explosivity at basaltic volcanoes — Constraints from water diffusion in olivine, Journal of Volcanology and Geothermal Research 387, p. 106664

Barth, A. and Plank, T., 2021. The ins and outs of water in olivine-hosted melt inclusions: hygrometer vs speedometer, Frontiers in Earth Science, accepted with revisions.

Bartoli, O., Cesare, B., Poli, S., Bodnar. R. J., Acosta-Vigil, A., Frezzotti, M. L. & Meli, S., 2013. Uncovering the composition of melt and fluid regime at the onset of crustal anatexis and S-type granite formation. Geology, 41, 115-118.

Baudouin, C., France, L., Boulanger, M., Dalou, C. D. Vidal, J.L., 2020. Trace element partitioning between clinopyroxene and alkaline magmas. Contributions to Mineralogy and Petrology, 175: 42. doi:10.1007/s00410-020-01680-6.

Beddoe-Stephens B, Aspden JA, Shepherd TJ, 1988. Glass inclusions and melt compositions of the Toba Tuffs, Northern Sumatra. Contributions to Mineralogy and Petrology, 83, 278-287

Befus K. S., Gardner J. E., Zinke R. W., 2012. Analyzing water contents in unexposed glass inclusions in quartz crystals. American Mineralogist, 97, 1898-1904, https://doi.org/10.2138/am.2012.4206

Behrens, H., Ohlhorst, S., Holtz, F., & Champenois, M., 2004. CO_2 solubility in dacitic melts equilibrated with H_2O-CO_2 fluids: Implications for modeling the solubility of CO_2 in silicic melts. Geochimica et Cosmochimica Acta, 68, 4687-4703.

Behrens, H., Misiti, V., Freda, C., Vetere, F., Botcharnikov, R. E., & Scarlato, P., 2009. Solubility of H_2O and CO_2 in ultrapotassic melts at 1200 and 1250 C and pressure from 50 to 500 MPa. American Mineralogist, 94, 105-120.

Berkesi, M., Hidas, K., Guzmics, T., Dubessy, J., Bodnar, R. J., Szabó, Cs., Vajna, B. & Tsunogae, T., 2009. Detection of small amounts of H_2O in CO_2-rich fluid inclusions using Raman spectroscopy. Journal of Raman Spectroscopy, 40, 1461-1463; http://10.1002/jrs.2440

Berry, A. J., O'Neill, H. S. C., Jayasuriya, K. D., Campbell, S. J. & Foran, G. J., 2003. XANES calibrations for the oxidation state of iron in a silicate glass. American Mineralogist 88, 967–977.

Berry, A. J., Stewart, G. A., O'Neill, H. S. C., Mallmann, G. & Mosselmans, J. F. W., 2018. A re-assessment of the oxidation state of iron in MORB glasses. Earth and Planetary Science Letters 483, 114–123.

Bodnar, R. J. & Student, J. J., 2006. Melt inclusions in plutonic rocks: Petrography and microthermometry. In Melt Inclusions in Plutonic Rocks (J. D. Webster, ed.) Mineral. Assoc. Canada, Short Course 36, 1-26.

Bodnar, R.J. and Frezzotti M-L., 2020. Microscale Chemistry Raman Analysis of Fluid and Melt Inclusions, Elements, DOI: 10.2138/gselements.15.2.93

Borisov, A., H. Behrens, and F. Holtz, 2018. Ferric/ferrous ratio in silicate melts: a new model for 1 atm data with special emphasis on the effects of melt composition. Contributions to Mineralogy and Petrology, 173, doi.org/10.1007/s00410-018-1524-8.

Botcharnikov, R. E., Koepke, J., Holtz, F., McCammon, C. & Wilke, M., 2005. The effect of water activity on the oxidation and structural state of Fe in a ferro-basaltic melt. Geochimica et Cosmochimica Acta 69, 5071–5085.

Bouvier, A.S., Métrich, N., and Deloule, E., 2008. Slab-Derived Fluids in the Magma Sources of St. Vincent (Lesser Antilles Arc): Volatile and Light Element Imprints: Journal of Petrology, 49, 1427–1448, doi: 10.1093/petrology/egn031.

Bouvier, A.-S., Manzini, M., Rose-Koga, E.F., Nichols, A.R.L., and Baumgartner, L.P., 2019. Tracing of Cl input into the sub-arc mantle through the combined analysis of B, O and Cl isotopes in melt inclusions : Earth and Planetary Science Letters, 507, 30–39, doi: 10.1016/j.epsl.2018.11.036.

Bracco Gartner, A.J.J., Nikogosian, I.K., Luciani, N., Davies, G.R., and Koornneef, J.M., 2019. Coupled Sr-Nd-Pb isotope and trace element ratios in olivine-hosted melt inclusions from subduction-related magmatism in central Italy. Acta Mineralogica-Petrographica Abstract Series 10, 21.

Bucholz, C.E., Gaetani, G.A., and Behn, M.D., 2013 Post-entrapment modification of volatiles and oxygen fugacity in olivine-hosted melt inclusions: Earth and Planetary Science Letters, 374, 145–155.

Burke, E. A.J., 2001. Raman microspectrometry of fluid inclusions. Lithos, 55, 139-158.

Bussweiler ,Y.,Giuliani A., Greig, A., Kjarsgaard, B.A., Petts, D. Jackson, S.E., Barrett, N., Luo, Y., Pearson, D.G. (2019) Trace element analysis of high-Mg olivine by LA-ICP-MS – Characterization of natural olivine standards for matrix-matched calibration and application to mantle peridotites, Chemical Geology, 524, 136-157.

Cabral, R.A., Jackson, M.G., Rose-Koga, E.F., Koga, K.T., Whitehouse, M.J., Antonelli, M.A., Farquhar, J., Day, J.M.D., and Hauri, E.H., 2013 Anomalous sulphur isotopes in plume lavas reveal deep mantle storage of Archaean crust: Nature, 496, 490–493, doi: 10.1038/nature12020.

Cabral, R. A., Jackson, M. G., Koga, K. T., Rose-Koga, E. F. Hauri, E. H., Whitehouse, M. J. & Kelley, K. A., 2014. Volatile cycling of H_2O CO_2 F, and C l in the HIMU mantle: A new window provided by melt inclusions from oceanic hot spot lavas at M angaia, Cook Islands. Geochemistry, Geophysics, Geosystems, 15, 4445-4467.

Cadoux, A., Iacono-Marziano, G., Paonita, A., Deloule, E., Aiuppa, A., Nelson Eby, G., Costa, M., Brusca, L., Berlo, K., Geraki K. Mather, T.A., Pyle, D.M., and Di Carlo, I., 2017. A new set of standards for in - situ measurement of bromine abundances in natural silicate glasses: Application to SR-XRF, LA-ICP-MS and SIMS techniques: Chemical Geology, 452, 60–70, doi: 10.1016/j.chemgeo.2017.01.012.

Cannatelli, C., Doherty, A.L. Esposito, R., Lima, A., and De Vivo, B., 2016. Understanding a volcano through a droplet: a melt inclusion approach. Journal of Geochemical Exploration, 171, 4-19.

Carroll, M., and Rutherford, M.J., 1988, Sulfur speciation in hydrous experimental glasses of varying oxidation state--results from measured wavelength shifts of sulfur X-rays: American Mineralogist, 73, 845–849.

Chabiron, A., Pfeifert, C., Pironon, J., and Cuney, M., 1999. Determination of water content in melt inclusions by Raman spectrometry. In : H. Ristedt, Manag- ing Editor; V. Lüders, R. Thomas, and A. Schmidt-Mumm, Guest Editors, Terra Nostra–Schriften der Alfred-Wegner-Stiftung 99/6; ECROFI XV (European Current Research On Fluid Inclusions), Abstracts and Program, June 21–24, 1999, p. 68–69. GeoForschungsZentrum Potsdam.

Chabiron, A., Pironon, J., and Massare, D., 2004, Characterization of water in synthetic rhyolitic glasses and natural melt inclusions by Raman spectroscopy: Contributions to Mineralogy and Petrology, 146, 485–492, doi: 10.1007/s00410-003-0510-x.

Chaigneau M., Massare D., Clocchiatti R., 1980 Contribution a l'etude des inclusions vitreuses et des elements volatils contenus dans la phenocristaux de quartz de roches volcaniques acides. Bulletin Volcanologique, 43, 233-240.

Chang, J., & Audétat, A., 2020. LA-ICP-MS analysis of crystallized melt inclusions in olivine, plagioclase, apatite and pyroxene: quantification strategies and effects of post-entrapment modifications. Journal of Petrology, doi.org/10.1093/petrology/egaa085

Chaussidon, M., Albarède, F., & Sheppard, S. M., 1989. Sulphur isotope variations in the mantle from ion microprobe analyses of micro-sulphide inclusions. Earth and Planetary Science Letters, 92, 144-156.

Chaussidon, M., Robert, F., Mangin, D., Hanon, P., and Rose, E.F., 1997. Analytical procedures for the measurement of boron isotope compositions by ion microprobe in meteorites and mantle rocks: Geostandards Newsletter, 21, 7–17.

Chen, Y., Provost, A., Schiano, P., and Cluzel, N., 2011. The rate of water loss from olivine-hosted melt inclusions: Contributions to Mineralogy and Petrology, 162, 625–636, doi: 10.1007/s00410-011-0616-5.

Chen, Y., Provost, A., Schiano, P., and Cluzel, N., 2013. Magma ascent rate and initial water concentration inferred from diffusive water loss from olivine-hosted melt inclusions: Contributions to Mineralogy and Petrology, 165, 525–541, doi: 10.1007/s00410-012-0821-x.

Cherniak, D.J., 2010. REE diffusion in olivine: American Mineralogist, 95, 362–368, doi: 10.2138/am.2010.3345.

Cottrell, E., Spiegelman, M., & Langmuir, C. H., 2002. Consequences of diffusive reequilibration for the interpretation of melt inclusions. Geochemistry, Geophysics, Geosystems, 3, 1-26.

Cottrell, E., Kelley, K. A., Lanzirotti, A. & Fischer, R. A., 2009. High-precision determination of iron oxidation state in silicate glasses using XANES. Chemical Geology 268, 167–179.

Cottrell, E. & Kelley, K. A., 2011. The oxidation state of Fe in MORB glasses and the oxygen fugacity of the upper mantle. Earth and Planetary Science Letters 305, 270–282.

Cottrell, E. & Kelley, K. A., 2013. Redox Heterogeneity in Mid-Ocean Ridge Basalts as a Function of Mantle Source. Science 340, 1314–1317.

Cottrell, E., Lanzirotti, A., Mysen, B., Birner, S., Kelley, K. A., Botcharnikov, R., Davis, F. A. & Newville, M., 2018. A Mössbauer-based XANES calibration for hydrous basalt glasses reveals radiation-induced oxidation of Fe. American Mineralogist 103, 489–501.

Cottrell, E., et al., 2020. Oxygen Fugacity Across Tectonic Settings, in AGU Geophysical Monograph: Redox variables and mechanisms in magmatism and volcanism. , D.R. Neuville and R. Moretti, Editors. 2020, Wiley.

Créon, L., Levresse, G., Remusat, L., Bureau, H., and Carrasco-Núñez, G., 2018. Chemical Geology, 483, 162–173, doi: 10.1016/j.chemgeo.2018.02.038.

Danyushevsky, L., Della-Pasqua, F., and Sokolov, S., 2000. Re-equilibration of melt inclusions trapped by magnesian olivine phenocrysts from subduction-related magmas: petrological implications. Contributions to Mineralogy and Petrology, 138, 68–83.

Danyushevsky, L. V., Sokolov, S. & Falloon, T. J., 2002a. Melt inclusions in olivine phenocrysts: using diffusive re-equilibration to determine the cooling history of a crystal, with implications for the origin of olivine-phyric volcanic rocks. Journal of Petrology 43, 1651–1671.

Danyushevsky, L. V., McNeill, A. W. & Sobolev, A. V., 2002b. Experimental and petrological studies of melt inclusions in phenocrysts from mantle-derived magmas: an overview of techni- ques, advantages and complications. Chemical Geology 183, 5–24.

Danyushevsky, L.V., and Plechov, P., 2011. Petrolog3: Integrated software for modeling crystallization processes: Geochemistry Geophysics Geosystems, 12, doi: 10.1016/0098-3004(90)90074-4.

Dauphas, N., Roskosz, M., Alp, E.E., Neuville, D.R., Hu, M.Y., Sio, C.K., Tissot, F.L.H., Zhao, J., Tissandier, L., Medard, E., and Cordier, C., 2014. Magma redox and

structural controls on iron isotope variations in Earth's mantle and crust: Earth and Planetary Science Letters, 398, 127–140, doi: 10.1016/j.epsl.2014.04.033.

Decraene M.-N., Marin-Carbonne J., Bouvier A.-S., Villeneuve J., Bouden N., Luais B., Deloule E., 2021. High spatial resolution and high precision measurements of iron isotopes by SIMS by using the new Hyperion RF Plasma source, Rapid Communications in Mass Spectrometry, 35, doi:10.1002/rcm.8986

Deer W.A., Howie R.A., Zussman J., 1997. Rock-forming minerals. Geological Society, London.

Delhaye, M. & Dhamelincourt, P., 1975. Raman microprobe and microscope with laser excitation. Journal of Raman Spectroscopy, 3, 33–43.

Devine, J., Gardner, J.E., Brack, H.P., Layne, G.D. and Rutherford, M.J., 1995. Comparison of microanalytical methods for estimating H_2O contents of silicic volcanic glasses, American Mineralogist, 80, 319-328.

Dhamelincourt, P., Bény, J.-M., Dubessy, J. & Poty, B., 1979. Analyse d'inclusions fluides à la microsonde MOLE à effet Raman. Bulletin de Minéralogie, 102, 600–610 [in French].

Di Genova, D. Kolzenburg, S. Wiesmaier, S., Dallanave, E., Neuville, D.R., Hess, K.-U., Dingwell, D.B., 2017. A chemical tipping point governing mobilization and eruption style of rhyolitic magma. Nature, 552, 235-238https://doi.org/10.1038/nature24488.

Di Genova, D., Caracciolo, A., Kolzenburg, S., 2018. Measuring the degree of "nanotilization" of volcanic glasses: Understanding syn-eruptive processes recorded in melt inclusions. Lithos, 318–319, 209-218.

Dixon, J. E., Stolper, E. M., & Holloway, J. R., 1995. An experimental study of water and carbon dioxide solubilities in mid-ocean ridge basaltic liquids. Part I: calibration and solubility models. Journal of Petrology, 36, 1607-1631.

Donovan, J.J., and Tingle, T.N., 1996. An improved mean atomic number background correction for quantitative microanalysis: JMSA, 2, 1–7.

Drignon, M. J., Nielsen, R. L., Tepley, F. J., III & Bodnar, R. J., 2019a. Upper mantle origin of plagioclase megacrysts from plagioclase ultraphyric MORB. Geology, 47, 43-46. https://doi.org/10.1130/G45542.1

Drignon, M. J., Nielsen, R. L., Tepley, F. J., III & Bodnar, R. J., 2019b. Re-equilibration processes occurring in plagioclase-hosted melt inclusions from plagioclase ultraphyric basalts. Geochemistry, Geophysics, Geosystems (G-cubed), 20, 109-119. https://doi.org/10.1029/2018GC007795

Dyar, M.D., McCanta, M., Breves, E.A., Caret, C.J., Lanzirotti, A., 2016. Accurate predictions of iron redox state in silicate glasses: A multivariate approach using X-ray absorption spectroscopy. American Mineralogist, 101, 744-747.

Esposito, R., Bodnar, R. J., De Vivo, B., Lima, A., Fedele, L., Shimizu, N. & Belkin, H., 2008. Volatiles in the magma associated with the Solchiaro eruption in the Phlegrean Volcanic District (Italy). Eos Trans. AGU, 89(52), Fall Meet. Suppl., Abstract V21A-2079.

Esposito, R., Bodnar, R. J., Danyushevsky, L. V., De Vivo, B., Fedele, L., Hunter, J., Lima, A. & Shimizu, N., 2011. Volatile evolution of magma associated with the Solchiaro eruption in the Phlegrean Volcanic District (Italy). Journal of Petrology, 52, 2431-2460. http://dx.doi.org/10.1093/petrology/egr051

Esposito, R., Hunter, J., Schiffbauer, J. D., Shimizu, N., & Bodnar, R. J. (2014). An assessment of the reliability of melt inclusions as recorders of the pre-eruptive volatile content of magmas. American Mineralogist, 99, 976-998.

Esposito, R., Lamadrid, H.M., Redi, D., Steele-MacInnis, M., Bodnar, R.J., Manning, C.E., De Vivo, B., Cannatelli, C., Lima, A., 2016. Detection of liquid H_2O in vapor bubbles in reheated melt inclusions: Implications for magmatic fluid composition and volatile budgets of magmas? American Mineralogist, 101, 1691-1695.

Farges, F., Lefrère, Y., Rossano, S., Berthereau, A., Calas, G. & Brown, G. E., 2004. The effect of redox state on the local structural environment of iron in silicate glasses: a combined XAFS spectroscopy, molecular dynamics, and bond valence study. Journal of Non-Crystalline Solids 344, 176–188.

Ferriss, E., Plank, T., Newcombe, M., Walker, D., Hauri, E., 2018. Rates of dehydration of olivines from San Carlos and Kilauea Iki, Geochimica et Cosmochimica Acta 242, 165-190.

Fialin, M., Wagner, C., Métrich, N., Humler, E., Galoisy, L., and Bézos, A., 2001. Fe3+/ΣFe vs. FeLα peak energy for minerals and glasses: Recent advances with the electron microprobe : American Mineralogist, 86, 456–465.

Fialin, M., Bézos, A., Wagner, C., Magnien, V., and Humler, E., 2004. Quantitative electron microprobe analysis of Fe3+/Fetot : basic concepts and experimental protocol for glasses: American Mineralogist, 89, 654–662.

Fialin, M., and Wagner, C., 2012. Redox kinetics of iron in alkali silicate glasses exposed to ionizing beams: Examples with the electron microprobe, Journal of Non-Crystalline Solids: Journal of non-crystalline solids, 358, 1617–1623, doi. 10.1016/j.jnoncrysol.2012.04.026.

Fiege, A., Ruprecht, P., Simon, A.C., Bell, A.S., Göttlicher, J., Newville, M., Lanzirotti, T., and Moore, G., 2017. Calibration of Fe XANES for high-precision determination of Fe oxidation state in glasses: Comparison of new and existing results obtained at different synchrotron radiation sources: American Mineralogist, v. 102, no. 2, p. 369–380, doi: 10.2138/am-2017-5822.

Florentin, L., Deloule, E., Faure, F., and Mangin, D., 2018. Chemical 3D-imaging of glass inclusions from allende (CV3) olivine via SIMS: A new insight on chondruleformation conditions. Geochimica et Cosmochimica Acta, 230, 83–93, doi: 10.1016/j.gca.2018.03.021.

Ford CE, Russell DG, Craven JA, Fisk MR, 1983. Olivine–liquid equilibria: temperature, pressure and composition dependence of the crystal/liquid cation partition coefficients for Mg, Fe2+, Ca and Mn. J Petrol 24:256–265.

Frezzotti, M. L., 2001. Silicate-melt inclusions in magmatic rocks: applications to petrology. Lithos, 55, 273-299.

Frezzotti, M. L., Tecce, F. & Casagli, A., 2012. Raman spectroscopy for fluid inclusion analysis. Journal of Geochemical Exploration, 112, 1-20, 10.1016/j.gexplo.2011.09.009

Gaetani, G.A., and Watson, E.B., 2000. Open system behavior of olivine-hosted melt inclusions: Earth and Planetary Science Letters, v. 183, no. 1, p. 27–41.

Gaetani, G.A., O'Leary, J.A., Shimizu, N., Bucholz, C.E., and Newville, M., 2012. Rapid reequilibration of H_2O and oxygen fugacity in olivine-hosted melt inclusions: Geology, 40, 915–918, doi: 10.1130/G32992.1.

Gaetani, G.A., O'Leary, J.A., Koga, K.T., Hauri, E.H., Rose-Koga, E.F., and Monteleone, B.D., 2014. Hydration of mantle olivine under variable water and oxygen fugacity conditions: Contributions to Mineralogy and Petrology, 167, 965–14, doi: 10.1007/s00410-014-0965-y.

Genske F., Stracke A., Berndt J., and Klemme S., 2019. Process-related isotope variability in oceanic basalts revealed by high-precision Sr isotope ratios in olivine-hosted melt inclusions. Chemical Geology, 524, 1-10. doi: 10.1016/j.chemgeo.2019.04.031.

Goncalves Feierra, P., de Ligny D., Lazzari, O., Jean, A., Cinotora Gonzalez, O., Neauville, D.R., 2013. Photoreduction of iron by a synchrotron X-ray beam in low iron content soda-lime silicate glasses: Chemical Geology, 346, 106–112.

Gualda G.A.R., Pamukcu A.S., Ghiorso M.S., Anderson A.T., Sutton S.R., Rivers M.L., 2012. Timescales of quartz crystallization and the longevity of the Bishop giant magma body. PLoS ONE, 7, e37492.

Guzmics, T., Berkesi, M., Bodnar, R.J., Fall, A., Bali, E., Milke, R., Vetlényi, E., and Szabó, C., 2019. Natrocarbonatites: A hidden product of three-phase immiscibility: Geology, 47, 527–530, doi: 10.1016/j.lithos.2006.03.018.

Head, E., Lanzirotti, A., Newville, M., & Sutton, S., 2018. Vanadium, sulfur, and iron valences in melt inclusions as a window into magmatic processes: A case study at Nyamuragira volcano, Africa. Geochimica et Cosmochimica Acta, 226, 149–173.

Halter, W.E., Pettke, T., Heinrich, C.A., and Rothen-Rutishauser, B., 2002. Major to trace element analysis of melt inclusions by laser-ablation ICP-MS: methods of quantification: Chemical Geology, 183, 63–86.

Hanyu, T., Yamamoto, J., Kimoto, K., Shimizu, K., & Ushikubo, T., 2020. Determination of total CO_2 in melt inclusions with shrinkage bubbles. Chemical Geology, 557, 119855.

Harlou, R., Pearson, D.G., Nowell, G.M., Ottley, C.J., and Davidson, J.P., 2009. Chemical Geology: Chemical Geology, 260, 254–268, doi: 10.1016/j.chemgeo.2008.12.020.

Hartley, M.E., Thordarson, T., Taylor, C., Fitton, J.G., EIMF, 2012. Evaluation of the effects of composition on instrumental mass fractionation during SIMS oxygen isotope analyses of glasses: Chemical Geology, 334, 312–323, doi: 10.1016/j.chemgeo.2012.10.027.

Hartley, M.E., Maclennan, J., Edmonds, M., and Thordarson, T., 2014. Reconstructing the deep CO_2 degassing behavior of large basaltic fissure eruptions. Earth and Planetary Science Letters, 393, 120-121.

Hartley, M. E., Shorttle, O., Maclennan, J., Moussallam Y. & Edmonds, M., 2017. Olivine-hosted melt inclusions as an archive of redox heterogeneity in magmatic systems. Earth and Planetary Science Letters 479, 192–205.

Hauri, E.H., Wang, J., Dixon, J.E., King, P.L., Mandeville, C. and Newman, S., 2002a SIMS investigations of volatiles in volcanic glasses, 1. Calibration, sensitivity and comparisons with FTIR. Chem. Geol. 183, 99–114.

Hauri, E.H., 2002b. SIMS investigations of volatiles in volcanic glasses, 2. Isotopes and abundances in Hawaiian melt inclusions. Chem. Geol. 183, 115–141.

Hauri, E. H., Shaw, A. M., Wang, J., Dixon, J. E., King, P. L., & Mandeville, C., 2006. Matrix effects in hydrogen isotope analysis of silicate glasses by SIMS. Chemical Geology, 235, 352-365.

Hauri, E.H., Weinreich, T., Saal, A.E., Rutherford, M.C., and Van Orman, J.A., 2011. High Pre-Eruptive Water Contents Preserved in Lunar Melt Inclusions: Science, 333, 213–215, doi: 10.1126/science.1204626.

Henderson, G.S., F.M.F. de Groot, and B.J.A. Moulton, 2014. X-ray Absorption Near-Edge Structure (XANES) Spectroscopy. Reviews in Mineralogy and Geochemistry, 78, 75-138.

Hervig R. L., Mazab F. K., Moore G., McMillan P. F.,2003. Analyzing hydrogen (H_2O) in silicate glass by secondary ion mass spectrometry and reflectance Fourier transform infrared spectroscopy. Developements in Volcanology, 5, 83-103, https://doi.org/10.1016/S1871-644X(03)80025-6

Hughes, E.C., Ben Buse, Kearns, S.L., Blundy, J.D., Kilgour, G., and Mader, H.M., 2019. Low analytical totals in EPMA of hydrous silicate glass due to sub-surface T charging: Obtaining accurate volatiles by difference, Chemical Geology, 505, 48–56, doi: 10.1016/j.chemgeo.2018.11.015.

Humphreys, M.C.S., Kearns, S.L., and Blundy, J.D., 2006. SIMS investigation of electron-beam damage to hydrous, rhyolitic glasses: Implications for melt inclusion analysis: American Mineralogist, 91, 667–679, doi: 10.2138/am.2006.1936.

Jackson, M.G. and S.R. Hart, 2006. Strontium isotopes in melt inclusions from Samoan basalts: Implications for heterogeneity in the Samoan plume. Earth and Planetary Science Letters. 245(1-2): p. 260-277.

Jarosewich, E., Parkes, A. S. and Wiggins, L. B., 1979. Microprobe Analysis of Four Natural Glasses and One Mineral: An Interlab- oratory Study of Precision and Accuracy, Smithsonian Contrib. Earth Sci. 22, 53-67.

Jenner, F.E., and O'Neill, H.S.C., 2012. Analysis of 60 elements in 616 ocean floor basaltic glasses: Geochemistry Geophysics Geosystems, 13, doi: 10.1029/2003GC000597.

Jugo, P.J., Wilke, M., and Botcharnikov, R.E., 2010. Sulfur K-edge XANES analysis of natural and synthetic basaltic glasses: Implications for S speciation and S content as function of oxygen fugacity. Geochimica et Cosmochimica Acta, 74, 5926-5938.

Kamenetsky, V.S., Davidson, P., Mernagh, T.P., Crawford, A.J., Gemmell, J.B., Portnyagin, M.V., and Shinjo, R., 2002. Fluid bubbles in melt inclusions and pillow-rim glasses: high-temperature precursors to hydrothermal fluids?: Chemical Geology, 183, 349-364.

Kamenetsky, V.S. and Kamenetsky, M.B., 2010. Magmatic fluids immiscible with silicate melts: examples from inclusions in phenocrysts and glasses, and implications for magma evolution and metal transport. Geofluids, 10, 293-311.

Kelley, K.A., Plank, T., Ludden, J., and Staudigel, H., 2003. Composition of altered oceanic crust at ODP Sites 801 and 1149: Geochemistry Geophysics Geosystems, 4, doi: 10.1016/0012-821X(94)00263-X.

Kelley, K.A., and Cottrell, E., 2009. Water and the Oxidation State of Subduction Zone Magmas: Science, 325, 605–607, doi: 10.1126/science.1174156.

Kelley, K.A., and Cottrell, E., 2012. The influence of magmatic differentiation on the oxidation state of Fe in a basaltic arc magma, Earth and Planetary Science Letters, 329-330, 109–121, doi: 10.1016/j.epsl.2012.02.010.

Kent, A. J., 2008. Melt inclusions in basaltic and related volcanic rocks. Reviews in Mineralogy and Geochemistry, 69, 273-331.

Kent, A. J., Ungerer, A., 2005. Production of barium and light rare earth element oxides during LA-ICP-MS microanalysis. Journal of Analytical Atomic Spectrometry, 20, 1256-1262.

King P. L., Larsen J. F., 2013. A micro-reflectance IR spectroscopy method for analyzing volatile species in basaltic, andesitic, phonolitic, and rhyolitic glasses. American Mineralogist, 98, 1162-1171, https://doi.org/10.2138/am.2013.4277

Knipping, J. L., Behrens, H., Wilke, M., Göttlicher, J. & Stabile, P., 2015. Effect of oxygen fugacity on the coordination and oxidation state of iron in alkali bearing silicate melts. Chemical Geology 411, 143-154.

Kobayashi, K., Tanaka, R., Moriguti, T., Shimizu, K. and Nakamura, E., 2004. Lithium, boron, and lead isotope systematics of glass inclusions in olivines from Hawaiian lavas: evidence for recycled components in the Hawaiian plume. Chem. Geol. 212, 143–161.

Koga, K.T., Hauri, E.H., Hirschmann, M.M., and Bell, D.R., 2003. Hydrogen concentration analyses using SIMS and FTIR: Comparison and calibration for nominally anhydrous minerals: Geochemistry Geophysics Geosystems, 4, doi: 10.1029/2002GC000378.

Koornneef, J.M., Bouman, C., Schwieters, J.B., and Davies, G.R., 2014. Measurement of small ion beams by thermal ionisation mass spectrometry using new 10^{13} Ohm resistors: Analytica Chimica Acta, 49–55, doi: 10.1016/j.aca.2014.02.007.

Koornneef, J.M., Nikogosian, I., Van Bergen, M.J., Smeets, R., Bouman, C., and Davies, G.R., 2015. TIMS analysis of Sr and Nd isotopes in melt inclusions from Italian potassium-rich lavas using prototype 10^{13} Ω amplifiers. Chemical Geology, 397, 14-23, doi: 10.1016/j.chemgeo.2015.01.005.

Koornneef, J.M., Nikogosian, I., Bergen, M.J., Vroon, P.Z., and Davies, G.R., 2019. Ancient recycled lower crust in the mantle source of recent Italian magmatism: Nature Communications, 1–10, doi: 10.1038/s41467-019-11072-5.

Kovalenko, V. I., Naumov, V. B., Girnis, A. V., Dorofeeva, V. A., & Yarmolyuk, V. V., 2006. Estimation of the average contents of H_2O, Cl, F, and S in the depleted mantle on the basis of the compositions of melt inclusions and quenched glasses of mid-ocean ridge basalts. Geochemistry International, 44, 209-231.

Kress, V.C., and Carmichael, I.S.E., 1991. The compressibility of silicate liquids containing Fe_2O_3 and the effect of composition, temperature, oxygen fugacity and pressure on their redox states: Contributions to Mineralogy and Petrology, 108, 82–92, doi: 10.1007/BF00307328.

Kress, V. C., & Ghiorso, M. S., 2004. Thermodynamic modeling of post-entrapment crystallization in igneous phases. Journal of Volcanology and Geothermal Research, 137, 247-260.

Lamadrid, H. M., Lamb, W. M., Santosh, M. & Bodnar, R. J., 2014. Raman spectroscopic characterization of H_2O in CO_2-rich fluid inclusions in granulite facies metamorphic rocks. Gondwana Research 26, 301-310, http://dx.doi.org/10.1016/j.gr.2013.07.003

Lamadrid, H. M., Moore, L., Moncada, D., Rimstidt, J. D., Burruss, R. C. & Bodnar, R. J., 2017. Reassessment of the Raman CO_2 densimeter. Chemical Geology, 450, 210-222. http://dx.doi.org/10.1016/j.chemgeo.2016.12.034

Lange R. A., 1997. A revised model for the density and thermal expansivity of K_2O-Na_2O-CaO-MgO-Al_2O_3-SiO_2 liquids from 700 to 1900 K: extension to crustal magmatic temperatures. Contributions to Mineralogy and Petrology, 130, 1-11, https://doi.org/10.1007/s004100050345

Laubier M., Grove T.L., Langmuir C.H., 2014. Trace element mineral/melt partitioning for basaltic and basaltic andesitic melts: An experimental and LA-ICP-MS study with application to the oxidation state of mantle source regions. Earth and Planetary Science Letters 392: 265-278

Layne, G.D. and Shimizu, N., 1998a. Measurement of lead isotope ratios in common silicate and sulfide phases using the Cameca IMS 1270 Ion Microprobe, in G. Gillen et al., eds., Secondary Ion Mass Spectrometry SIMS XI, John Wiley, 63-65.

Layne, G.D. and Shimizu, N., 1998b. High resolution-high transmission Secondary Ion
    Mass Spectrometry (SIMS) for the in situ microanalysis of lead isotope ratios in
    minerals and melt inclusions, Eight Annual V.M. Goldschmidt Conference,
    Mineralogical Magazine, 62A, 860-861.

Layne, G.D., 2006. Application of secondary ion mass spectrometry to the determination
    of traditional and non-traditional light stable isotopes in melt inclusions, in Melt
    Inclusions in Plutonic Rocks (J.D. Webster, ed.), Min. Assoc. Can. Short Course 36,
    27-50.

Layne, G.D., Kent, A.J.R. and Bach, W., 2009. $\delta^{37}Cl$ systematics of a back-arc spreading
    system: The Lau Basin, Geology, 37(5), 427–430; https://doi.org/10.1130/G25520A.1

Lerner, A.H., 2020. The depths and locations of magma reservoirs and their
    consequences for the behavior of sulfur and volcanic degassing. PhD
    Dissertation, University of Oregon. ProQuest Dissertations Publishing 28022240.

Lerner, A.H., Muth, M.J., Wallace, P.J., Lanzirotti, A., Newville, M., Gaetani,
    G.A., Chowdhury, P., Dasgupta, R. (submitted). Improving the reliability of Fe- and
    S-XANES measurements in silicate glasses: correcting beam damage and identifying
    Fe-oxide nanolites in hydrous and anhydrous melt inclusions. Geochimica et
    Cosmochimica Acta.

Le Voyer, M., 2009, Rôle des fluides dans la genèse des magmas d'arcs : analyses in situ
    des éléments volatils et des isotopes du bore dans les inclusions magmatiques des
    olivines primitives. PhD dissertation, Université Blaise Pascal, Clermont-Ferrand,
    France, p. 276 [in french].

Le Voyer, M., Asimow, P.D., Mosenfelder, J.L., Guan, Y., Wallace, P.J., Schiano, P.,
    Stolper, E.M., and Eiler, J.M., 2014. Zonation of H_2O and F Concentrations around
    Melt Inclusions in Olivines: Journal of Petrology, 55, 685–707.

Li, J. & Chou, I.-M., 2015. Hydrogen in silicate melt inclusions from granite detected
    with Raman spectroscopy. Journal of Raman Spectroscopy, 46, 983-986.
    https://doi.org/10.1002/jrs.4644

Liptai, N., Berkesi, M., Patkó, L., Bodnar, R.J., O'Reilly, S.Y., Griffin, W.L., Szabó, C.,
    2020. Characterization of the metasomatizing agent in the upper mantle beneath the
    northern Pannonian Basin based on Raman imaging, FIB-SEM and LA-ICP-MS

analyses of silicate melt inclusions in spinel peridotite, American Mineralogist, DOI: https://doi.org/10.2138/am-2020-7292

Liu, Y., Zhang, Y., & Behrens, H., 2005. Solubility of H_2O in rhyolitic melts at low pressures and a new empirical model for mixed H_2O–CO_2 solubility in rhyolitic melts. Journal of Volcanology and Geothermal Research, 143, 219-235.

Llovet, X., Moy, A., Pinard, P.T., Forunelle J.H., 2021. Electron probe microanalysis: A review of recent developments and applications in materials science and engineering, Progress in Materials Science, 116, 100673.

Lloyd, A.S., Plank, T., Ruprecht, P., Hauri, E.H., and Rose, W., 2013. Volatile loss from melt inclusions in pyroclasts of differing sizes, Contributions to Mineralogy and Petrology, 165, 129–153, doi: 10.1007/s00410-012-0800-2.

Lloyd, A.S., Ruprecht, P., Hauri, E.H., Rose, W., Gonnermann, H.M., and Plank, T.,, 2014. NanoSIMS results from olivine-hosted melt embayments: Magma ascent rate during explosive basaltic eruptions : Journal of Volcanology and Geothermal Research, 283, 1–18, doi: 10.1016/j.jvolgeores.2014.06.002.

Lowenstern, J.B., 1995. Applications of silicate-melt inclusions to the study of magmatic volatiles: Magmas, fluids and ore deposits, 23, 71–99.

Lowenstern, J. B., 2003. Melt inclusions come of age: volatiles, volcanoes, and Sorby's legacy. In Developments in Volcanology, 5, 1-21.

Lowenstern J. B., Pitcher B. W., 2013. Analysis of H_2O in silicate glass using attenuated total reflectance (ATR) micro-FTIR spectroscopy. American Mineralogist, 98, 1660-1668, https://doi.org/10.2138/am.2013.4466

Lytle, M.L., Kelley, K.A., Hauri, E.H., Gill, J.B., Papia, D., and Arculus, R.J., 2012. Tracing mantle sources and Samoan influence in the northwestern Lau back-arc basin: Geochemistry Geophysics Geosystems, 13, doi: 10.1038/375774a0.

Maclennan, J., 2008. Lead isotope variability in olivine-hosted melt inclusions from Iceland. Geochimica Et Cosmochimica Acta, 72, 4159-4176.

Maclennan, J., 2017. Bubble formationand decrepitation control the CO_2 content of olivine-hosted melt inclusions, Geochemistry Geophysics Geosystems,18, 597–616, doi:10.1002/2016GC006633.

Mandeville, C. W., Webster, J. D., Rutherford, M. J., Taylor, B. E., Timbal, A., & Faure, K., 2002. Determination of molar absorptivities for infrared absorption bands of H_2O in andesitic glasses. American Mineralogist, 87, 813-821.

Manley C.R., 1996. Morphology and maturation of melt inclusions in quartz phenocrysts from the Badlands rhyolite lava flow, southwestern Idaho. American Mineralogist, 81, 158-168.

Mann, C.P., Wallace, P.J., Stix, J., 2013. Phenocryst-hosted melt inclusions record stalling of magma during ascent in the conduit and upper magma reservoir prior to vulcanian explosions, Soufriere Hills volcano, Montserrat, West Indies. Bull. Volcanol. 75, 687. http://dx.doi.org/10.1007/s00445-013-0687-4.

Manzini, M., Bouvier, A.S., Barnes, J.D., Bonifacie, M., Rose-Koga, E.F., Ulmer, P., Métrich, N., Bardoux, G., Williams, J., Layne, G.D., Straub, S., Baumgartner, L.P., and John, T., 2017a. SIMS chlorine isotope analyses in melt inclusions from arc settings: Chemical Geology, 449, 112–122.

Manzini, M., Bouvier, A.-S., Baumgartner, L.P., Müntener, O., Rose-Koga, E.F., Schiano, P., Escrig, S., Meibom, A., and Shimizu, N., 2017b. Weekly to monthly time scale of melt inclusion entrapment prior to eruption recorded by phosphorus distribution in olivine from mid-ocean ridges: Geology, doi: 10.1130/G39463.1.

Manzini, M., Bouvier, A.-S., Baumgartner, L.P., Rose-Koga, E.F., Schiano, P., and Shimizu, N., 2019. Grain scale processes recorded by oxygen isotopes in olivine-hosted melt inclusions from two MORB samples, Chemical Geology, 511, 11–20, doi: 10.1016/j.chemgeo.2019.02.025.

Massare, D., Métrich, N., and Clocchiatti, R., 2002. High-temperature experiments on silicate melt inclusions in olivine at 1 atm: inference on temperatures of homogenization and H_2O concentrations, Chemical Geology, 183, 87–98.

McMillan, P., 1984. Structural studies of silicate glasses and melts—applications and limitations of Raman spectroscopy, American Mineralogist, 69, 622–644.

Mernagh, T. P. Kamentsky, V. S. & Kamenetsky, M. B., 2011. A Raman microprobe study of melt inclusions in kimberlites from Siberia, Canada, SW Greenland and South Africa. Spectrochimica Acta Part A. Molecular and Biomolecular Spectroscopy, 80(1), 82-87. https://doi.org/10.1016/j.saa.2011.01.034

Métrich, N., & Wallace, P. J., 2008. Volatile abundances in basaltic magmas and their degassing paths tracked by melt inclusions. Reviews in mineralogy and geochemistry, 69, 363-402

Mercier, M., Di Muro, A., Métrich, N., and Giordano, D., 2010. Spectroscopic analysis (FTIR, Raman) of water in mafic and intermediate glasses and glass inclusions: Geochimica et Cosmochimica Acta, 74, 5641–5656.

Milman-Barris, M.S., Beckett, J.R., Baker, M.B., Hofmann, A.E., Morgan, Z., Crowley, M.R., Vielzeuf, D., and Stolper, E., 2008. Zoning of phosphorus in igneous olivine: Contributions to Mineralogy and Petrology, 155, 739– 765, https://doi.org/10.1007/s00410-007-0268-7.

Mironov, N., Portnyagin, M., Botcharnikov, R., Gurenko, A., Hoernle, K., and Holtz, F., 2015. Quantification of the CO_2 budget and H_2O–CO_2 systematics in subduction-zone magmas through the experimental hydration of melt inclusions in olivine at high H_2O pressure: Earth and Planetary Science Letters 425, 1–11.

Moore, L., Gazel, E., Tuohy, R., Lloyd, A., Esposito, R., Steele-MacInnis, M., Hauri, E., Wallace, P., Plank, T. & Bodnar, R. J. 2015. Bubbles matter: An assessment of the contribution of vapor bubbles to melt inclusion volatile budgets. American Mineralogist, 100, 806-823. http://dx.doi.org/10.2138/am-2015-5036

Moore, L.R., Mironov, N., Portnyagin, M., Gazel, E., Bodnar, R.J., 2018. Volatile contents of primitive bubble-bearing melt inclusions from Klyuchevskoy volcano, Kamchatka: Comparison of volatile contents determined by mass-balance versus experimental homogenization. Journal of Volcanology and Geothermal Research, 358, 124-131.

Morgan, G.B., and London, D., 1996. Optimizing the electron microprobe analysis of hydrous alkali aluminosilicate glasses : American Mineralogist, 81, 1176–1185.

Morizet, Y., Brooker, R.A., Iacono-Marziano, G., and Kjarsgaard, B.A., 2013. Quantification of dissolved CO_2 in silicate glasses using micro-Raman spectroscopy: American Mineralogist, 98, 1788–1802, doi: 10.2138/am.2013.4516.

Morizet, Y., Gennaro, E., Jego, S., Zajacz, Z., Iacono-Marziano, G., Pichavant, M., Di Carlo, I., Ferraina, C., Lesne, P., 2017. A Raman calibration for the quantification of

SO_4^{2-} groups dissolved in silicate glasses: application to natural melt inclusions. American Mineralogist, 102, 2065–2076. https://doi.org/10.2138/am-2017-6100

Mourey A., France L., Laporte D. & Gurenko A., 2017. Characterization of Volatile Contents in Primitive Magmas of an Active Carbonatitic Volcanic Complex (Oldoinyo Lengai, Tanzania). Goldschmidt Abstracts, 2821.

Moussallam, Y., Oppenheimer, C., Scaillet, B., Gaillard, F., Kyle, P., Peters, N., Hartley, M., Berlo, K. & Donovan, A., 2014. Tracking the changing oxidation state of Erebus magmas, from mantle to surface, driven by magma ascent and degassing. Earth and Planetary Science Letters 393, 200–209.

Moussallam, Y., Edmonds, M., Scaillet, B., Peters, N., Gennaro, E., Sides, I. & Oppenheimer, C., 2016. The impact of degassing on the oxidation state of basaltic magmas: A case study of Kīlauea volcano. Earth and Planetary Science Letters 450, 317–325.

Moussallam Y., Longpré M-A, McCammon C., Gomez-Ulla A., Rose-Koga E.F., Scaillet B., Peters N., Gennaro E., Paris R., Oppenheimer C., 2019a. Mantle plumes are oxidized, Earth and Planetary Science Letters 527, doi.org/10.1016/j.epsl.2019.115798.

Moussallam, Y., Rose-Koga, E.F., Koga, K.T., Médard, E., Bani, P., Devidal, J.-L., and Tari, D., 2019b. Fast ascent rate during the 2017–2018 Plinian eruption of Ambae (Aoba) volcano: a petrological investigation: Contributions to Mineralogy and Petrology, 174, doi: 10.1007/s00410-019-1625-z.

Mujin, M. Nakamura, M. Miyake, A., 2017. Eruption style and crystal size distributions: Crystallization of groundmass nanolites in the 2011 Shinmoedake eruption. American Mineralogist, 102, 2367-2380.

Mutchler, S.R., Fedele, L., Bodnar, R.J., 2008. Analysis Management System (AMS) for reduction of laser ablation ICP-MS data: Mineralogical Association of Canada Short Course Series, 40.

Mysen, B. O. & Virgo, D., 1980. Solubility mechanisms of carbon dioxide in silicate melts: A Raman spectroscopic study. American Mineralogist, 65, 885-899.

Newcombe, M.E., Fabbrizio, A., Zhang, Y., Ma, C., Le Voyer, M., Guan, Y., Eiler, J.M., Saal, A.E., and Stolper, E.M., 2014. Chemical zonation in olivine-hosted melt

inclusions: Contributions to Mineralogy and Petrology, 168, 1030–26, doi: 10.1007/s00410-014-1030-6.

Nichols A. R. L., Wysoczanski R. J., 2007. Using micro-FTIR spectroscopy to measure volatile contents in small and unexposed inclusions hosted in olivine crystals. Chemical Geology, 242, 371-384, https://doi.org/10.1016/j.chemgeo.2007.04.007

Nielsen, C.H. and Sigurdsson, H., 1981. Quantitative methods for electron microprobe analysis of sodium in natural and synthetic glasses, American Mineralogist, 66, 547-552.

Nielsen, R. L., Michael, P. J., & Sours-Page, R., 1998. Chemical and physical indicators of compromised melt inclusions. Geochimica et Cosmochimica Acta, 62, 831-839.

Nikogosian, I., Ersoy, Ö., Whitehouse, M., Mason, P. R. D., de Hoog J. C. M., Wortel, R., van Bergen, M. J., 2016. Multiple subduction imprints in the mantle below Italy detected in a single lava flow. Earth and Planetary Science Letters, 449, 12-19, doi: 10.1016/j.epsl.2016.05.033.

Norman, M. D., Garcia, M. O., Kamenetsky, V. S., & Nielsen, R. L., 2002. Olivine-hosted melt inclusions in Hawaiian picrites: equilibration, melting, and plume source characteristics. Chemical Geology, 183, 143-168.

Ochs F. A., Lange R. A., 1999, The density of hydrous magmatic liquids. Science, 283, 1314-1317, https://doi.org/10.1126/science.283.5406.1314

O'Hara, M.J., 1968. Are Ocean Floor Basalts Primary Magma? Nature, 220, 683–686, doi: 10.1038/220683a0.

Óladóttir, B.A., Sigmarsson, O., Larsen, G., and Devidal, J.-L., 2011. Provenance of basaltic tephra from Vatnajökull subglacial volcanoes, Iceland, as determined by major- and trace-element analyses: The Holocene, 21, 1037-1048.

O'Neill, H.S.C., Berry, A.J., and Mallmann, G., 2018. The oxidation state of iron in Mid-Ocean Ridge Basaltic (MORB) glasses: Implications for their petrogenesis and oxygen fugacities. Earth and Planetary Science Letters, 504, 152-162.

Pamukçu A.S., Gualda G.A.R., Rivers M.L., 2013. Quantitative 3D petrography using x-ray tomography 4: Assessing glass inclusion textures with propagation phase-contrast tomography. Geosphere, 9, 1704-1713.

Pamukçu A.S., Gualda G.A.R., Begue F., Gravley D.M., 2015. Melt inclusion shapes: Timekeepers of short-lived giant magma bodies. Geology, 43, 947-950.

Pamukçu, A.S., Wright, K.A., Gualda, G.A.R., and Gravley, D., 2020, Magma residence and eruption at the Taupo Volcanic Center (Taupo Volcanic Zone, New Zealand): Insights from rhyolite-MELTS geobarometry, diffusion chronometry, and crystal textures: Contributions to Mineralogy and Petrology, v. 175, https://doi.org/10.1007/s00410-020-01684-2.

Peppard, B.T., Steele A.M., Davis A.M., Wallace, P.J., Anderson, A.T., 2001. Zoned quartz phenocrysts from the rhyolitic Bishop Tuff, American Mineralogist, 86, 1034-1052.

Portnyagin, M., Almeev, R., Matveev, S., and Holtz, F., 2008. Experimental evidence for rapid water exchange between melt inclusions in olivine and host magma: Earth and Planetary Science Letters, v. 272, p. 541–552.

Qin, Z., Lu, F., Anderson, A.T., 1992. Diffusive reequilibration of melt and fluid inclusions, American Mineralogist, 77, 565-576.

Rasmussen, D.J., Kyle, P.R., Wallace, P.J., Sims, K.W.W., Gaetani, G.A., and Phillips, E.H., 2017. Understanding Degassing and Transport of CO$_2$-rich Alkalic Magmas at Ross Island, Antarctica using Olivine-Hosted Melt Inclusions. Journal of Petrology, 58, 841–862.

Rasmussen, D.J., Plank, T.A., Wallace, P.J., Newcombe, M.E., Lowenstern, J.B., 2020. Vapor-bubble growth in olivine-hosted melt inclusions, American Mineralogist, 105, 1898-1919.

Reinhard AA, Jackson MG, Koornneef JM, Rose-Koga EF, Blusztajn J, Konter JG, Koga KT, Wallace PJ, and Harvey J, 2018. Sr and Nd isotopic compositions of individual olivine-hosted melt inclusions from Hawai'i and Samoa: Implications for the origin of isotopic heterogeneity in melt inclusions from OIB lavas. Chemical Geology, 495, 36-49.

Richard, A., Morlot, C., Créon, L., Beaudoin, N., Balistky, V.S., Pentelei, S., Dyja-Person, V., Giuliani, G., Pignatelli, I., Legros, H., Sterpenich, J., and Pironon, J., 2018. Advances in 3D imaging and volumetric reconstruction of fluid and melt inclusions by

high resolution X-ray computed tomography. Chemical Geology, 1–12, doi: 10.1016/j.chemgeo.2018.06.012.

Riker, J., 2005. The 1859 Eruption of Mauna Loa Volcano, Hawai'i: Controls on the Development of Long Lava Channels, PhD dissertation, University of Oregon, USA.

Roberge J., Wallace P.J., Kent A.J.R., 2013. Magmatic processes in the Bishop Tuff rhyolitic magma based on trace elements in melt inclusions and pumice matrix glass. Contributions to Mineralogy and Petrology, 165:237-257

Roedder, E., 1963. Studies of fluid inclusions III: extraction and quanttative analysis of inclusions in the milligram range: Economic Geology, 58, 353–374.

Roedder, E., 1979. Origin and significance of magmatic inclusions. Bulletin de Mineralogie, 102, 467-510.

Roedder, E., 1984. Fluid Inclusions. Reviews in Mineralogy, 12, Mineralogical Society of America, 644 p.

Roeder, P.L. and Emslie, R.F., 1970. Olivine-Liquid Equilibrium, Contribution to Mineralogy and Petrology, 29, 275-289

Rosasco, G.J., Roedder, E. & Simmons, J.H., 1975. Laser-excited Raman spectroscopy for nondestructive partial analysis of individual phases in fluid inclusions in minerals. Science, 190, 557–560.

Rosasco, G.J. & Roedder, E., 1979. Application of a new Raman microprobe spectrometer to nondestructive analysis of sulfate and other ions in individual phases in fluid inclusions in minerals. Geochimica et Cosmochimica Acta, 43, 1907–1915.

Rose, E.F., Shimizu, N., Layne, G.D., and Grove, T.L., 2001. Melt production beneath Mt. Shasta from boron data in primitive melt inclusions: Science, 293, 281–283.

Rose-Koga, E.F., Koga, K., Schiano, P., and Le Voyer, M., 2012. Mantle source heterogeneity for South Tyrrhenian magmas revealed by Pb isotopes and halogen contents of olivine-hosted melt inclusions. Chemical Geology, 334, 266-279.

Rose-Koga, E.F., Koga, K.T., Moreira, M., Vlastélic, I., Jackson, M.G., Whitehouse, M.J., Shimizu, N., and Habib, N., 2017. Geochemical systematics of Pb isotopes, fluorine, and sulfur in melt inclusions from Sao Miguel, Azores. Chemical Geology, 2017. 458: p. 22-37.

Rose-Koga E.F., Koga K.T., Devidal J-L., Shimizu N., Le Voyer M., Dalou C., Döbeli M., 2020. In-situ measurements of magmatic volatile elements, F, S and Cl by electron microprobe, secondary ion mass spectrometry, and elastic recoil detection analysis, American Mineralogist, doi.org/10.2138/am-2020-7221.

Rottier, B., & Audétat, A., 2019. In-situ quantification of chlorine and sulfur in glasses, minerals and melt inclusions by LA-ICP-MS. Chemical Geology, 504, 1-13.

Rowe, M. C., Kent, A. J. R. & Nielsen, R. L., 2007. Determination of sulfur speciation and oxidation state of olivine hosted melt inclusions. Chemical Geology 236, 303–322.

Ruscitto, D.M., Wallace, P.J., Johnson, E.R., Kent, A.J.R., and Bindeman, I.N., 2010. Volatile contents of mafic magmas from cinder cones in the Central Oregon High Cascades: Implications for magma formation and mantle conditions in a hot arc: Earth and Planetary Science Letters, 298, 153–161, doi:10.1016/j.epsl.2010.07.037.

Ruscitto D.M., Wallace P.J., Kent A.J.R., 2011. Revisiting the compositions and volatile contents of olivine-hosted melt inclusions from the Mount Shasta region: Implications for the formation of high-Mg andesite. Contributions to Mineralogy and Petrology, 162:109-132, DOI 10.1007/s00410-010-0587-y

Saal, A., Hart, S.R., Shimizu, N., Hauri, E.H., and Layne, G., 1998. Pb isotopic variability in melt inclusions from oceanic island basalts, Polynesia. Science, 1998. 282, 1481-1484.

Sack R.O., Walker D., Carmichael I.S.E., 1987. Experimental petrology of alkalic lavas: constraints on cotectics of multiple saturation in natural basic liquids. Contrib Mineral Petrol 96, 1–23.

Schiano, P., 2003. Primitive mantle magmas recorded as silicate melt inclusions in igneous minerals, Earth Sci. Rev. 63, 121-144.

Schiavi, F., Kobayashi, K., Nakamura, E., Tiepolo, M., Vannucci R., 2012. Trace element and Pb–B–Li isotope systematics of olivine-hosted melt inclusions: insights into source metasomatism beneath Stromboli (southern Italy), Contributions to Mineralogy and Petrology, 163, 1011-1031.

Schiavi, F., Provost, A., Schiano, P., and Cluzel, N., 2016. P V T X evolution of olivine-hosted melt inclusions during high-temperature homogenization treatment: Geochimica et Cosmochimica Acta, 172, 1–21, doi: 10.1016/j.gca.2015.09.025.

Schiavi F., Bolfan, N., Buso, R., Laumonier, M., Laporte, D., Medjoubi, K., Venugopal, S. Gomez-Ulla, A., Cluzel, N., Hardiagon, M., 2020. Quantifying magmatic volatiles by Raman microtomography of glass inclusion-hosted bubbles, Geochemical Perspectives Letters, 16, 17-24, doi: 10.7185/geochemlet.2038

Severs, M. J., Azbej, T., Thomas, J. B., Mandeville, C. W., Jr. & Bodnar, R. J., 2007. Experimental determination of H_2O loss from melt inclusions during laboratory heating. Chemical Geology, 237(3-4), 358-371, http://dx.doi.org/10.1016/j.chemgeo.2006.07.008

Shatsky, V., Zedgenizov, D., Ragozin, A. & Kalinina, V., 2019. Silicate melt inclusions in diamonds of eclogite paragenesis from placers of the northeastern Siberian craton. Minerals, 9, 412. http://dx.doi.org/10.3390/min9070412

Shaw, A.M., Hauri, E.H., Fischer, T.P., Hilton, D.R., and Kelly, K.A., 2008. Hydrogen isotopes in Mariana arc melt inclusions. Implications for subduction dehydration and the deep-Earth water cycle. Earth and Planetary Science Letters, 275, 138–145.

Shaw, A.M., Behn, M.D., Humphris, S.E., Sohn, R.A., and Gregg, P.M., 2010. Deep pooling of low degree melts and volatile fluxes at the 85°E segment of the Gakkel Ridge: Evidence from olivine-hosted melt inclusions and glasses: Earth and Planetary Science Letters, 289, 311–322, doi: 10.1016/j.epsl.2009.11.018.

Shea, T., Costa, F., Krimer, D., and Hammer, J.E., 2015. Accuracy of timescales retrieved from diffusion modeling in olivine: A 3D perspective: American Mineralogist, 100, 2026–2042, doi: 10.2138/am-2015-5163.

Shea, T., Hammer, J.E., Hellebrand, E., Mourey, A.J., Costa, F., First, E.C., Lynn, K.J., and Melnik, O., 2019. Phosphorus and aluminum zoning in olivine: contrasting behavior of two nominally incompatible trace elements: Contributions to Mineralogy and Petrology, 1–24, doi: 10.1007/s00410-019-1618-y.

Shorttle, O., Moussallam, Y., Hartley, M. E., Maclennan, J., Edmonds, M. & Murton, B. J., 2015. Fe-XANES analyses of Reykjanes Ridge basalts: Implications for oceanic

crust's role in the solid Earth oxygen cycle. Earth and Planetary Science Letters 427, 272–285.

Sinton, C.W., Christie, D.M., and Coombs, V.L., 1993, Near-primary melt inclusions in anorthite phenocrysts from the Galapagos Platform: Earth and Planetary Science Letters, 119, 527–537.

Sisson, T. W., & Layne, G. D., 1993. H_2O in basalt and basaltic andesite glass inclusions from four subduction-related volcanoes. Earth and Planetary Science Letters, 117, 619-635.

Shishkina, T. A., Botcharnikov, R. E., Holtz, F., Almeev, R. R., Jazwa, A. M., & Jakubiak, A. A., 2014. Compositional and pressure effects on the solubility of H_2O and CO_2 in mafic melts. Chemical Geology, 388, 112-129.

Shorttle, O., Moussallam, Y., Hartley, M. E., Maclennan, J., Edmonds, M., & Murton, B. J., 2015. Fe-XANES analyses of Reykjanes Ridge basalts: Implications for oceanic crust's role in the solid Earth oxygen cycle. Earth and Planetary Science Letters, 427, 272-285.

Sobolev, V. S., & Kostyuk, V. P., 1975. Magmatic crystallization based on a study of melt inclusions. Fluid Inclusion Research, 9, 182-253.

Sobolev, A.V., Dmitriev, L.V., Barsukov, V.L., Nevsorov, V.N., Slutsky, A.B., 1980. The formation conditions of the high-magnesian olivines from the monomineralic fraction of Luna 24 regolith. Proc. 11th Lunar Sci. Conf., 105–116.

Sobolev, A.V., and Danyushevsky, L.V., 1994. Petrology and Geochemistry of Boninites from the North Termination of the Tonga Trench: Constraints on the Generation Conditions of Primary High-Ca Boninite Magmas: Journal of Petrology, 35, 1183–1211.

Sobolev, A. V., & Shimizu, N., 1993. Ultra-depleted primary melt included in an olivine from the Mid-Atlantic Ridge. Nature, 363, 151-154.

Sobolev, A. V., & Nikogosian, I. K., 1994. Petrology of long-lived mantle plume magmatism: Hawaii, Pacific and Reunion Island, Indian Ocean. Petrology, 2, 111-144.

Sobolev, A.V., and Chaussidon, M., 1996. H_2O concentrations in primary melts from supra-subduction zones and mid-ocean ridges: Implications for H_2O storage and recycling in the mantle: Earth and Planetary Science Letters, 137, 45–55.

Sobolev, A. V., 1996. Melt inclusions in minerals as a source of principle petrological information. Petrology, 4, 209-220.

Sobolev, A.V., Hofmann, A.W., Jochum, K.P., Kuzmin, D.V., and Stoll, B., 2011. A young source for the Hawaiian plume. Nature. 476, 434-437.

Sorby, H.C., 1858. On the Microscopical, Structure of Crystals, indicating the Origin of Minerals and Rocks: Quarterly Journal of the Geological Society, 14, 453–500, doi: 10.1144/GSL.JGS.1858.014.01-02.44.

Spandler C., O'Neill HStC., Kamenetsky V.S., 2007. Survival times of anomalous melt inclusions: constraints from element diffusion in olivine and chromite. Nature 447:303–306.

Steele-MacInnis, M., Esposito, R., and Bodnar, R.J., 2011. Thermodynamic model for the effect of post-entrapment crystallization on the H_2O-CO_2 systematics of vapor-saturated, silicate melt inclusions. Journal of Petrology, 52, 2461-2482.

Steele-Macinnis, M., Esposito, R., Moore, L.R., Hartley, M.E., 2017. "Heterogeneously entrapped, vapor-rich melt inclusions record pre-eruptive magmatic volatile contents," Contributions to Mineralogy and Petrology, 172:18, 1-13.

Stolper E., 1982. Water in silicate glasses: An infrared spectroscopic study. Contributions to Mineralogy and Petrology, 81, 1-17, https://doi.org/10.1007/BF00371154

Stracke, A., Genske, F., Berndt, J., and Koornneef, J.M., 2019. Ubiquitous ultra-depleted domains in Earth's mantle. Nature Geoscience, 12, 851–855, doi: 10.1038/s41561-019-0446-z.

Straub, S.M. and Layne, G.D., 2002. The systematics of boron isotopes in Izu arc front volcanic rocks, Earth Planet. Sci. Letters, 198, 25-39; https://doi.org/10.1016/S0012-821X(02)00517-4

Student, J.J., and Bodnar, R.J.,1999. Synthetic Fluid Inclusions XIV: Coexisting Silicate Melt and Aqueous Fluid Inclusions in the Haplogranite-H_2O-NaCl-KCl: Journal of Petrology, 40, 1509–1525.

Student, J. J. & Bodnar, R. J., 2004. Silicate melt inclusions in porphyry copper deposits: Identification and homogenization behavior. Canadian Mineralogist, 42,1583-1599.

Sun C. and Liang Y., 2013. The importance of crystal chemistry on REE partitioning between mantle minerals (garnet, clinopyroxene, orthopyroxene, and olivine) and basaltic melts. Chemical Geology 358: 23-36

Sutton, S. R., Lanzirotti, A., Newville, M., Dyar, M. D., & Delaney, J., 2020. Oxybarometry and valence quantification based on microscale X-ray absorption fine structure (XAFS) spectroscopy of multivalent elements. Chemical Geology, 531, 119305.

Tait, S., 1992. Selective preservation of melt inclusions in igneous phenocrysts: American Mineralogist, 77, 146–155.

Tamic N., Behrens H., Holtz F., 2001. The solubility of H_2O and CO_2 in rhyolitic melts in equilibrium with a mixed CO_2-H_2O fluid phase. Chemical Geology, 174, 333-347, https://doi.org/10.1016/S0009-2541(00)00324-7

Thomas, R., 2000. Determination of water contents of granite melt inclusions by confocal laser Raman microprobe spectroscopy : American Mineralogist, 85, 868–872.

Thomas, J. B., Bodnar, R. J., Shimizu, N. & Sinha, A. K., 2002. Determination of zircon/melt trace element partition coefficients from SIMS analysis of melt inclusions in zircon. Geochimica et Cosmochimica Acta, 66, 2887-2902.

Thomas, J. B., Bodnar, R. J., Shimizu, N. & Chesner, C., 2003. Melt Inclusions in Zircon. in ZIRCON, J.M. Hanchar & P. W.O. Hoskins, eds., Mineralogical Society of America, Reviews in Mineralogy & Geochemistry, 53, 63-87.

Thomas, R., Kamenetsky, V.S., and Davidson, P., 2006. Laser Raman spectroscopic measurements of water in unexposed glass inclusions. American Mineralogist, 91, 467-470.

Thomas, R. & Davidson, P., 2012. The application of Raman spectroscopy in the study of fluid and melt inclusions. Zeitschrift der Deutschen Gesellschaft für Geowissenschaften (ZDGG), 162, 113-126 doi: 10.1127/1860-1804/2012/0163-0113.

Tison, A. (2006) Étude expérimentale des inclusions magmatiques, Université Blaise Pascal, Clermont- Ferrand, 50p [in French].

Toplis, M.J., 2005. The thermodynamics of iron and magnesium partitioning between olivine and liquid: criteria for assessing and predicting equilibrium in natural and experimental systems, Contributions to Mineralogy and Petrology, 149, 22–39.

Tollan, P., Ellis, P., Troch, J., Neukampf J., 2019. Assessing magmatic volatile equilibria through FTIR spectroscopy of unexposed melt inclusions and their host quartz: a new technique and application to the Mesa Falls Tuff, Yellowstone: Contributions to Mineralogy and Petrology, 174, doi: 10.1007/s00410-019-1561-y.

Toplis, M. J., 2005. The thermodynamics of iron and magnesium partitioning between olivine and liquid: criteria for assessing and predicting equilibrium in natural and experimental systems. Contributions to Mineralogy and Petrology, 149, 22-39.

Tuohy, R.M., Wallace, P.J., Loewen, M.W., Swanson, D.A., and Kent, A.J.R., 2016. Geochimica et Cosmochimica Acta, 185, 1–55, doi: 10.1016/j.gca.2016.04.020.

Vigouroux N., Wallace P., Kent A.J.R., 2008. Volatiles in high-K magmas from the western Trans-Mexican Volcanic Belt: Evidence for fluid-flux melting and extreme enrichment of the mantle wedge by subduction processes. Journal of Petrology, 49:1589-1618

Von Aulock F. W., Kennedy B. M., Schipper C. I., Castro J. M., Martin D. E., Oze C., Watkins J. M., Wallace P. J., Puskar L., Nichols A. R. L., Tuffen H., 2014. Advances in Fourier transform infrared spectroscopy of natural glasses: From sample preparation to data analysis. Lithos, 206-207, 52-64, http://dx.doi.org/10.1016/j.lithos.2014.07.017

Walker, D., Shibata, T. and DeLong, S.E., 1979. Abyssal tholeiites from the Oceanographer Fracture Zone, II. Phase equilibria and mixing. Contributions to Mineralogy and Petrology, 70, 111-125.

Wallace, P.J., and Carmichael, I.S.E., 1994. Sulfur speciation in submarine basal- tic glasses as determined by measurements of SKa X-ray wavelength shifts. American Mineralogist, 79, 161–167.

Wallace P. J., Anderson A. T., Davis A. M., 1999. Gradients in H_2O, CO_2, and exsolved gas in a large-volume silicic magma system: Interpreting the record preserved in melt inclusions from the Bishop Tuff. Journal of Geophysical Research, 104 (B9), 20097–20122.

Wallace, P.J., Kamenetsky, V.S., Cervantes, P., 2015. Melt inclusion CO_2 contents, pressures of olivine crystallization, and the problem of shrinkage bubbles, American Mineralogist, 100, 787–794.

Watson, E.B., 1976. Two-Liquid Partition Coefficients: Experimental Data and Geochemical Implications, Contributions to Mineralogy and Petrology, 56, 119–134.

Webster, J. D., & Thomas, R., 2006. Silicate melt inclusions in felsic plutons: a synthesis and review. MAC Short Course, 36, 165-188.

Welsch, B., Hammer, J., and Hellebrand, E., 2014. Phosphorus zoning reveals dendritic architecture of olivine: Geology, 42, 867–870, doi: 10.1130/G35691.1.

Wieser, P.E., Lamadrid, H., Maclennan, J., Edmonds, M., Matthews, S., Iacovino, K., Jenner, F.E., Gansecki, C., Trusdell, F., Lee, R.L., Ilyinskaya, E., 2020. Reconstructing Magma Storage Depths for the 2018 Kīlauean Eruption from Melt inclusion CO_2 Contents: The Importance of Vapor Bubbles. Geochemistry, Geophysics, Geosystems, https://doi.org/10.1029/2020GC009364

Wilke, M., Farges, F., Petit, P.-E., Brown, G. E. & Martin, F., 2001. Oxidation state and coordination of Fe in minerals: An Fe K-XANES spectroscopic study. American Mineralogist 86, 714–730.

Wilke, M., Partzsch, G. M., Bernhardt, R. & Lattard, D., 2004. Determination of the iron oxidation state in basaltic glasses using XANES at the K-edge. Chemical Geology 213, 71–87.

Wilke, M., Partzsch, G.M., Bernhardt, R., and Lattard, D., 2005. Determination of the iron oxidation state in basaltic glasses using XANES at the K-edge. Chemical Geology, 220, 143-161

Wilke, M., Schmidt, C., Farges, F., Malavergne, V., Gautron, L., Simionovici, A., Hahn, M. & Petit, P.-E., 2006. Structural environment of iron in hydrous aluminosilicate glass and melt-evidence from X-ray absorption spectroscopy. Chemical Geology 229, 144–161.

Witham, F., Blundy, J., Kohn, S. C., Lesne, P., Dixon, J., Churakov, S. V., & Botcharnikov, R., 2012. SolEx: A model for mixed COHSCl-volatile solubilities and exsolved gas compositions in basalt. Computers & Geosciences, 45, 87-97.

Wysoczanski R. J. & Tani K., 2006. Spectroscopic FTIR imaging of water species in silicic volcanic glasses and melt inclusions: An example from the Izu-Bonin arc. Journal of Volcanology and Geothermal Research, 156, 302-314, https://doi.org/10.1016/j.jvolgeores.2006.03.024

Yang, K. & Bodnar, R. J., 1994. Magmatic-hydrothermal evolution in the "bottoms" of porphyry copper systems: Evidence from silicate melt and aqueous inclusions in granitoid intrusions in the Gyeongsang Basin, South Korea. International Geology Review, 36, 608-628.

Yasuda A., 2014. A new technique using FT-IR micro-reflectance spectroscopy for measurement of water concentrations in melt inclusions. Earth, Planets and Space, 66, 34, http://www.earth-planets-space.com/content/66/1/34

Yurimoto, H., Kogiso, T., Abe, K., Barsczus, H.G., Utsunomiya, A., and Maruyama, S.,, 2004. Lead isotopic compositions in olivine-hosted melt inclusions from HIMU basalts and possible link to sulfide components. Physics of the Earth and Planetary Interiors, 2004. 146, 231-242.

Zajacz, Z., Halter, W., Malfait, W.J., Bachmann, O., Bodnar, R.J., Hirschmann, M.M., Mandeville, C.W., Morizet, Y., Müntener, O., Ulmer, P., and Webster, J.D., 2005. A composition-independent quantitative determination of the water content in silicate glasses and silicate melt inclusions by confocal Raman spectroscopy: Contributions to Mineralogy and Petrology, 150, 631-642, doi: 10.1007/s00410-005-0040-9.

Zajacz, Z., Halter, W. E., Pettke, T., & Guillong, M., 2008. Determination of fluid/melt partition coefficients by LA-ICPMS analysis of co-existing fluid and silicate melt inclusions: Controls on element partitioning. Geochimica et Cosmochimica Acta, 72, 2169-2197.

Zajacz, Z., & Halter, W., 2009. Copper transport by high temperature, sulfur-rich magmatic vapor: Evidence from silicate melt and vapor inclusions in a basaltic andesite from the Villarrica volcano (Chile). Earth and Planetary Science Letters, 282, 115-121.

Zhang, H. L., Hirschmann, M. M., Cottrell, E., Newville, M. & Lanzirotti, A., 2016. Structural environment of iron and accurate determination of Fe3+/ΣFe ratios in andesitic glasses by XANES and Mössbauer spectroscopy. Chemical Geology 428, 48–58.

Zhang, H. L., Cottrell, E., Solheid, P. A., Kelley, K. A. & Hirschmann, M. M., 2018. Determination of Fe3+/ΣFe of XANES basaltic glass standards by Mössbauer

spectroscopy and its application to the oxidation state of iron in MORB. Chemical Geology 479, 166–175.

Zhang, L., Ren, Z-Y., Xia, X-P., Yang, Q., Hong, L-B., Wu, D., 2018. In situ determination of trace elements in melt inclusions using laser ablation inductively coupled plasma sector field mass spectrometry, Rapid Communications in Mass Spectrometry, https://doi.org/10.1002/rcm.8359

Zhang, Y., 1998. Mechanical and phase equilibria in inclusion–host systems: Earth and Planetary Science Letters, 157, 209–222.